Amorphous ices: experiments and numerical simulations

2006 J. Phys.: Condens. Matter 18 R919

(http://iopscience.iop.org/0953-8984/18/50/R01)

INSTITUTE OF PHYSICS PUBLISHING JOURNAL OF PHYSICS: CONDENSED MATTER

J. Phys.: Condens. Matter **18** (2006) R919–R977 doi:10.1088/0953-8984/18/50/R01

TOPICAL REVIEW

Amorphous ices: experiments and numerical simulations

Thomas Loerting[1] **and Nicolas Giovambattista**[2]

[1] Institute of Physical Chemistry/Institute of General, Inorganic and Theoretical Chemistry, University of Innsbruck, Innrain 52a, A-6020 Innsbruck, Austria
[2] Department of Chemical Engineering, Princeton University, Princeton, NJ 08544, USA

E-mail: thomas.loerting@uibk.ac.at and ngiovamb@princeton.edu

Received 22 July 2006, in final form 27 October 2006
Published 27 November 2006
Online at stacks.iop.org/JPhysCM/18/R919

Abstract

Polyamorphism, i.e. the presence of more than one amorphous state, was observed for the first time in amorphous ice or glassy water. In addition to LDA (low-density amorphous ice), a second amorphous state, HDA (high-density amorphous ice), was discovered ∼20 years ago. Since then, polyamorphism has been observed in many other substances, such as SiO_2, GeO_2, Si, and Ge. Five years ago, experimental results suggesting the existence of a third amorphous state, VHDA (very high-density amorphous ice), were reported, opening the possibility that more than two amorphous states could also be observed in other substances. A consistent phase diagram of glassy water does not yet exist. Such a phase diagram is necessary if one also wants to understand the anomalous behaviour of supercooled *liquid* water. Since the discovery of HDA, a large amount of work based on experiments and computer simulations has appeared. It is the purpose of this work to review such studies with special emphasis in comparing the experimental and simulation results. In particular, we review the recent studies concerning VHDA and its nature, and discuss the main open questions relating to the phase diagram of glassy water.

(Some figures in this article are in colour only in the electronic version)

Contents

1. Introduction

The simple structure of the water molecule, H_2O, contrasts with the complex properties and phase diagram of stable/metastable, liquid/solid water. For example, ice exists in at least 15 different phases [1], which includes metastable phases such as cubic ice, ice IV [2] and ice XII [3]. In the equilibrium and supercooled (metastable) liquid state, water is an anomalous liquid: it expands upon cooling at $T < 4\,^{\circ}$C ($P = 1$ bar), and its isothermal compressibility and constant-pressure specific heat seem to diverge at the extrapolated temperature of $\sim -45\,^{\circ}$C ($P = 1$ bar) [4, 5]. In the (metastable) amorphous solid state (also called glassy water), water shows polyamorphism, i.e. the presence of more than one amorphous state. The anomalous behaviour of supercooled and glassy water have attracted the attention of many scientists and there are excellent reviews on this topic [5–11].

This review focuses on glassy water. Understanding the behaviour of glassy water is relevant not only from a scientific point of view, but also for its presence in other fields such as biology, or in technological applications. From a scientific point of view, understanding the polyamorphism in glassy water can also be of fundamental importance for a number of other substances [12, 13]. Polyamorphism was observed for the first time in amorphous ice. Since then, many one-component types of systems showing multiple amorphous solids have been discovered. Among them are elemental liquids [14–19] (such as Si, Ge, P, S, or C), organic liquids [20–29] (such as triphenyl phosphite), tetrahedrally coordinated open networks [30–38] (such as SiO_2, GeO_2 or $GeSe_2$), and binary liquids [39–48] (such as Y_2O_3–Al_2O_3) (excellent reviews are also available on this topic [13, 49]). From a technological point of view, e.g.,

understanding the properties of glassy water may help to improve cryofixation techniques in microscopy [50] and cryopreservation techniques, which involve preserving organs and tissues for transplantation or other uses. A major problem hindering wider use of cryopreservation is the formation of ice crystals, which damage cell structures [51]. In some biological systems, such as certain trees and insects [52], the formation of glassy water seems to be involved in the preservation of life at low temperature, and some polar fish species have even developed the ability to produce antifreeze proteins [53].

In general, computer simulations are able to reproduce many of the transformations between ice, amorphous ice, and liquid water observed in experiments. This is surprising based on the different timescales accessible in experiments and simulations: experiments are limited by the largest accessible compression and cooling rates, ranging up to $\sim$6000 MPa min^{-1} [54] and $\sim 10^6$ K s^{-1} [55], while computer simulations are limited by the slowest accessible rates of $\sim 10^{11}$ MPa min^{-1} and $\sim 10^{11}$ K s^{-1} [56]. This difference in timescales implies, on one hand, that some phenomena observed in experiments cannot be reproduced in simulations (for example, liquid water crystallizes in experiments performed at normal pressure even at high cooling rates of 10^4–10^5 K s^{-1} [50], while crystallization is extremely difficult to observe in simulations, even at the slowest accessible cooling rates) [57, 58]. On the other hand, difficult processes inaccessible to experiments can be simulated (for example, it is very difficult to obtain glassy water by isobarically cooling liquid water at high pressure; so far, it has only been achieved experimentally in emulsions of water in oil, that serve the purpose of delaying nucleation [59]).

The agreement among many results obtained from computer simulations and experiments, and the possibility of simulating processes difficult to perform in experiments, has resulted in a synergism between experimental and computer simulation groups. A prime example of such a synergism is the fascinating liquid–liquid phase transition hypothesis suggested by Poole *et al* [60] based on computer simulation of water, after the experimental observation of water polyamorphism by Mishima *et al* [61]. This hypothesis might explain the anomalous behaviour of supercooled and glassy water. The number of works published in recent years, particularly on amorphous ice, makes it difficult to keep track of the different ideas and results in this field, and in particular what conclusions are based on computer simulations and which ones are based on experiments. It is the focus of this review to discuss the properties and the phase diagram of amorphous ice and its implications for the liquid state. In doing so, we compare the results obtained from the experimental approach with the results obtained from the simulation approach as closely as possible.

At least five methods have been used to make amorphous ice: condensing the vapour at low temperature [62–64] (the resulting glass being called amorphous solid water, ASW), fast-quenching of the liquid [55, 65] (the resulting glass being called hyperquenched glassy water, HGW or HQW), pressurizing ice at high pressure below the glass transition temperature [66], also in the course of cryosectioning specimens [67], heating/compressing other amorphous phases [54, 61, 68], and irradiating crystals with UV photons, electrons, protons, or fast ions [69–75]. Interestingly, these methods do not produce the same metastable amorphous structure but instead two or possibly three different phases, which can be distinguished in terms of their density. They are called low-density (LDA), high-density (HDA), and very high-density amorphous ice (VHDA), with densities of 0.94 ± 0.02 g cm^{-3}, 1.17 ± 0.02 g cm^{-3}, and 1.25 ± 0.01 g cm^{-3} at $T = 77$ K and $P = 1$ bar, respectively. HGW and ASW are very similar in terms of density and structure to LDA, so we employ the notion of 'LDA' here to refer to LDA, HGW, or ASW. HGW is produced on freezing liquid droplets at rates of $\sim 10^6$ K s^{-1}, which was done first in 1980 with the aid of a liquid cryomedium [65] and in 1985 without such a medium [55]. ASW is produced on depositing water vapour at cold substrates at low

total pressures, which is a common process in space. It was first prepared in the laboratory in 1935 [62].

In this work we focus on LDA, HDA, and VHDA. In section 2 we describe how LDA and HDA have been produced and characterized and how these two amorphous states transform by applying pressure or increasing the temperature, and we introduce the second critical point hypothesis. In section 3 we elaborate on the discovery of VHDA and address the still open question of whether it is a thermodynamically distinct state or an annealed HDA. In section 4 we compare the structural data obtained mainly from x-ray and neutron diffraction with the structural data from simulations, and in section 5 we discuss the relation between the liquid and glassy states, which includes the question of whether the amorphous states are really 1:1 proxies of the supercooled liquids.

2. Low- and high-density amorphous ice (LDA and HDA)

2.1. HDA obtained upon compression of ice I at low temperature

HDA was prepared for the first time in 1984 by Mishima *et al* [66]. Instead of attempting to cool liquid water below its glass transition temperature, they succeeded in preparing HDA by pressurizing hexagonal ice (ice I_h) at liquid nitrogen temperature (i.e., $T = 77$ K). The resulting process is called pressure-induced amorphization (PIA).

Figure 1(a) shows the evolution of the piston displacement, d, as a function of the nominal pressure, P, during the compression of four samples of 1.2 g of ice at $T = 77$ K. The subsequent evolution of d with P, upon decompression of the four samples, is also included in the figure. In this experiment, the samples have to be encased in indium, which serves as a lubricant even at $T = 77$ K and prevents sudden pressure drops and shock-wave heating [76]. At $P \sim 1.0$ GPa (10 000 bar) a sudden and sharp 'dip' of the piston into the sample is observed, which corresponds to a sudden and sharp densification (i.e., HDA is formed). As also apparent from figure 1(a), this densification is not reversible at $T = 77$ K, i.e., there is no sudden change of the piston displacement upon decompression. This implies that HDA can be *recovered* at atmospheric pressure and investigated by independent methods such as x-ray diffraction.

The x-ray diffraction pattern of recovered HDA is also reported in [66]. Figure 2 (top trace) shows the principal x-ray halo of the samples recovered after the procedure shown in figure 1(a). The broad peak centred at ∼3.0 Å indicates that, indeed, a non-crystalline, amorphous substance has formed from the crystalline material. As mentioned above, this amorph is called HDA because of its density, which exceeds the density of liquid water.

The experiments of Mishima *et al* are the first example of PIA of a crystal. Interestingly, for the case of water, a linear extrapolation of the measured solid–liquid phase boundary between ice I_h and liquid water to $P = 1.0$ GPa results roughly in a melting temperature of $T \sim 77$ K. Therefore, the process of PIA of ice I_h was initially interpreted as a melting of the solid to a metastable, vitrified liquid. It has been proposed that the melting of the ice to a vitrified liquid holds only for compression temperatures $T > 165$ K, while at $T < 140$ K the amorphization of ice I_h is due to a mechanical instability in the ice lattice [77–79]. If the last case is true and HDA is a collapsed lattice, then some microcrystalline structure should exist in HDA. Recent experiments find no signs of microcrystallinity, suggesting that HDA is the result of 'melting' ice I [80]. Instead of ice I_h, cubic ice (ice I_c) can also be employed as a starting material to produce HDA by PIA [81]. Originally, it was thought that both types of ice I lead to the same HDA. However, recent work has shown that there are subtle differences, e.g. in the x-ray structure factor and the calorigram [82].

Measuring densities *in situ* from compression experiments is not simple. For the case shown in figure 1(a), the density of the initial state, ρ (ice I_h), at $P = 1$ bar and $T = 77$ K, is

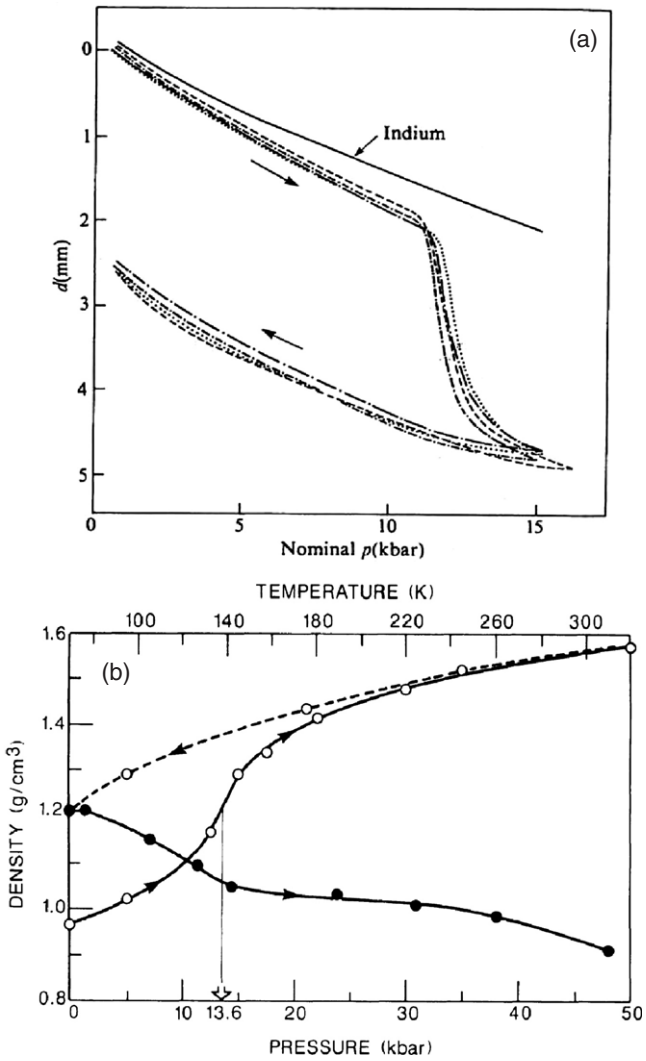

Figure 1. (a) Evolution of the piston displacement, d, as a function of the nominal pressure, P, during the ice $I_h \rightarrow$ HDA transformation. Results correspond to four samples of ice I compressed in an indium cup at $T = 77$ K. The subsequent evolution of d upon decompression of the four samples is also shown. The pressure of the sample is ∼0.9 of the nominal pressure. The compression of a volume of indium equal to the volume of the ice sample (solid line) is needed to determine the density of the sample (see the text) (from [66]). (b) Density, ρ, versus pressure upon compression of ice I_h (open circles, solid line) from MD simulations. The density during the decompression of the resulting amorphous structure, HDA, is also shown (open circles, dashed line). These two curves can be compared directly to (a) (where $d \sim 1/\rho$). Note that the pressure interval in (b) is three times the pressure interval in (a). Also included is the evolution of ρ with temperature (top x-axis) upon heating recovered HDA to obtain LDA (filled circles, solid line) (from [85]).

well known [83]. Thus, the density of recovered HDA, ρ(HDA), at $P = 1$ bar and $T = 77$ K can be calculated:

$$\rho(\text{HDA}) = \rho(\text{ice I}_h) \times h/(h - \Delta d),$$

where Δd is the measured difference in piston displacement at $P = 1$ bar before and after

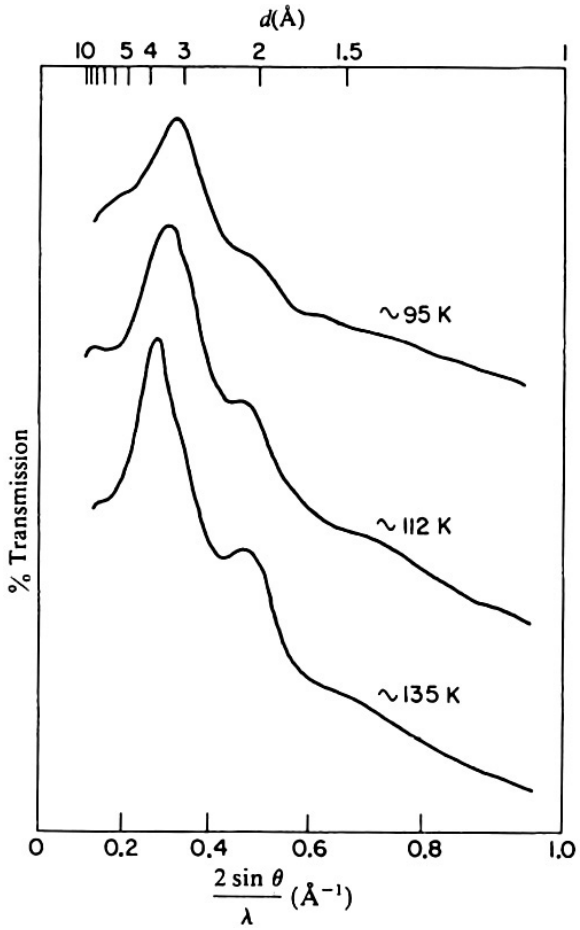

Figure 2. X-ray diffraction patterns at $P = 0$ GPa of recovered HDA at $T \sim 95$ K and $T \sim 112$ K, and LDA at $T \sim 135$ K. LDA is obtained upon isobaric heating of recovered HDA at $P = 0$ GPa (from [66]).

the compression/decompression cycle (which amounts to ∼2.5 mm in figure 1(a)), and h is the height of the ice I_h sample. If $m(\text{ice } I_h)$ is the mass of ice initially pipetted into the cold cylinder, and A is the cross-section of the bore, then h is given by

$$h = m(\text{ice } I_h)/(\rho(\text{ice } I_h) \times A).$$

It is necessary that the hexagonal ice has been precompressed before starting the cycle so that the loosely packed ice crystals obtained directly after pipetting reach roughly the density of a single crystal of ice I_h. It is also assumed that the diameter of the cylinder remains constant during the cycle, i.e., only uniaxial compression takes place. In the case shown in figure 1(a), the density of the sample at $P = 1$ bar and $T = 77$ K increases by ∼24%, from 0.94 g cm^{-3} (ice I_h) to 1.17 ± 0.02 g cm^{-3} (HDA). The latter density has been confirmed by weighing in liquid nitrogen [61, 84] and later by the independent method of buoyancy in a liquid Ar/N_2 mixture [68]. When calculating the densities of HDA at $P > 1$ bar from the measured Δd, it is necessary to take into account the elastic compression of indium, which causes a significant fraction of the piston displacement changes Δd upon (de)compression.

Therefore, it is necessary to determine in a separate experiment the displacement caused by the same amount of indium. This is the curve labelled 'Indium' in figure 1(a). The indium signal is then subtracted from the combined signal obtained from ice encased in indium, i.e., $\Delta d = \Delta d(\text{ice, indium}) - \Delta d(\text{indium})$. Because of the relatively high compressibility of indium and the need to correct for indium, isothermal compressibilities cannot be determined as reliably as isobaric thermal expansion coefficients. Mishima *et al* provide the value of $\rho = 1.31$ g cm^{-3} at $T = 77$ K and $P = 1.0$ GPa for HDA, and a value of $\rho \sim 1.42$ g cm^{-3} at $P = 1.75$ GPa and $T = 77$ K [66]. This implies an isothermal compressibility of 0.14 g cm^{-3} GPa^{-1} for HDA at $T = 77$ K.

The first results obtained from computer simulations to study glassy water were published in 1987, three years after the experiments by Mishima *et al* [85]. In this work, Tse and Klein perform molecular dynamics (MD) simulations using the TIP4P model [86] for water and show that (see figure 1(b)) (i) upon isothermal compression at $T = 80$ K, ice I_h undergoes a transition to HDA at high pressure and (ii) isothermal decompression of HDA at $T = 80$ K down to $P = 0$ GPa results in a *recovered* HDA of density 1.22 g cm^{-3}. The results (i) and (ii) agree qualitatively with the experiments performed by Mishima *et al* [66]. In experiments, the ice $I_h \rightarrow$ HDA transformation occurs at $P \sim 1.0$ GPa at $T = 77$ K, and the density of HDA is $\rho = 1.31$ g cm^{-3} at $P = 1.0$ GPa. The simulations of [85] show that the ice $I_h \rightarrow$ HDA transformation occurs at $P = 1.3$ GPa at $T = 80$ K, and the density of HDA at $P = 1.75$ GPa is $\rho = 1.34$ g cm^{-3}. After decompression of HDA, the experimental density of recovered HDA at $P = 0$ GPa is $\rho = 1.17 \pm 0.02$ g cm^{-3} at $T = 77$ K [66], while the corresponding density value in simulations is $\rho = 1.22$ g cm^{-3} ($T = 80$ K) [85].

2.2. LDA obtained upon isobaric heating of HDA at ambient pressure

2.2.1. Diffraction and densitometry experiments. A continuous relaxation process takes place upon heating HDA at ambient pressure at a heating rate of 2.6 K min^{-1}. The principal x-ray halo at ∼3.0 Å, characterizing HDA at $T = 77$ K (figure 2, upper trace), shifts almost linearly with temperature [66]. At $T \sim 112$ K, a partially relaxed state can be observed, and the corresponding principal x-ray halo shifts to ∼3.4 Å (figure 2, middle trace). That a continuous range of partially relaxed HDA samples *at ambient pressure* can be prepared in the temperature range ∼77–117 K was later also confirmed from combined neutron and x-ray diffraction studies [87–90]. Upon further heating, an exothermic transition to a second distinct amorphous state, denoted LDA, takes place at $T \sim 117$ K. This transition is accompanied by a spontaneous and sharp decrease in density. The principal x-ray halo peak is shifted from ∼3.0 Å (for HDA at $T = 77$ K) to ∼3.7 Å (for LDA at $T \sim 117$ K). At ∼135 K, a fully relaxed LDA state is observed, as indicated by the x-ray halo peak in figure 2, bottom trace. The overall heat of conversion from HDA to LDA at ambient pressure is 42 ± 8 J g^{-1} (757 ± 144 J mol^{-1}) [66]. Above $T \sim 152$ K, LDA crystallizes to ice I_c, which releases another 92 ± 15 J g^{-1} (1658 ± 270 J mol^{-1}) and causes the appearance of sharp Bragg peaks in the diffraction pattern (not shown). On further heating, ice I_c transforms into ice I_h and finally melts.

Figure 3 shows the evolution of density during the HDA → LDA transformation at $P = 20$ bar for a heating rate of ∼3 K min^{-1}. This trace can be directly compared to the trace obtained from simulations as shown in figure 1(b) (filled black circles). A decrease in density is observed in figure 3 upon heating HDA from $T \sim 85$ K up to $T = 137$ K in a piston–cylinder apparatus. The density of HDA decreases by $\Delta\rho = 0.06$ g cm^{-3} on heating just up to $T \sim 125$ K. This density change corresponds to a relaxation process. In fact, such a relaxation process occurs in addition to simple thermal expansion in the temperature region

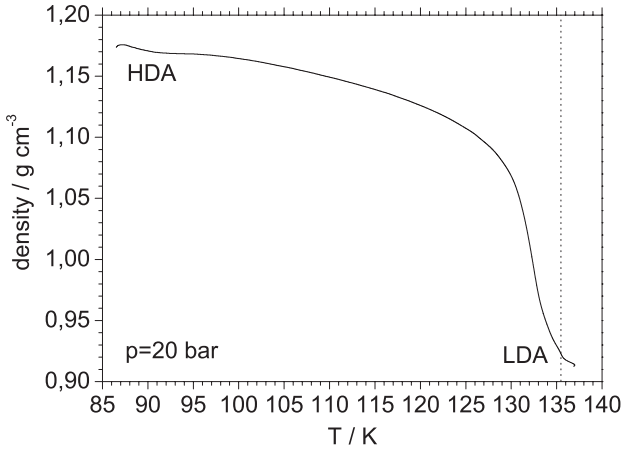

Figure 3. Evolution of density with temperature upon isobaric heating of HDA at $P = 2$ MPa. A relaxation process occurs in the range of temperatures 85–125 K. The HDA $\rightarrow$ LDA transformation occurs at $T \sim 132$ K. The dotted line indicates the temperature T_t at which the transformation to LDA is complete.

85–125 K at $P = 20$ bar. For comparison, we note that the density decrease due to simple thermal expansion of hexagonal ice between $T = 77$ and 250 K amounts to $\Delta\rho = 0.02$ g cm^{-3} ($\rho = 0.94$ g cm^{-3} at $T = 77$ K and $\rho = 0.92$ g cm^{-3} at $T = 250$ K) [83]. The sharp transformation from relaxed HDA to LDA then takes place in the temperature interval of $\sim$130–135 K and decreases the density suddenly to 0.92 g cm^{-3} at 135 K (20 bar). As a result of the 20-fold increase in pressure, the transition temperature to LDA has shifted by $\Delta T \sim +18$ K and $\Delta\rho \sim -0.02$ g cm^{-3} with respect to the values obtained at $P = 1$ bar ($\rho = 0.94$ g cm^{-3} and $T = 117$ K).

2.2.2. Density calculations from computer simulations. The HDA $\rightarrow$ LDA transformation obtained upon isobaric heating in the experiments is also observed in the computer simulations of Tse and Klein (filled circles in figure 1(b)) [85]: isobaric heating of recovered HDA at $P \sim 0$ GPa produces LDA; further heating of LDA results in liquid water. Whereas the transition from HDA to LDA takes place in a rather narrow temperature interval at the slow heating rates in experiment (see figure 3), the fast heating rates in the computer simulations result in a continuous loss of density in the temperature interval 77–140 K (see figure 1(b)).

The experimental density of LDA is $\rho = 0.94 \pm 0.02$ g cm^{-3} [61] at $P = 1$ bar and $T = 140$ K. In the simulations of [85], the density of LDA is $\rho = 1.06$ g cm^{-3} at $T = 142$ K and $P = 0$ GPa. This high value of density is probably due to the fast heating rate used in the simulations to obtain LDA. Recent longer MD simulations (using also the TIP4P model) indicate that the density of LDA at $P = 0$ GPa and $T = 80$ K is $\rho = 0.98$ g cm^{-3} [91]. The results observed in the computer simulations of Tse and Klein (i.e., the ice I_h $\rightarrow$ HDA transformation, the decompression of HDA back to normal pressure, and the HDA $\rightarrow$ LDA transformation at $P = 0$ GPa), together with the structural description of LDA and HDA that is also reported in their work [85], were confirmed nine years later by Okabe *et al* [92] using the same TIP4P model of water (see also [91]). The improvement of computers made it possible to perform longer simulations than those in [85]. The ice I_h $\rightarrow$ HDA transformation in the computer simulations of Okabe *et al* [92] lasts for about 400 ps, corresponding to a

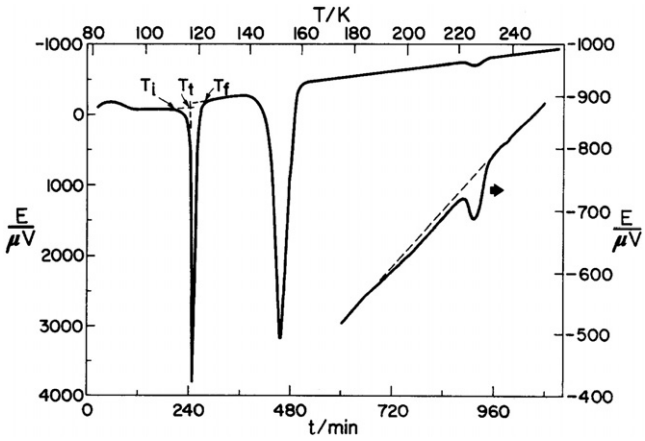

Figure 4. Voltage (microvolts) generated by the differential thermopile upon heating ∼2.7 g HDA sample at the rate of 10 K h^{-1}. The upper scale is the temperature of the sample corresponding to the time indicated by the abscissa. The left-hand ordinate corresponds to the main curve. The right-hand ordinate corresponds to the right-hand part of the curve, which shows the small peak at $T \sim 225$ K (main plot) in an expanded scale. T_i, T_t, and T_f are the temperatures at which the transformation from HDA to LDA was taken as initiating, transforming, and finishing, respectively (first sharp peak). LDA transforms to ice I_h at $T \sim 150$ K (second sharp peak), which transforms to ice I_c at $T \sim 225$ K (third peak) (from [94]).

compression rate of 2–4 MPa ps^{-1}. In the simulations performed by Tse and Klein, the number of molecules is only $N = 128$, and a typical compression run lasts only ∼130 ps. Besides the small system size and short simulation times, their results compare very well with experiments. Moreover, some results found in [85] were confirmed later in experiments. For example, in [85] it is found that if HDA is compressed to higher pressures (5–15 GPa) then the structure of HDA approaches that of ice VIII or ice VII. This prediction was later confirmed by experiments [93] showing that HDA transforms abruptly at $P = 4$ GPa and $T = 77$ K to a crystalline phase close to orientationally disordered ice VII and to a more ordered solid (ice-VIII-like) at higher temperatures.

2.2.3. Calorimetry experiments. Figure 4 shows the calorimetric trace obtained on heating HDA at ambient pressure in a Tian-Calvet calorimeter [94]. The HDA → LDA transformation corresponds to the sharp peak at $T_t = 114$ K. As discussed in section 2.2.1, Mishima *et al* [66] report a transition temperature of $T_t = 117$ K. The difference in conversion temperatures (114 K versus 117 K) is related to the difference in heating rates employed in [66] and [94]: 2.6 and 0.17 K min^{-1}, respectively. The continuous relaxation of HDA due to heating from $T = 77$ K up to $T = 114$ K is called 'exothermic relaxation' and the corresponding heat released over this broad interval amounts to approximately −220 J mol^{-1}. At the transition temperature $T_t \sim 114$ K, a sharp exotherm indicating the HDA → LDA conversion is found, which releases a heat of −530 J mol^{-1} (Mishima *et al* [66] report an amount of −757 J mol^{-1}). The second exotherm observed in figure 4 at $T_t' \sim 144$ K corresponds to the LDA → ice I_c transition, while the third tiny exotherm at $T_t'' \sim 225$ K indicates the ice I_c → ice I_h transition. The heat released in these exothermic transitions is −1380 J mol^{-1} (Mishima *et al* [66] report −1658 J mol^{-1}) and −20 J mol^{-1} plus an additional −20 J mol^{-1} from a broad pre-peak (see magnified inset figure 4), respectively.

The results shown in figure 4 indicate that HDA, as produced at $T = 77$ K by PIA, is a kinetically arrested non-equilibrium structure. On heating this state at $P = 1$ bar, a slow

enthalpy relaxation process to a relaxed HDA state first takes place. At $T = T_t$ enough thermal energy becomes suddenly available, and the relaxed HDA undergoes a sharp transition to LDA. At $P = 1$ bar HDA is thus metastable with respect to LDA, which itself is metastable with respect to ice I. The continuous relaxation process observed for 77 K $\leqslant T \leqslant T_t$ takes place in the same 'HDA megabasin' in configurational space and is determined by relaxation kinetics. The sharp transition at T_t, however, is an activated transition from HDA to the distinct LDA megabasin. The processes taking place on heating HDA at ambient pressure are best subdivided into three stages as suggested by Koza *et al* [89]: (i) kinetically driven annealing of HDA, (ii) a thermodynamically driven first-order-like transition to LDA, and (iii) kinetically driven annealing of LDA. The activation barrier for process (ii) has been estimated to be $\Delta E \sim 33$ kJ mol^{-1} [89].

Tulk *et al* [87] report neutron and x-ray structure factors for a finite number of amorphous states intermediate between HDA and LDA. However, the first diffraction peak of all of their intermediate states (obtained by annealing at temperatures up to 105 K) is relatively close to the diffraction peak of HDA and none of the intermediate states is relatively close to the diffraction peak of LDA (see figures 2 and 3 in [87]). It seems plausible, therefore, that all the intermediate states reported correspond to the states obtained during stage (i) and the sharp dip of the position of the first diffraction peak on annealing at $T > 110$ K corresponds to stage (ii).

2.2.4. Sound velocity and bulk/shear moduli measurements. In addition to diffraction methods (see figure 2), densitometry (see figure 3), and calorimetric methods (see figure 4), the transformation sequence HDA $\rightarrow$ LDA $\rightarrow$ ice I_c $\rightarrow$ ice I_h was also investigated by change of sound velocity and thermal conductivity [95] at pressures close to 1 bar. In particular, Gromnitskaya *et al* [96] performed sound velocity and bulk and shear moduli measurements at $P = 50$ bar, and observed a two-stage transformation of HDA to LDA, comprising an 'annealed stage' and a sharp transition at $T_t \sim 138$ K (see figure 5). This two-stage transformation is very similar to that shown in figure 3 [96]. The first stage (100 K $< T <$ 130 K) begins with a softening of the shear modulus G at $T \sim 100$ K and a softening of the bulk modulus B at $T \sim 110$ K (see figure 5(c)). Also, the transverse/longitudinal sound velocities (figure 5(a)) and the Poisson ratio (figure 5(d)) start to deviate significantly at $T \sim 100$ K. These results confirm the onset of the HDA to LDA transition at $T \sim 100$ K. Interestingly, during this first stage of the HDA $\rightarrow$ LDA transformation, the relative volume (figure 5(b)) changes only slightly, in agreement with the findings presented in figure 3. We note that even though the volume changes only slightly in the range 100–130 K some irreversible relaxation takes place. This softening of the elastic moduli in the first stage has been attributed to 'displacive rearrangement of the short-range order structure in HDA' [96].

At $T \sim 130$ K the sharp decrease of the density marks the end of the first stage of the transformation to LDA. This decrease in density causes minima in the sound velocities at $T \sim 130$ K (figure 5(a)), which clearly mark the onset of the sharp, second stage. The onset temperature for the sharp HDA $\rightarrow$ LDA transition of $T \sim 130$ K has also been confirmed by monitoring the thermal conductivity [95] of HDA samples *in situ* at pressures between 40 and 70 bar while heating[3]. The decrease in density and increase in sound velocity is complete at $T_t \sim 138$ K, which completes the second stage; pure LDA has formed. The results shown in figure 5 indicate that the HDA $\rightarrow$ LDA transition occurs at $T_t \sim 138$ K at $P = 50$ bar. At

[3] We emphasize that these 'HDA' samples have not been prepared by pressure-induced amorphization of ice I_h at 77 K, but rather by an elaborate protocol involving LDA as an intermediate stage. We surmise that their samples A and B might be rather VHDA, whereas sample C might resemble HDA. This may explain why the thermal conductivity plots shown in figure 1 of [95] show a plateau region between ~140 and 150 K in the case of samples A and B, but not in the case of sample C.

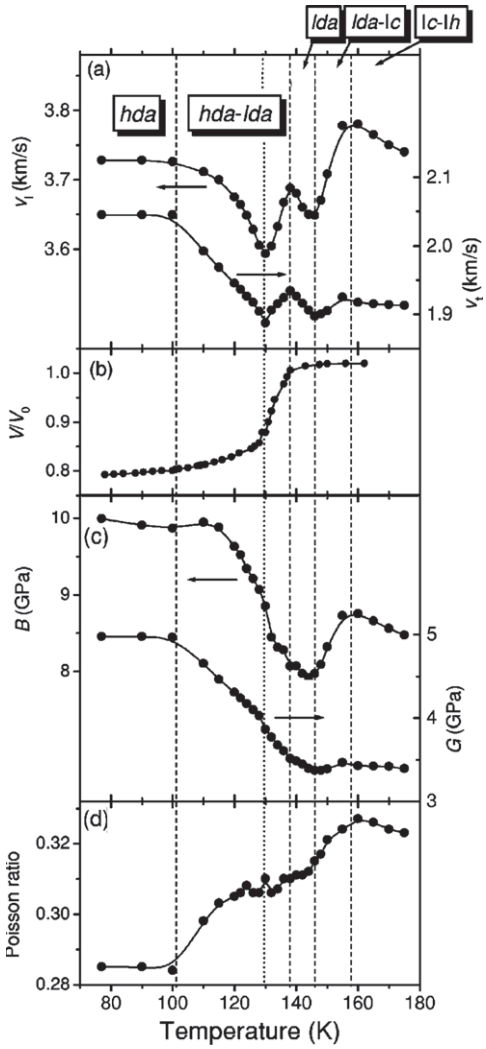

Figure 5. Properties of amorphous ices during the temperature-induced HDA → LDA transformation at $P = 0.05$ GPa. Temperature dependences of (a) the longitudinal (left ordinate) and transverse (right ordinate) sound velocities; (b) normalized volume; (c) bulk (left ordinate) and shear moduli (right ordinate); and (d) Poisson's ratio. Two stages can be identified: the dashed vertical lines at $T \sim 100$ K and $T \sim 130$ K correspond to the onset and end of HDA annealing ('the first stage'); the dashed vertical line at $T \sim 138$ K corresponds to the transformation temperature T_t to LDA ('end of second stage'). The dashed vertical lines at $T \sim 147$ K and $T \sim 158$ K correspond to the transformation to ice I_c and ice I_h (from [96]).

$P = 1$ bar $T_t \sim 117$ K [66]; at $P = 20$ bar $T_t \sim 135$ K (see figure 3). Thus, an increase in pressure at similar heating rates shifts the transition temperature to higher values.

The two-stage behaviour in the LDA → HDA transformation is in contrast to the observation of a single-stage transformation of ice I_h to HDA. In the case of the ice I_h → HDA transition, density, sound velocities, and elastic moduli start to change simultaneously (see figure 4 in [96]).

LDA finally transforms to ice I_c at $T \sim 147$ K, which can easily be seen in all panels of figure 5, except for figure 5(b), since the densities of LDA and ice I_c are roughly equal.

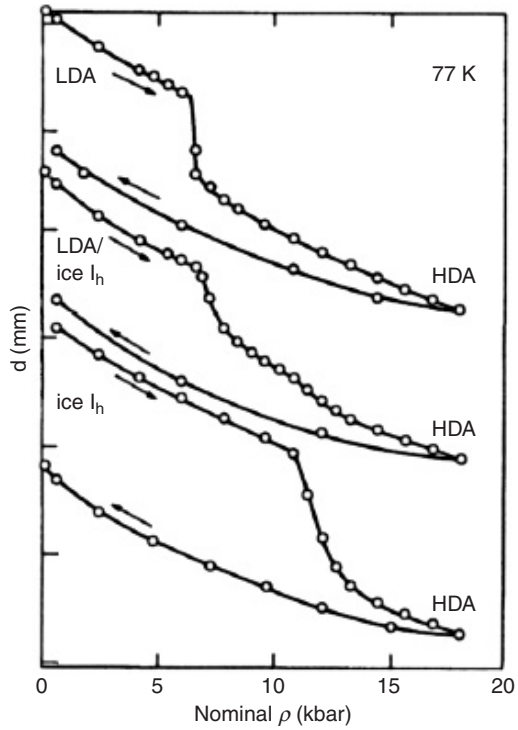

Figure 6. Piston displacement versus nominal pressure curves of three samples at $T = 77$ K. The first starting material is pure LDA (top curve; prepared by heating HDA at a rate of $\sim$1 K min^{-1} to $T = 132$ K at $P = 0.01$ GPa). The second starting material is a mixture of ice I_h and LDA (middle curve; prepared by heating HDA at a rate of $\sim$1 K min^{-1} to $T = 148$ K at $P = 0.01$ GPa). The third starting material is pure ice I_h (bottom curve; prepared by pipetting H_2O into a cold cup). All three starting materials are transformed to HDA after compression to 1.8 GPa and subsequent recovery. Curves are offset for clarity (adapted from [61]).

2.3. LDA ↔ HDA transformations upon isothermal compression/decompression

2.3.1. LDA → HDA transformation at $T = 77$ K. A year after the discovery of PIA of ice I_h, Mishima *et al* demonstrated that LDA can also be employed as a starting material for preparation of HDA [61]. The procedure remains the same as for the PIA of ice I: the starting material is kept at $T = 77$ K in a piston–cylinder apparatus and it is subjected to an increasing uniaxial pressure. As in the case of ice I, compression of LDA results in a sharp and apparently discontinuous transition that is accompanied by a large volume change ($\Delta V = -0.22$ cm^3 g^{-1}). Figure 6 shows the compression curves obtained on pressurizing LDA (top panel), an LDA/ice I_h mixture (middle panel), and ice I_h (bottom panel). The decompression curves of the resulting material are also included in figure 6. In the case of LDA, the sharp transition takes place at $P \sim 0.60 \pm 0.05$ GPa, approximately 60% of the pressure required for PIA of ice I. The transformation is not reversible, i.e. LDA is not recovered upon decompression. Instead, the density of the sample after decompression to $P = 1$ bar is $\sim$26% higher than that of LDA, and corresponds approximately to the density of recovered HDA obtained by PIA of ice I_h at $T = 77$ K. X-ray diffraction experiments confirm that compression of LDA results in HDA. The x-ray diffractogram of the recovered state [61] shows a broad principal halo centred at $\sim$3.0 Å, and is very similar to the halo of HDA obtained from ice I_h (figure 2).

The LDA → HDA transformation has been called 'a first-order-like transition'. This terminology seems to be justified since, despite the low temperature of $T = 77$ K, the transition is sharp and is accompanied by a large volume change. When a mixture of ice I and LDA is compressed (middle panel, figure 6), both transitions can be discerned, the LDA → HDA transition at $P \sim 0.6$ GPa and the ice I_h → HDA transition at $P \sim 1.0$ GPa.

2.3.1.1. Polyamorphism in substances other than water. The case of water provided the first example of an apparently first-order transition between amorphous solids. In the following years, the presence of more than one amorphous state (i.e. polyamorphism) has been observed in other substances, e.g., Si, C, SiO_2, GeS_2, and triphenyl phosphite [13, 49, 97]. The occurrence of at least two different solid amorphous states and the corresponding distinct liquid states is usually observed in systems showing anomalies in the liquid state, such as negative melting slopes dT_m/dp, negative thermal expansivity α_p (and hence, density maxima), and minima in the isothermal compressibility κ_T and the specific heat c_p [98]. For many substances showing such anomalies two distinct amorphous states, often called LDA and HDA, have been found. With the notable exception of liquid phosphorus [99], the critical temperature T_c of the liquid–liquid phase transition occurs only in the supercooled region.

Molten silica (SiO_2) is exceptional just like water since there might be more than one transition between amorphous/liquid states. It can be supercooled easily to form a glass. Amorphous silica can also be prepared by pressure- or temperature-induced amorphization of crystals [100–103], and amorphous–amorphous transitions in silica have been reported [104, 105]. The low-density amorph can be densified permanently by up to 22% at pressures up to 20 GPa without destroying the tetrahedral coordination [106–108]. Upon compression up to 42 GPa the Si–O distance approaches the distance corresponding to the structure of stishovite, from which octahedral coordination is inferred [109, 110]. How many polyamorphic transitions occur in SiO_2 is unclear; there might be one transition related to the LDA–HDA transition within four-coordinated structures, another transition on the switch to an octahedral structure, and yet another one called a clathrate type transition, which could even be at negative pressures. It is also unclear if these transitions are first-order-like transitions or just continuous transformations. Lyapin *et al* provide evidence against a first-order-like nature of the polyamorphic transitions in amorphous SiO_2 [111].

Besides the density- or entropy-driven polyamorphic transitions that are induced by increasing either pressure or temperature, respectively, a third type of polyamorphism can be found when moving into the composition axis, i.e., in systems containing more than one chemical constituent (e.g., in binary Na_2O–SiO_2 or ternary Al_2O_3–CaO–SiO_2). All these minerals are important in Earth's mantle. The so called 'compositional polyamorphism' is a sudden unmixing of the constituents on changing mole fractions, i.e. a miscibility gap in the metastable state. This effect is for instance made use of when producing Vycor glass equipment. In systems containing SiO_2 the maximum temperature of unmixing, e.g. 1150 K for Na_2O–SiO_2, is found at 90 mol% SiO_2 [112]. This temperature is reduced to about 800 K when moving to the pure pole of SiO_2, which happens to be close to the postulated LDA–HDA transition temperature of amorphous SiO_2. The preceding discussion clearly indicates that understanding the polyamorphism in water can help our understanding of polyamorphism in general.

2.3.2. Reversible LDA ↔ HDA transformation at $T \sim 135$ K. The pressure-induced LDA → HDA transition has also been continuously monitored in terms of elastic moduli and ultrasonic velocity [96], as well as thermal conductivity [113]. These experiments show that at

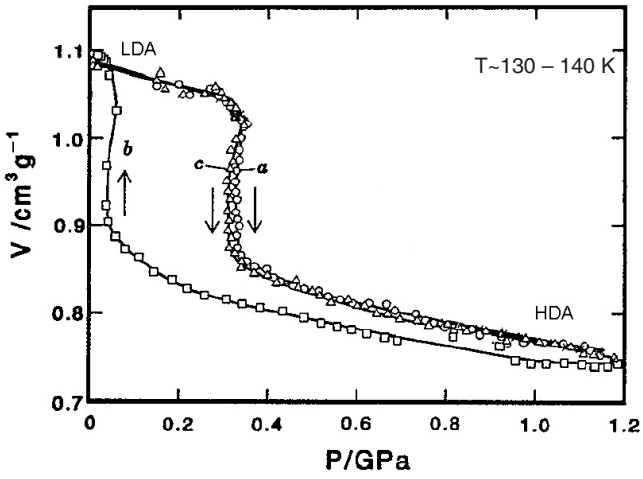

Figure 7. (a) Compression of LDA to obtain HDA, (b) successive decompression of HDA, and (c) subsequent recompression of LDA; $T = 130$–140 K; compression rate $r \sim 0.6$ GPa min^{-1} (from [114]).

$T \sim 110$ K LDA transforms to HDA at $P \sim 0.40$ GPa, i.e. two-thirds of the pressure required to transform LDA at $T = 77$ K [96, 113]. When LDA is compressed at $T \sim 135$ K, the sharp LDA $\rightarrow$ HDA transition occurs at $P \sim 0.20$ GPa, i.e. one-third of the pressure required to transform LDA at $T = 77$ K [114]. Therefore, the pressure at which LDA transforms to HDA decreases as the compression temperature increases. It has been estimated that the equilibrium pressure for the LDA $\rightarrow$ HDA transformation is about $P = 0.18$ GPa at temperatures ranging from 77 K to just below the crystallization temperature T_X [81]. Therefore, it seems that at $T = 77$ K overpressurization by a factor of three is necessary to transform LDA into HDA, whereas at $T \sim 135$ K the equilibrium pressure is almost reached.

The compression/decompression curves obtained during the LDA $\leftrightarrow$ HDA transformation at $T \sim 135$ K are shown in figure 7. A comparison of figures 7 and 6 shows that by increasing the compression/decompression temperature from $T = 77$ K to $T \sim 135$ K the LDA $\rightarrow$ HDA transition can be reversed. The transition from HDA back to LDA occurs at $P \sim 0.05$ GPa at $T \sim 135$ K and shows hysteresis.

Figure 8 shows the phase diagram of ice, together with the lines corresponding to the compression-induced LDA $\rightarrow$ HDA transition and the decompression-induced HDA $\rightarrow$ LDA transition, as well as the temperature-induced HDA $\rightarrow$ LDA and temperature-induced LDA $\rightarrow$ HDA transitions. A similar phase diagram has also been presented elsewhere (see figure 8 in [96]).

A hysteresis such as that observed in the compression/decompression experiments of LDA conducted in the range $125 \text{ K} \leqslant T < 150$ K is not unusual for first-order phase transitions. For instance, crystal–crystal phase transitions also show a pronounced hysteresis. In figure 8 the ice $I_h \leftrightarrow$ ice II transitions at $T = 170$ K are shown to occur at $P \sim 0.3$ GPa on compression, and at $P \sim 0.05$ GPa on decompression. This hysteresis is comparable to that observed in the LDA $\leftrightarrow$ HDA transition at $T \sim 135$ K. Thus, the presence of hysteresis has been used as evidence for a first-order-like nature of the LDA $\leftrightarrow$ HDA transition [114]. On the other hand, at $T = 220$ K, just a slight hysteresis remains in the ice $I_h \leftrightarrow$ ice II phase transitions (i.e., the higher the temperature, the shorter the time for equilibration and the less pronounced the hysteresis is), while the hysteresis is still evident in the LDA $\leftrightarrow$ HDA transition at $T = 135$ K.

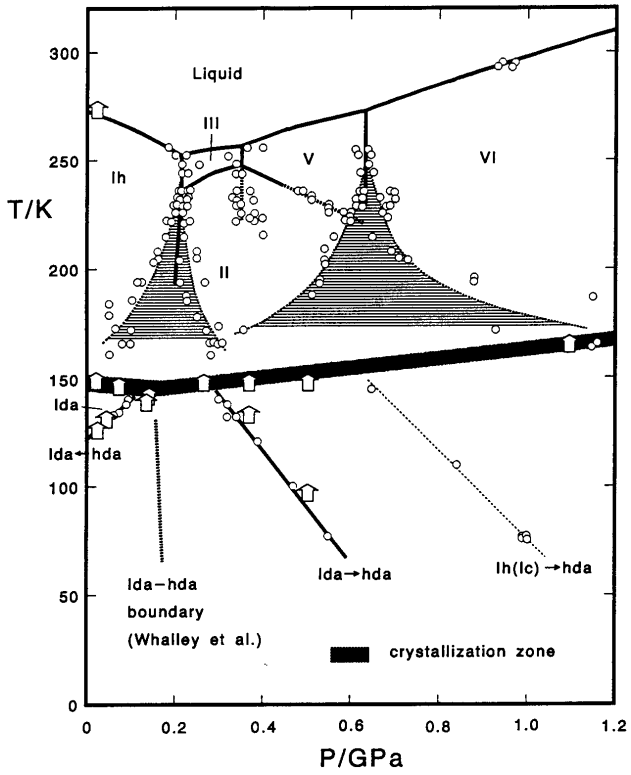

Figure 8. Phase diagram of LDA and HDA. Open circles indicate pressure-induced transitions and temperature-induced transitions are indicated by arrows. The thick black line marks the crystallization temperature. Below this temperature amorphous–amorphous transitions are indicated, whereas above this temperature crystal–crystal transitions are indicated. For pressure-induced transitions a pronounced hysteresis is found both for the LDA $\leftrightarrow$ HDA transition and for crystal–crystal transitions, e.g. the ice Ih $\leftrightarrow$ ice II or the ice V $\leftrightarrow$ ice VI transition. Phase transitions were identified by sudden volume or temperature changes. Recovered phases were identified by x-ray photographs (from [114]).

Therefore, the hysteresis on decompression has also been employed to argue against a first-order, abrupt, and reversible transformation between HDA and LDA at $P \sim 0.20$ GPa and 130 K $\leqslant T \leqslant$ 140 K [95].

We emphasize that it is quite astonishing that two metastable amorphous states can reversibly be converted into each other at temperatures as low as 77 K $\leqslant T <$ 150 K. The fact that the reversibility occurs with hysteresis implies that there are kinetic limitations. A similar kinetic limitation is also found for instance for melt–freeze cycles of ice I_h: ice I_h melts at $T = 273$ K and $P = 1$ atm, but on cooling it may not freeze, but remain in the supercooled state, down to $T \sim 235$ K. That is, because of the kinetic limitation provided by ice nucleation and growth, the melting transition of ice I_h is not reversible at the same temperature and pressure—still, it is a prime example for a reversible, abrupt first-order phase transition [115].

2.3.3. Isothermal LDA $\leftrightarrow$ HDA transformation from computer simulations. The work of Tse and Klein [85] shows how results from computer simulations can complement the experimental

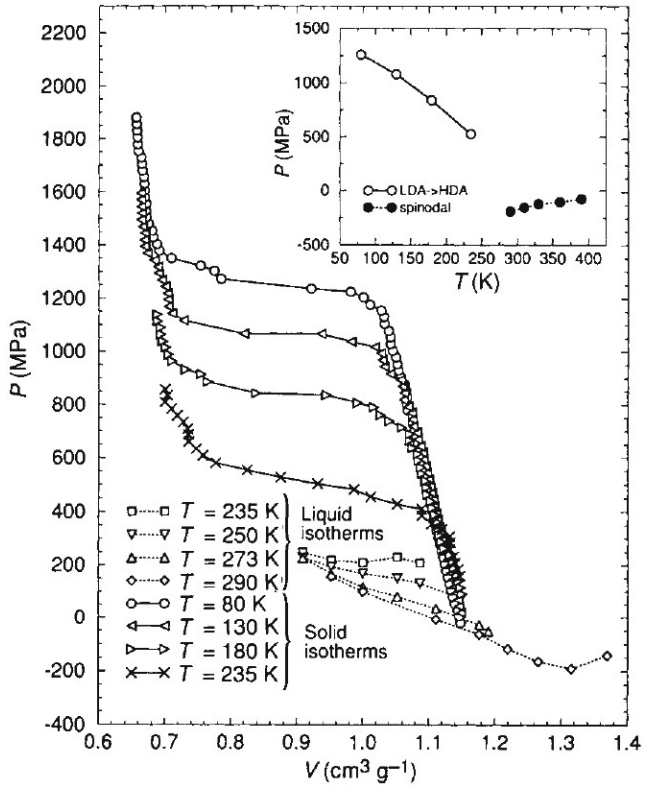

Figure 9. Solid lines: isothermal compression curves for LDA in the temperature range 80–235 K calculated using the ST2 potential. The curves start at a molar volume of $V \sim 1.15$ cm^3 g^{-1} and a pressure $P = 0$ MPa. The plateau region indicates the amorphous–amorphous transition to HDA. Dotted lines: isothermal compression curves at $T > 235$ K for liquid water, which do not show a transformation involving decrease in molar volume. Inset: location of the phase boundary between LDA and HDA predicted from ST2-water MD simulations (white circles), and the line of instability, where spinodal decomposition takes place (black circles) (from [60]).

results and can help us to understand glassy water behaviour. By the time their work was published, it was not clear how much computer simulations would influence our view of the phase diagram of amorphous ice. In 1992, Poole *et al* [60] performed MD computer simulations using the ST2 model for water [116] in both the liquid and glassy states. They observed an isothermal LDA $\rightarrow$ HDA transformation at $T = 80$, 130, 180, and 235 K (the corresponding compression curves are shown in figure 9). The sharp change of the molar volume, indicating the LDA $\rightarrow$ HDA transition, occurs at $P \sim 1.3$ GPa at $T = 80$ K, and at $P \sim 1.1$ GPa at $T = 130$ K. These results are in qualitative agreement with the experimental data ($P \sim 0.6$ GPa at $T = 80$ K and $P \sim 0.2$ GPa at $T = 135$ K), but do not agree very well quantitatively, probably due to the simplicity of the model and to the high compression rates used in simulations that may result in overpressurization. At temperatures above $T \sim 150$ K crystallization takes place in experiments, whereas in MD simulations using the ST2 model the LDA $\rightarrow$ HDA transformation can be observed up to $T = 235$ K. Increasing the compression temperature to $T = 180$ K and $T = 235$ K lowers the onset pressure for the simulated LDA $\rightarrow$ HDA transformation to $P \sim 0.9$ GPa and $P \sim 0.5$ GPa, respectively.

Table 1. Density of HDA obtained upon compression of LDA from experiments and computer simulations using different water models. As we discuss in section 3.2.1, recent computer simulations using the TIP4P [91] and SPC/E [118] show that HDA recovered from different high pressures is characterized by a range of densities at $P = 0$ GPa (and not by a single value of ρ).

	Experimental	TIP4P	SPC/E	ST2
1 bar	1.15–1.19 [68, 114]	∼1.21[a] [91]	∼1.2[a] [118]	1.37 [117]
1.4 GPa	1.37 [114]	1.34 [91]	1.31 [118]	1.45 [117]

[a] Approximated values.

The simulations of reference [60] in the glassy state reproduce only the LDA → HDA transformation. The isothermal decompression of HDA, to investigate the properties of recovered HDA and the HDA → LDA transformation, were investigated by computer simulations in subsequent works. The isothermal LDA → HDA and subsequent HDA → LDA transformations, using the ST2 and TIP4P potentials, are studied in [117]. Results using the SPC/E model are reported in [118]. The trajectories of the system in the P–ρ plane during the LDA ↔ HDA cycle, for the ST2, TIP4P, and SPC/E potentials, are reproduced in figure 10.[4] The similarities between these results at positive pressures and those reported from experiments at $T = 77$ K, shown in figure 6, are remarkable. The densities of HDA at $T \sim 77$ K and $P = 1$ bar and 1.4 GPa, from experiments and computer simulations, are summarized in table 1.

The values in table 1 indicate that the TIP4P and SPC/E models are better than the ST2 potential to reproduce the LDA ↔ HDA transformation. Moreover, the LDA → HDA transformation in the case of the ST2 model is quite abrupt, as compared with the TIP4P and SPC/E potentials and experiments.

In experiments, the LDA ↔ HDA transformation is reversible at $P > 0$ GPa when the compression/decompression temperature is $T = 135$ K [114]. In simulations, the LDA → HDA transformation is reversible if negative pressures are considered (figure 10). In general, increasing the compression/decompression temperature reduces the pressure characterizing the LDA → HDA transformation, and increases the pressure of the HDA → LDA transformation. Thus, the hysteresis in the LDA ↔ HDA transformation diminishes as the compression temperature increases, which is consistent with the experimental results shown in figure 8. Although the LDA ↔ HDA transformation is reversible in simulations when looking at the trajectory of the system in the P–ρ plane, simulations using the TIP4P [117] and SPC/E [119] models indicate that the potential energy, potential energy landscape properties [120–122], and structure of the amorphous ice at low density recovered upon decompression of HDA differ from those of the starting LDA (before compression). These results suggest that LDA might not be a unique glassy state, but that it might represent a 'family' of low-density glassy states, all with a similar structure.

2.3.4. The liquid–liquid first-order transition hypothesis.

2.3.4.1. The hypothesis. Besides reproducing the LDA ↔ HDA transition, the simulations of Poole *et al* [60] in the *liquid* phase also show (i) the presence of a density anomaly (i.e. a range of temperatures where the density decreases upon isobaric cooling) and (ii) an anomalous increase of the response functions (compressibility κ_T and specific heat c_p) upon cooling, which

[4] LDA is not obtained from isobaric heating of HDA at $P = 0$ GPa, but by isochoric cooling of a low-density ($\rho \sim 0.9$ g cm^{-3}) and low-temperature equilibrated liquid. The RDF of the LDA obtained in this way is in agreement with experiments (see e.g., [60]).

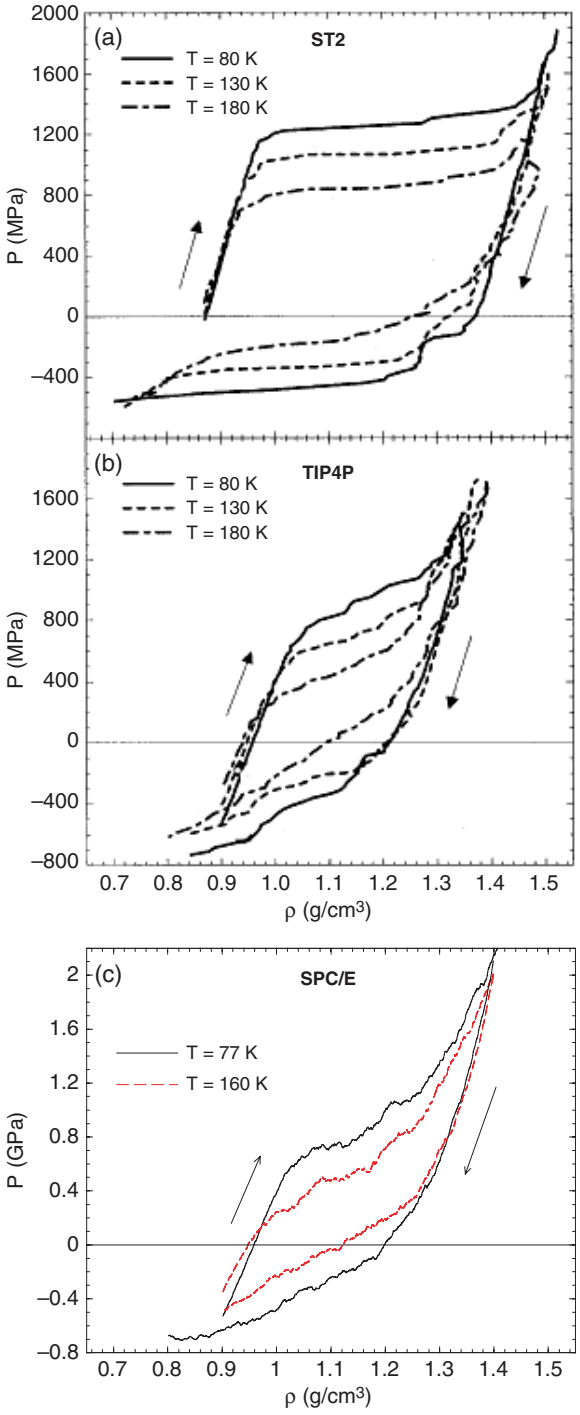

Figure 10. Isothermal compression curves during the LDA → HDA transition and subsequent isothermal decompression curves of HDA. HDA transforms back to LDA at negative pressures. Results are from MD simulations using (a) the ST2, (b) TIP4P, and (c) SPC/E models of water ((a) and (b) taken from [117]; (c) adapted from [118]).

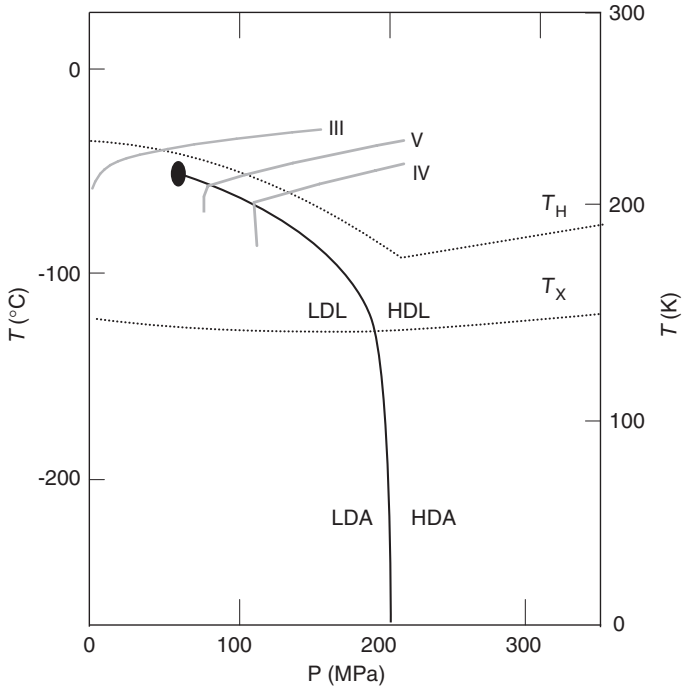

Figure 11. Schematic representation of the phase diagram showing the hypothesized first-order liquid–liquid phase transition. The first-order transition line separates LDA and HDA, at low temperature, and the low- (LDL) and the high-density liquid (HDL), at high temperature. This line ends at the hypothesized (second) critical point. Grey lines are the experimental determination of the melting curves of ice III, ice IV and ice V as observed by the onset of a change in sample temperature. In agreement with the liquid–liquid phase transition hypothesis, only the melting curves of ice IV and V show a discontinuous change of slope, the melting curves of ice III being continuous. The area above the crystallization temperature T_X and below the homogeneous nucleation temperature T_H is called 'no man's land'. Observation of disordered states has so far not been possible in the 'no man's land' (adapted from [130]).

is consistent with experimental results [4, 123–126]. In addition, they show that (iii) there is no re-entrant spinodal (i.e., the pressure of the liquid-to-gas spinodal decreases monotonically upon cooling).

To explain the LDA $\leftrightarrow$ HDA transformation, together with the findings (i)–(iii) in the liquid state, Poole *et al* [60] propose the phase diagram for metastable water (i.e. supercooled liquid and amorphous ice) shown in figure 11. In this phase diagram, LDA and HDA are separated by a first-order transition line. This line extends, at higher temperatures, into the supercooled liquid region separating two liquid phases (low-density (LDL) and high-density liquid (HDL)), and ends in a second (metastable) critical point (CP) (filled black circle in figure 11). Below the second CP, the transformation between the two liquids is accompanied by a discontinuity in density. Above the second CP, such a discontinuity in density can no longer be observed. Instead, there would be strong density fluctuations in the area close to the second CP. In the proposed phase diagram, LDL and HDL are the liquids connected by cooling to LDA and HDA, respectively (in these cases, the thermodynamic paths from HDA to HDL and from LDA to LDL do not intersect the first-order transition line).

The results of reference [60] showed, for the first time, that (a) the 'stability-limit conjecture' [127–129] proposed to explain the anomalous behaviour of supercooled water

Table 2. Location of the second CP obtained from MD simulations using different water models. Monte Carlo simulations in the Gibbs and restricted density-fluctuation ensembles, neglecting the LRCI beyond a cut-off distance, show multiple CPs (in addition to the liquid–vapour CP) for the present water models (see section 3.2.2.3).

	ST2	TIP5P
$P_{c'}$ [GPa]	0.18[a]	0.34[b]; 0.31[c]
$T_{c'}$ [K]	245[a]	217[b]; 210[c]
$\rho_{c'}$ [g cm^{-3}]	0.94[a]	1.13[b]; 1.09[c]

[a] From [132].
[b] From [58] (simulations using the reaction field technique to treat the long-range Coulombic interactions).
[c] From [135] (simulations using the reaction field technique to treat the long-range Coulombic interactions).

(see e.g. [5, 7, 10]) does not agree with simulations using the ST2 model; and that (b) the liquid anomalies and the polyamorphism observed in water can both be explained as a result of a single phenomenon: the presence (in the metastable regime) of a first-order transition line ending in a second CP. Evidence suggesting the possibility that LDL and HDL are separated by a first-order transition line was obtained originally by Mishima *et al* [61] (see also section 2.3.4.2). Mishima later also showed that D_2O shows a very similar behaviour [130]. A detailed interpretation of the phenomenology associated with the LDA $\leftrightarrow$ HDA and the liquid $\leftrightarrow$ amorphous ice transformations in terms of the phase diagram proposed in figure 11 is given in [131]. Nowadays, most of the MD simulations in the liquid and glassy state, such as those performed in [60], are shorter than the time needed for the system to crystallize. Thus, in simulations, one connects the liquid and the glass state by cooling and heating, with no intermediate crystal phase. This is not the case in experiments, where heating the amorphous state above the crystallization temperature T_X (see figure 11) or cooling the liquid below the homogeneous nucleation temperature T_H (see figure 11) usually results in crystallization.

Recent high-resolution MD simulations [132] using the ST2 potential confirm the presence of the second CP (see also [133]). MD simulations performed using the TIP5P model [134], treating the long range interaction with a cut-off [58] or using the Ewald sum method [135], also find a second CP, together with a density anomaly, and a non-re-entrant spinodal. The location of the second CP obtained from different MD simulations is summarized in table 2.

Table 2 shows that, in computer simulations, the second CP is located at $P \sim 0.18$–0.34 GPa and $T \sim 210$–245 K. Tanaka [136, 137] performed MD simulations using the TIP4P model and found a sharp change in density and potential energy upon cooling the system at constant pressure in the range $P \sim 0.1$–0.2 GPa. He interpreted his results as indicative of the presence of a liquid–liquid spinodal at low temperature; at $P = 0.1$ GPa, the spinodal temperature was estimated as $T_s \sim 213$ K. Accordingly, he proposed the existence of a second CP in the phase diagram of the TIP4P model but he located it at negative pressures, at $P_{c'} \sim -0.1$ GPa and $T_{c'} \sim 250$ K. However, subsequent MD simulations [138] also using the TIP4P model showed that at $T = 200$ K $< T_s$ there is no liquid–liquid transition line. At present, direct evidence of a second CP in MD simulations using the TIP4P model has not been reported.

MD simulations using the SPC/E model, at the lowest temperatures accessible in simulations, do not show such a second CP [138, 139]. Sciortino *et al* [140] performed theoretical calculations based on the potential energy landscape approach combined with numerical data from MD simulations using the SPC/E model in the liquid state. Their calculations indicate that a second CP exists in the phase diagram of the SPC/E model located

between ∼140 and 175 K and between ∼0.185 and 0.340 GPa. These results are in agreement with previous estimations of the location of the second CP (also based on the SPC/E model) obtained by extrapolation of the liquid free energy to low temperatures [141].

The liquid–liquid first-order transition hypothesis is not the only possible explanation for the anomalies in liquid water and the polyamorphism in amorphous ice. At least two other explanations have been proposed to explain water's behaviour: the 'stability-limit conjecture' [128] and the 'singularity-free scenario' [142]. In the stability-limit conjecture, the liquid–gas spinodal, that is born at the liquid–gas critical point located at $T = 647$ K and $P = 0.022$ GPa, decreases monotonically in the P–T plane upon cooling, reaches a minimum at negative pressure, and re-enters the positive P domain, crossing the $P = 0$ GPa axis at low temperature. In this view, the anomalous increase of the response functions observed in liquid water at normal pressure is a consequence of approaching the re-entrant spinodal upon cooling. The concept of a re-entrant spinodal is in disagreement with MD computer simulations of different water models such as ST2, TIP4P, and TIP5P models [58, 117]. In the singularity-free scenario, the liquid water anomalies are explained in terms of thermodynamic relationships and the existence of a density anomaly [142, 143]. It is shown that thermodynamics requires the increase of response functions upon cooling the liquid due to the presence of the density anomaly. In both the stability-limit conjecture and singularity-free scenario, there is no postulated second CP. Therefore, the LDA ↔ HDA transformations are interpreted as a continuous transformation.

Much theoretical work has been performed to investigate the different scenarios proposed to explain water behaviour. Examples include simplified analytical models [144–146], lattice models [147–149], two-state models [150–153], field theoretic models [154], and models involving the competition of two local orders (density and bond ordering) [155–159]. It is not the goal of the present discussion to summarize the works in favour of or against the liquid–liquid first-order transition hypothesis. Such a discussion goes beyond the scope of this work. For a more detailed discussion in this respect we refer to [9, 10, 160].

2.3.4.2. Indirect experimental evidence of the liquid–liquid first-order transition hypothesis. Computer simulations indicate that the second CP could be located at $P_{c'} \sim 180$–340 MPa and at $T_{c'} \sim 210$–245 K (see table 2). Transitions in the liquid state in this P, T range are hard to investigate experimentally. This is because (see figure 11) (i) amorphous ice immediately crystallizes on heating above $T_X(P)$ (e.g., $T_X = 150$ K at $P = 1$ bar, and $T_X = 180$ K at $P = 1.0$ GPa) and (ii) supercooled liquid water immediately crystallizes below the homogeneous nucleation temperature $T_H(P)$ (e.g., $T_H \sim 232$ K at $P = 0.1$ MPa [161], and $T_H \sim 181$ K at $P = 0.2$ GPa [162]). The temperature range between T_X and T_H, where only crystalline ice has been observed, is called the 'no-man's land'. Since the no-man's land also encompasses the hypothesized second CP, experiments testing directly the second CP or the LDL ↔ HDL transition (at $T_X < T < T_H$) are not possible in the supercooled state.

Mishima and Stanley provided an indirect experimental confirmation of the liquid–liquid first-order transition hypothesis by recording the *decompression-induced* melting lines of high-pressure ices [160, 163]. Figure 11 shows the decompression-induced melting lines of ice III, IV and V. The melting curve of ice III is smoothly curved, while the melting curves of ice IV and ice V undergo an abrupt change of slope. These results are consistent with the liquid–liquid first-order transition hypothesis. Since the ice III melting line runs above the hypothesized second CP, it shows a smooth curvature. On the other hand, the melting lines of ice IV and ice V run below the second CP and cross the postulated liquid–liquid transition line. Therefore, these melting lines show an abrupt change in curvature. However, we note that these results are not conclusive evidence of a liquid–liquid first-order transition; it has been emphasized

that it is very difficult to distinguish experimentally between a sharp but continuous and a discontinuous transition [10, 164]. In [160], Mishima and Stanley construct the Gibbs free energy of supercooled water from which they estimate the location of the second CP to be at ∼0.1 GPa and $T \sim 220$ K.

The possibility remains open, though, that there is a *deeply* supercooled liquid regime in the temperature range below the 'no-man's land'. If so, the liquid–liquid transition could, in principle, be observed experimentally. This requires that the amorphous state experiences a glass-to-liquid transition prior to its crystallization, i.e. that the glass transition temperature T_g lies below T_X. In the case of LDA (or HGW, ASW) a lot of work has been done to investigate whether there exists a deeply supercooled liquid regime. When heating HGW at *normal pressure*, a small step-like change in the heat capacity (amounting to $\Delta c_p \sim 0.7$ J K^{-1} mol^{-1}) occurs at a temperature of $T \sim 136$ K [165–168]. In the case of LDA, such a step-like change occurs at $T = 134 \pm 2$ K, at a heating rate of 30 K min^{-1} [169], and at $T = 124$ K, at a heating rate of 0.17 K min^{-1} [170]. Therefore, a value of $T_g \sim 136$ K (which is ∼15 K below T_X) has been attributed to the glass transition temperature from LDA (or HGW) to LDL at *normal pressure*. Experiments also indicate that the diffusive mixing in LDA is significantly enhanced at $T = 150$ K, and thus are also consistent with a value of $T_g \sim 136$ K [171]. Please note that there is still some scientific discourse about the value of T_g since comparison of the glass transition behaviour of LDA with inorganic glasses suggests that the features observed at $T \sim 136$ K could be a 'shadow transition', whereas the real glass transition might be in the 'no-man's land' at $T \sim 165$ K [11, 172, 173].

Much less is known about the glass transition temperature of HDA (or VHDA; section 3), since high-pressure experiments are difficult to perform. At least two experiments suggest that, also at high pressure, $T_g < T_X$. In [174], Mishima performs experiments decompressing an emulsion of amorphous ice from 1.05 GPa at constant $T \sim 160$ K. He observes a reproducible small decrease in temperature at $P \sim 0.4$ GPa, prior to crystallization (see figure 1 in [174]). This endothermic event is attributed to the glass transition to HDL at $P_g \sim 0.4$ GPa (and a corresponding $T_g \sim 160$ K). Similar experiments on emulsified LiCl aqueous solutions suggest that this slight decrease in temperature indeed corresponds to the pressure-induced glass transition.

In [175], Andersson performs a set of dielectric relaxation measurements and concludes that the relaxation time of amorphous ice at $P = 1.0$ GPa amounts to $\tau = 1$ s at 140 K, and $\tau = 30$ ms at 150 K (see figure 4 in [175]). These results indicate that, at $P = 1$ GPa, the amorphous ice is, in fact, an ultraviscous liquid at 140 K $< T <$ 160 K, and that the glass transition temperature at $P = 1$ GPa is below $T = 140$ K. Andersson also finds that the relaxation times at $P = 0.4$ GPa are quite similar to the relaxation times at $P = 1.0$ GPa, so that $T_g < 140$ K also at $P = 0.4$ GPa. Although this value of $T_g < 140$ K is lower that the $T_g \sim 160$ K obtained by Mishima, both experiments [175] indicate that at high pressure $T_g < T_X$.

In summary, the liquid–liquid first-order transition hypothesis has not been confirmed by direct experiments and its existence is still under debate (e.g., see [10]). The location of the second CP is estimated to fall in a range of temperatures and pressures where experimental liquid water crystallizes, and only indirect experimental evidence could be found supporting its presence in bulk water [160], in water confined to nanopores [176, 177] and in interfacial water [178]. The simplicity and elegance of the liquid–liquid first-order transition hypothesis is appealing, and even if the second CP can never be observed, one can still interpret the computer simulation results as indicative of the presence of a *virtual* second critical point: its presence being the cause of water's liquid anomalies and polyamorphism. Such a *virtual* second critical point would be observed hypothetically if the unavoidable crystallization did not occur.

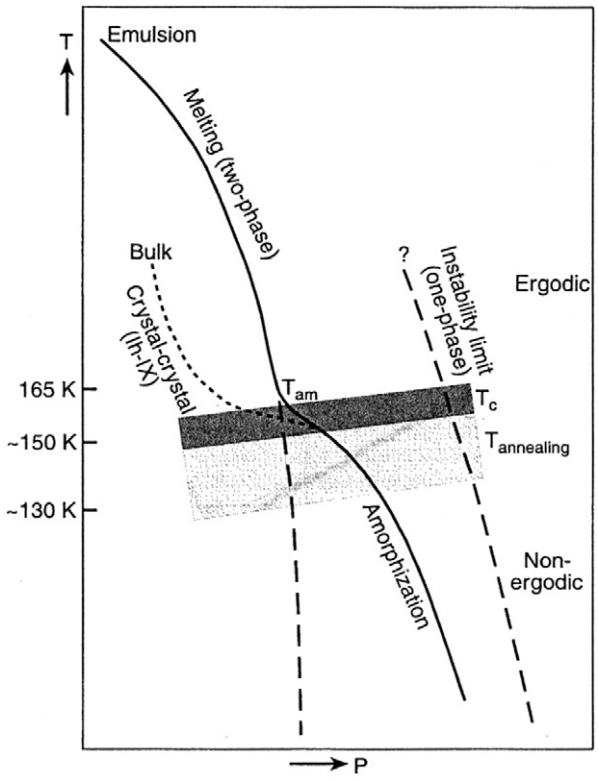

Figure 12. The pressure-induced melting/amorphization line of emulsified ice I_h (solid line), and the crystal–crystal transformation observed in bulk ice I_h (short-dashed line). Transition pressures were obtained by detecting a decrease in sample volume or a change in sample temperature. The dark grey shaded area denoted by T_c corresponds to the crystallization temperature of 'HDA'. The light grey shaded area denoted by $T_{annealing}$ corresponds to 'annealed states of HDA'. Above T_c, ice I crystallizes while emulsified ice melts into a liquid. Below T_c, both emulsified ice and ice I_h transform into HDA (at the same temperature and pressures). The long-dashed line at low pressures corresponds to the extrapolated thermodynamic melting line. The long-dashed line at high pressures marked with '?' corresponds to a possible spinodal, at which spontaneous one-phase decomposition is thought to occur (from [78]).

3. Very high-density amorphous ice (VHDA)

3.1. Three routes to produce VHDA

3.1.1. Isothermal compression of ice I at $T \sim$ 130–165 K. In section 2.1, we discuss how HDA can be obtained by PIA of ice I at $T = 77$ K. The effect of compressing ice I at $T > 77$ K has been studied by Mishima [78] (at $T < 270$ K) and by Lyapin *et al* (at $T < 200$ K [179]). Experiments monitoring the thermal conductivity *in situ*, at $T = 130$ K, as measured using a transient hot wire method, have been performed by Johari and Andersson [95]. All these studies agree that at $T < 165$ K PIA takes place, whereas at $T > 165$ K an ice $I_h \rightarrow$ ice IX transformation is observed in bulk samples (see the dotted line in figure 12).

Emulsions allow one to study liquid water at temperatures lower than the crystallization temperature of bulk water, i.e. emulsions suppress the crystal nucleation at low temperatures. When ice I emulsions are compressed at $T > 165$ K, instead of ice IX emulsions, a liquid

phase is reached (see the solid line in figure 12). However, at $T < 165$ K, even compressing ice emulsions results in a crystal → amorph transition. Thus, as the temperature is raised, a crossover from amorphization to equilibrium melting occurs on pressurizing ice emulsions, while a crossover from amorphization to a crystal–crystal transition occurs for bulk ice I. The same crystal → amorphous ice transition line is obtained upon compression of ice I and ice emulsions.

At temperatures from $T \sim 130$ K to $T \sim 165$ K (grey shaded area of figure 12), a smooth crossover from sluggish amorphization to equilibrium melting is seen. In this temperature range, 'ice I_h melts to a highly viscous liquid which seemed to be related to an imperfectly relaxed amorphous ice', whereas below $T \sim 130$ K, ice I_h 'transforms to an unrelaxed phase apparently related to HDA' [78]. Mishima [78] notices that the principal halo of the sample recovered after compression at $T = 145$ K is shifted from HDA's principal halo of ∼3.0 Å (figure 2) to ∼2.75 Å. Also the conversion temperature back to LDA, at ambient pressure, is clearly different for samples compressed above and below $T \sim 130$ K (see figure 13, bottom panel). The sharp transition back to LDA as observed by thermal analysis (see figure 13, first peak in top panel) is shifted by approximately +10 K. Therefore, HDA produced at $T = 77$ K is structurally different from the 'HDA' produced between $T \sim 130$ K and $T \sim 165$ K. Nowadays, the structural state of 'HDA' showing the principal halo at ∼2.75 Å is called very high-density amorphous ice (VHDA), and the preparation of VHDA via this route corresponds to PIA. Since amorphous ice of high density cannot be obtained from ice I at $T > 165$ K, and VHDA is produced from ice I at $T \sim 165$ K, VHDA can be viewed as the limiting amorphous structure of highest density.

We note that in computer simulations VHDA has not been obtained by isothermal compression of ice (see e.g. [91, 180]). It is not clear whether this is due to the limitations of the water models used nowadays in simulations, or if this is due to the large compression rates, in comparison with experiments, that are accessible with the present computer times.

3.1.2. Isobaric annealing of HDA.

3.1.2.1. Experimental data. If HDA is obtained by PIA of ice I at $T = 77$ K, and subsequently annealed (i.e. isobaric heating) up to $T \sim 140$ K at pressures between $P = 1.0$ GPa and $P = 1.5$ GPa [78], then the resulting sample shows a similar principal x-ray halo at ∼2.75 Å as observed in VHDA (section 3.1.1). Moreover, if the resulting amorphous ice is recovered at $P = 1$ bar and then heated at constant pressure, it transforms to LDA at a temperature similar to the VHDA → LDA transformation temperature (see figure 13, lower panel). Therefore, both the isothermal compression of ice I at high temperature, and the isobaric annealing of HDA at high pressure, result in VHDA.

The annealing of HDA under pressure up to temperatures close to the crystallization temperature, which corresponds to Mishima's protocol used in [78], has been investigated in more detail at the University of Innsbruck [68, 181]. It is found that HDA densifies on isobaric heating at pressures in the range 0.84 GPa $< P <$ 1.9 GPa. This is quite unusual, since density typically decreases on isobaric heating due to thermal expansion and, therefore, this implies that structural changes take place on isobaric heating. Regardless of the choice of pressure in the range 0.84 GPa $< P <$ 1.9 GPa, the density of the samples, after annealing close to the crystallization temperature and recovering at $T = 77$ K and $P = 1$ bar, is $\rho = 1.25$ g cm^{-3}. The fact that the same structural state at $T = 77$ K and $P = 1$ bar is obtained after annealing HDA at 0.84 GPa $< P <$ 1.9 GPa, and that this structural state is significantly different from HDA, prompted Loerting *et al* [68] to devote the new acronym of VHDA to this state. If VHDA is cooled at constant pressure back to $T = 77$ K (0.84 GPa $< P <$ 1.9 GPa) and

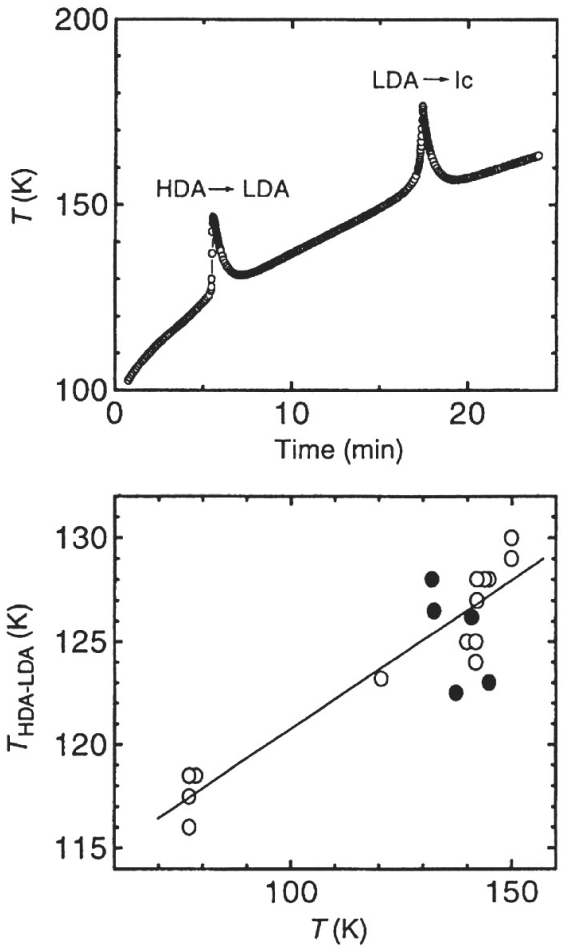

Figure 13. (a) Heating curve of HDA at $P = 1$ bar showing the two relatively sharp transformations corresponding to HDA $\rightarrow$ LDA and LDA $\rightarrow$ ice I_c. Increase in temperature implies an exothermic event. (b) HDA $\rightarrow$ LDA transition temperatures at $P = 1$ bar, $T_{HDA–LDA}$, of recovered HDA ices. Open circles correspond to HDA ices that have been obtained by compression of ice I at temperature T (indicated on the abscissa). Filled circles correspond to HDA ices obtained upon compression of ice I and annealed at $P > 1$ GPa up to the temperature T (indicated on the abscissa). All HDA ices are then recovered at $P = 1$ bar and $T = 77$ K and heated until LDA is formed (from [78]).

heated isobarically up to $T \sim 165$ K again, the expected decrease in density due to thermal expansion is observed [68]; i.e., no further structural changes take place on a 'second' isobaric heating. Recovered VHDA at $T = 77$ K and $P = 1$ bar shows a density that is higher by about 9% than that of HDA and a shift in the Raman peak by $+30$, $+18$, and -15 cm^{-1} for the coupled OH stretching band, the decoupled OD stretching band, and the low-frequency intermolecular band, respectively. In particular, since the decoupled OD frequency correlates with the hydrogen bonded average OO distance, the shift in the OD frequency implies that, when going from HDA to VHDA, the OO distance increases from 2.82 to 2.85 Å. That is, even though VHDA is denser than HDA, its hydrogen bonded OO distances are longer—a paradox explained in terms of a changing of coordination number (see section 4). A similar paradox has also been found for high-pressure crystalline phases [182].

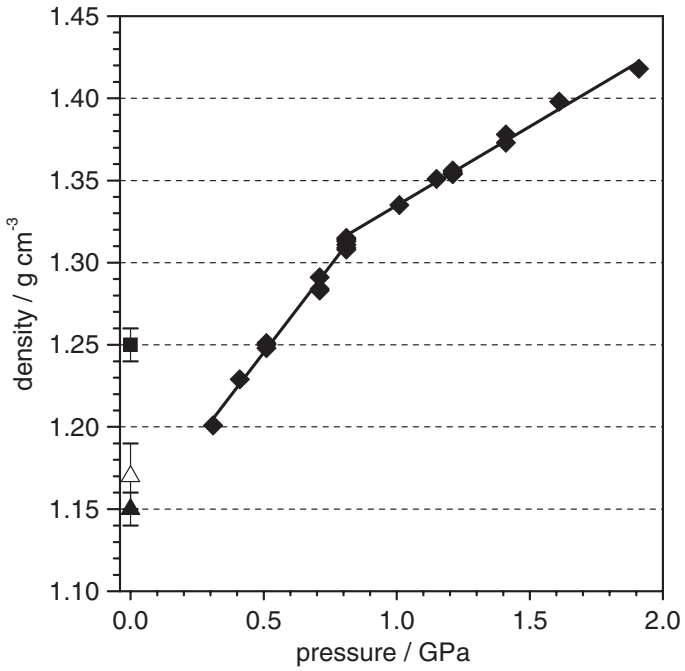

Figure 14. Density values of relaxed amorphous ice calculated from the densities of crystalline high-pressure ices in the pressure range 0.3–1.9 GPa. Linear fits below and above 0.8 GPa (with correlation coefficients of 0.996 for each linear fit) are indicated by thick black lines with gradients of 0.21 g cm^{-3} GPa^{-1} below 0.8 GPa and 0.10 g cm^{-3} GPa^{-1} above 0.8 GPa. Density values of HDA and VHDA at 77 K and 1 bar from [68] are depicted by a full triangle and a full square. Mishima *et al*'s density value of HDA at 77 K and 1 bar is shown by an open triangle [66]. See [181] for further details (from [221]).

In a second set of experiments, the Innsbruck group [181] determined the density of the amorphous ices obtained after annealing HDA at 0.3 GPa $< P <$ 1.9 GPa (i.e. in a wider range of pressures than those discussed above). In these experiments, HDA is first obtained upon compression of ice I_h at $T = 77$ K, recovered at $P = 0$ GPa, and then re-compressed to 0.3 GPa $< P <$ 1.9 GPa. The resulting amorphous ices are then heated isobarically up to $T > T_X$ until crystallization occurs, as indicated by a sharp density change $\Delta\rho$ at $T_X(P)$ (T_X increases from ∼144 K at $P = 0.3$ GPa to ∼183 K at $P = 1.9$ GPa). The density of 'HDA' at T_X can then be calculated as explained in section 2.1, by subtracting $\Delta\rho$ from the densities of crystalline ices at high pressures.

The high-pressure ices produced on crystallizing 'HDA' at 0.3 GPa $< P <$ 1.9 GPa depend on the heating rate employed. In other words, by varying the heating rate at a pressure of, e.g., $P = 0.51$ GPa, one can either produce crystalline ices of a density lower ($\Delta\rho < 0$) or higher ($\Delta\rho > 0$) than that of HDA at $T \sim T_X$. At $P = 0.51$ GPa HDA crystallizes to the less dense ice IX at a heating rate of 0.5 K min^{-1}, and to the more dense ice V at a heating rate of 19 K min^{-1} [183, 184]. However, the densities calculated after heating HDA up to $T \sim T_X$, before crystallization occurs, are independent of the heating rate. Therefore, this method of quantifying HDA densities at $T \sim T_X$ is a valid approach.

The density versus pressure plot of the amorphous samples at $T \sim T_X$ is shown in figure 14. In principle, this $\rho(P)$ curve can be considered as the equation of state of annealed HDA. There are two linear portions in this plot, with a pronounced change in slope at

$P \sim 0.8$ GPa. The slope of the pressure versus density curve at $P > 0.8$ GPa amounts to 0.10 g cm^{-3} GPa^{-1}, and at $P < 0.8$ GPa the slope amounts to approximately twice this value. The value 0.10 g cm^{-3} GPa^{-1} is exactly that of the isothermal compressibility measured upon compression of VHDA [54], and so it suggests that pressurization of the annealed glasses at $P > 0.8$ GPa and $T \sim T_X(P)$ results in merely elastic (reversible) compression of VHDA. On the other hand, the isothermal compressibility of HDA was measured to be 0.14 g cm^{-3} GPa^{-1} [54, 66], and so the slope of ∼0.20 g cm^{-3} GPa^{-1} at $P < 0.8$ GPa implies that pressurization of the annealed glasses at $T \sim T_X(P)$ up to $P \sim 0.8$ GPa results not only in elastic (reversible) compression of HDA but also in an inelastic (irreversible) densification due to structural changes, possibly in such a way that annealed HDA ($P < 0.8$ GPa, $T \sim T_X(P)$) develops toward VHDA ($P > 0.8$ GPa, $T \sim T_X(P)$).

Both x-ray diffractograms and Raman spectra of the annealed samples, after recovering at $P \sim 1$ bar and $T \sim 77$ K, also indicate that major structural changes in the annealed samples occur when the annealing pressure is $P < 0.8$ GPa [181]. This is also consistent with the fact that a pressure $P > 0.8$ GPa is required to produce the limiting VHDA structure upon isobaric annealing of HDA [68]. In the pressure range 0.8 GPa $< P <$ 1.1 GPa only minor structural changes take place among the annealed glasses, and at approximately $P > 1.1$ GPa all the annealed samples have reached the limiting structure VHDA. Therefore, the results shown in figure 14 indicate that the HDA → VHDA transition upon annealing runs to completion only at $P > 0.8$ GPa, while at $P < 0.8$ GPa HDA evolves toward a relaxed HDA. The structural states produced upon annealing HDA close to T_X at $P < 0.8$ GPa are not well investigated experimentally so far, with a notable exception: Nelmes *et al* have shown that both HDA heated isochorically to ∼0.18 GPa and 125 K and VHDA heated isochorically to ∼0.30 GPa and 130 K are characterized by a maximum of the first diffraction peak shifted from the position of unrelaxed HDA in the direction of LDA [185].

It is experimentally hard to distinguish if figure 14 shows a true kink in the density versus pressure plot (attributable to a 'second-order phase transition' between relaxed HDA and VHDA at $T \sim T_X$), or if there is a discontinuity smaller than the experimental reproducibility (attributable to a 'first-order phase transition' between relaxed HDA and VHDA at $T \sim T_X$), or if the slope of $\rho(P)$ decreases without a kink or a discontinuity (attributable to a continuous relaxed HDA → VHDA transition at $T \sim T_X$). Similarly, the density step seen on isothermally compressing HDA at 125 K at 0.8 $< P <$ 1.0 GPa [54] allows for either interpretation: a continuous relaxation or a true phase transition between HDA and VHDA (see section 3.1.3). Therefore, it is still a major open question whether the HDA → VHDA transition takes place continuously over a wide range of pressures, or whether it takes place as a phase transition at a pressure of ∼0.8 GPa (at $T \sim T_X$).

It is natural to ask whether it is necessary to anneal HDA very close to the crystallization temperature T_X, or whether a range of temperatures below the crystallization temperature is available to produce the limiting VHDA. It is found that, indeed, annealing HDA up to temperatures approximately 30–40 K below T_X already results in VHDA. For instance, at $P = 1.17$ GPa, the structural changes causing densification are found to occur between $T \sim 121$ K and $T \sim 130$ K, whereas crystallization takes place at $T \sim 168$ K. That is, the experimental protocol to produce VHDA is to anneal HDA to at least $T \sim 130$ K at a pressure of at least $P \sim 1.0$ GPa. We note that it is necessary to wait for a minute or so at $T > 130$ K and $P > 1.0$ GPa, so that the densification process has ample time to reach completion. Due to the fact that T_X increases by about 20 K GPa^{-1} in the range 1 GPa $< P <$ 2 GPa (see figure 8 in [186] and figure 7 from [114]), the minimum temperature needed to obtain VHDA also increases with pressure. For example, at $P \sim 1$ GPa VHDA can be obtained at $T \sim 130$ K, while at $P \sim 2$ GPa VHDA is formed upon annealing HDA above $T \sim 150$ K.

The preparation of VHDA via this route corresponds to an isobaric, temperature-induced amorphous–amorphous transition (AAT). Such an AAT can be employed not only to prepare VHDA from HDA, but also to prepare HDA from LDA [61, 114]. In figure 8 the two arrows at $T \sim 140$ K and $P \sim 0.35$ GPa and at $T \sim 100$ K and $P \sim 0.5$ GPa indicate this temperature-induced isobaric transition, while the open circles on the LDA $\rightarrow$ HDA boundary indicate isothermal, pressure-induced transitions.

3.1.2.2. Isobaric annealing of amorphous ices in computer simulations. The experimental densities of HDA at $P = 1.41$ GPa and $P = 1.61$ GPa are $\rho \sim 1.35$ and 1.38 g cm^{-3}, respectively (data extrapolated from figure 2 of [78]). After annealing up to $T \sim 165$ K, the corresponding densities of VHDA are estimated to be $\rho \sim 1.37$ g cm^{-3} and $\rho \sim 1.40$ g cm^{-3}, respectively [181]. MD simulations using the TIP4P [91] and SPC/E [187] models are able to reproduce the HDA $\rightarrow$ VHDA transformation upon annealing HDA. In references [91, 187], HDA is heated isobarically at high pressure, following the corresponding experimental recipe to produce VHDA. The densities of HDA and VHDA, in both models, compare qualitatively well with the experiments. For example, simulations using the TIP4P model show that at $P = 1.65$ GPa, the densities of HDA ($T = 80$ K) and VHDA ($T = 170$ K) are $\rho \sim 1.38$ g cm^{-3} and $\rho \sim 1.42$ g cm^{-3}, respectively [91]. Results using the SPC/E model are shown in figure 15. HDA is formed after compression of LDA at $T = 77$ K. At $P \sim 1.38$ GPa, the density of HDA is $\rho \sim 1.31$ g cm^{-3} (red square symbol in figure 15(a)). After annealing HDA at $P = 1.38$ GPa up to $T \sim 170$ K $< T_g \sim 180$ K (horizontal arrow in figure 15(a)), VHDA is formed with a density of $\rho \sim 1.35$ g cm^{-3} (see figure 15(b)).

In computer simulations, as in experiments, the differences between HDA and VHDA are more evident after recovering at $P = 0$ GPa and $T = 77$ K (see the dotted green and dashed blue lines in figure 15(a)). For example, for the SPC/E model, the densities of HDA and VHDA at $P = 0$ GPa and $T = 77$ K are $\rho = 1.2$ g cm^{-3} and $\rho = 1.26$ g cm^{-3}, respectively. These values are similar to the experimental values of $\rho = 1.15$–1.19 g cm^{-3} for HDA and $\rho = 1.25$ g cm^{-3} for VHDA. However, simulations show that the densities of recovered HDA and VHDA depend on the annealing pressure (section 3.2.1).

The effect of annealing amorphous ices at high, intermediate, and low pressures has been studied in detail in a few recent simulations [91, 118, 180, 187].

References [91, 180] focus on the effect of annealing HDA and *decompressed* samples of HDA at $T = 80$ K using the TIP4P model. In this case, HDA is first obtained upon isothermal compression of ice I_h at $T = 80$ K *up to* $P = 2.25$ GPa (up triangles in figure 16(a)). Then, HDA configurations *obtained at* $P = 1.5$ GPa are isothermally decompressed to different pressures down to $P = 0$ GPa (down triangles in figure 16(a)). Horizontal arrows in figure 16(a) show the effect of annealing these glasses from $T = 80$ K up to $T = 170$ K *and* after cooling down the system back to $T = 80$ K. At high pressures, $P > 1.25$ GPa, the HDA $\rightarrow$ VHDA transformation, as described in the previous paragraphs, is observed. The effect of annealing isothermally decompressed HDA at approximately 0.7 GPa $< P < 1$ GPa is to increase the density, as is the case in the HDA $\rightarrow$ VHDA transformation at $P > 1.25$ GPa. As the annealing pressure approaches the value $P = 0.7$ GPa, the total increase of density after annealing decreases (figure 16(a)). Moreover, at $0 < P < 0.7$ GPa, annealing produces a less dense amorphous ice. The formation of less dense glasses upon annealing at low pressures already has experimental support: in fact, the annealing of recovered HDA at $P = 0$ GPa is nothing else but the 'recovered HDA' $\rightarrow$ LDA transformation discussed in section 2.

References [118, 187] focus on the effect of annealing LDA, HDA, and glasses formed upon compression of LDA, during the LDA $\rightarrow$ HDA transformation (at approximately $P < 1$ GPa, i.e. before HDA is fully formed) using the SPC/E model (see solid line in

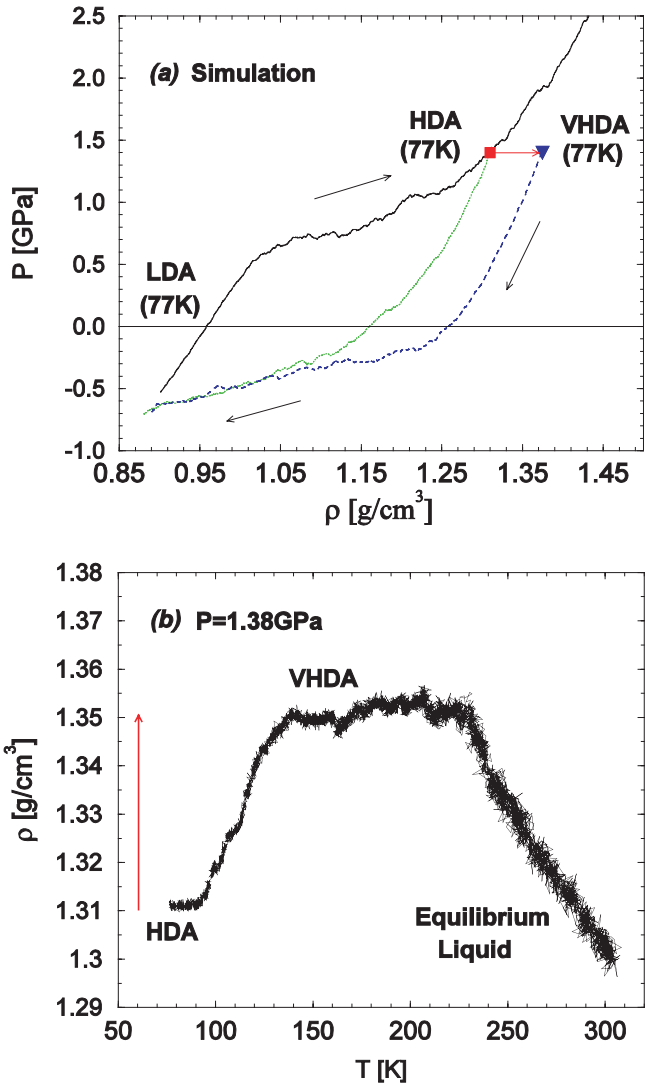

Figure 15. (a) Compression curve during the LDA → HDA transformation at $T = 77$ K obtained from MD simulation using the SPC/E model (black horizontal line). The solid arrow indicates the evolution of density upon heating HDA (square) from $T = 77$ K up to $T \sim 165$ K and cooling back to $T = 77$ K, at $P = 1.38$ GPa. The resulting amorphous ice is identified as VHDA (down triangle). The dotted (green) and dashed (blue) lines are the decompression curves of HDA and VHDA at $T = 77$ K, respectively. (b) Evolution of density with temperature during the HDA → VHDA transformation indicated in (a), (from [118]).

figure 16(b)). Horizontal arrows in figure 16(b) show the effect of annealing the starting glasses from $T = 77$ K up to $T \sim 170$ K. Upon annealing at $P > 0.15$ GPa, the amorphous ices become denser. The transformation resembles the HDA → VHDA transformation. Thus, in computer simulations, annealing HDA at high pressure ($P > 1$ GPa) has the same effect as annealing LDA/HDA at intermediate pressures (approximately 0.15 GPa $< P <$ 1 GPa): upon annealing, the density of the system increases. In these computer simulations [118, 187], the phenomenology observed at high pressure is not particular to the HDA → VHDA

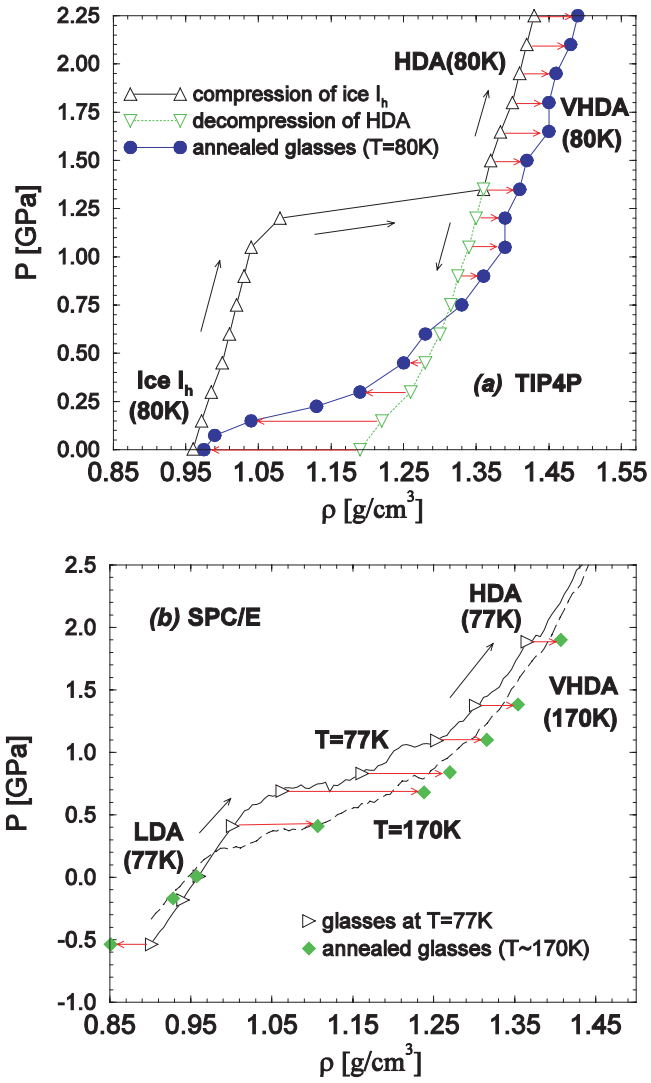

Figure 16. (a) Compression of ice I_h at $T = 80$ K from MD simulations using the TIP4P model (black line, up triangles). The sharp change in density at $\rho \sim 1.3$ g cm^{-3} corresponds to the amorphization of ice I_h to HDA. The dotted green line (down triangles) is the decompression of HDA ($\rho = 1.35$ g cm^{-3}) at $T = 80$ K. Both the decompressed ($\rho < 1.35$ g cm^{-3}) and compressed ($\rho > 1.35$ g cm^{-3}) HDAs are annealed (isobarically heated) up to $T \sim 170$ K *and cooled back to* $T = 80$ K (horizontal arrows). The resulting amorphous ices are indicated by the blue solid line (filled circles), and correspond to VHDA states at high pressure (adapted from [91]). (b) Compression of LDA at $T = 77$ K (black line, right triangles) and $T = 170$ K (long-dashed black line) from MD simulations using the SPC/E model. The compression of LDA results in HDA at high pressure. Horizontal arrows indicate the density change upon annealing *up to* $T \sim 170$ K the amorphous ices obtained at $T = 77$ K. These annealed glasses at high pressure are identified as VHDA (adapted from [118]).

transformation, but it is also observed upon annealing *LDA and glasses corresponding to a mixture of LDA and HDA,* at intermediate pressures (approximately 0.3 GPa $< P <$ 1 GPa). The total increase in density after annealing, $\Delta\rho$, is maximal at $P \sim 0.7$ GPa ($\Delta\rho \sim 0.18$ g cm^{-3}; figure 16(b)) [118]. As the annealing pressure increases above this

value, $\Delta\rho$ becomes smaller (e.g., $\Delta\rho \sim 0.02$ g cm^{-3} at $P = 2.66$ GPa). Similarly, if the pressure decreases below $P \sim 0.7$ GPa toward $P \sim 0.15$ GPa, $\Delta\rho$ becomes smaller; and $\Delta\rho \sim 0$ at $P \sim 0.15$ GPa. For lower pressures, the amorphous forms corresponding to LDA, expand. For example, it is found that at $P = 0.01$ GPa $\Delta\rho \sim -0.005$ g cm^{-3}. At even lower pressures, below $P = 0$ GPa, the expansion upon annealing becomes larger, and at low enough temperature the density decreases monotonically upon annealing; in this case, the system sublimates before $T \sim 170$ K (see figure 16(b)).

The apparently complicated behaviour of amorphous ice upon annealing at different pressures can be understood *in computer simulations*, at least qualitatively, by taking into account the low-T equilibrium isotherms in the P–ρ plane. Figure 17(a) shows, for the SPC/E model, the $T = 77$ K glass isotherm during the LDA $\rightarrow$ HDA transformation in the P–ρ plane (thick black line), together with the $T = 210$ K and $T = 230$ K equilibrium liquid isotherms (circle and diamond symbols, respectively). We also show two trajectories corresponding to the isothermal decompression of HDA (black dotted line) and VHDA (blue dashed line) at $T = 77$ K. There is one simple rule that explains qualitatively the results of references [91, 118, 180, 187] upon annealing: 'the state point in the P–ρ plane evolves, upon heating, toward the low-T equilibrium isotherm'. By 'low-T equilibrium isotherm', we mean the lowest temperature at which the system can be equilibrated (liquid or vapour phase) in simulations (where crystallization does not occur). In experiments, such a 'low-T equilibrium isotherm' cannot be reached due to crystallization. In this case, the 'low-T equilibrium isotherm' could probably be replaced by the glass transition temperature line, $T_g(P)$. Figure 17(a) shows a few trajectories upon annealing the amorphous ices from $T = 77$ K [118]. Left-pointing (red) arrows are the trajectories starting at glass state points that, at $T = 77$ K, have a density higher than that of the low-temperature liquid. These glasses expand upon annealing. Green (right-pointing) arrows are the trajectories starting at glass state points that, at $T = 77$ K, have a density lower than that of the low-temperature liquid. These glasses contract upon annealing.

Figure 17(b) shows, for the TIP4P model, the compression curve of ice I_h (solid black line) and the decompression curve of HDA (dotted black line), together with the location of the annealed glasses shown in figure 16(a) (solid grey (cyan) line). We include in the figure the low-temperature ($T = 200$ K) liquid isotherms from [117] (square symbols). The red (left-pointing) and green (right-pointing) arrows indicate the trajectories in the P–ρ plane of the glasses that contract or expand upon annealing, respectively [91, 180]. Although the liquid isotherm in figure 17(b) extends only up to $\rho \sim 1.2$ g cm^{-3}, the results for the TIP4P model are consistent with the view that upon annealing the glass state points move, in the P–ρ plane, toward the low-T liquid isotherm.

Figures 17(a) and (b) also indicate that at negative pressure and above $P \sim -0.25$ GPa the liquid isotherms are located at lower densities than those for LDA and recovered HDA. Thus, these glasses expand upon annealing. Moreover, the SPC/E model simulations show that there is no liquid isotherm at approximately $P < -0.25$ GPa. At these pressures, the amorphous ice sublimates upon annealing. In this case, the 'low-temperature liquid isotherm', toward which the glass state point moves, should be identified with a low-temperature vapour isotherm.

3.1.3. Slow compression of LDA at $T = 125$ K: LDA $\rightarrow$ HDA $\rightarrow$ VHDA transformation. HDA can be prepared both by annealing [114] and by isothermal compression of LDA [61, 117]. In the previous section, we discuss how VHDA can be formed upon isobaric annealing of HDA. Thus, it is natural to ask whether VHDA can be obtained upon isothermal compression of HDA. That this is, indeed, possible was recently presented by means of analysis of recovered samples by x-ray diffraction after isothermal compression of amorphous ice [54].

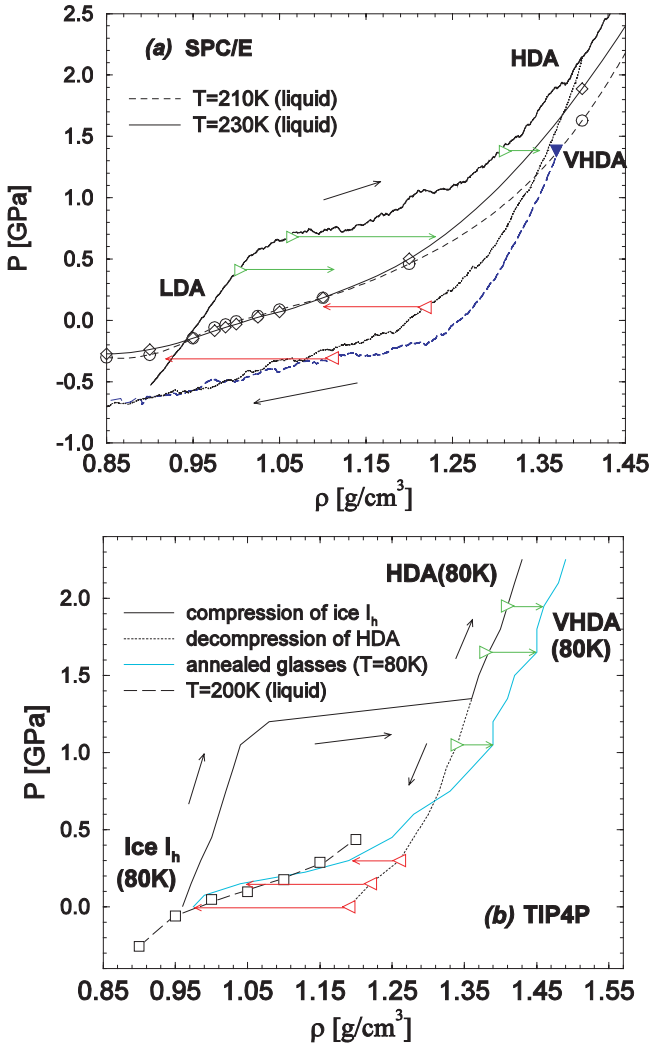

Figure 17. Effect of annealing amorphous ices in computer simulations. Upon annealing, glasses evolve in the P–T plane, toward the low-temperature equilibrium isotherms. (a) Compression curve during the LDA $\rightarrow$ HDA transformation at $T = 77$ K using the SPC/E model (from figure 16(b)). The solid thin line (diamonds) and dashed thin line (circles) are two low-temperature equilibrium liquid isotherms. Dotted thick and long-dashed thick lines are decompression curves of HDA and VHDA at $T = 77$ K, respectively (liquid isotherms from [222]). (b) Compression curve of ice I_h (solid black line), decompression curve of HDA (dotted black line), and annealed glasses (solid grey (cyan) line) from MD simulation using the TIP4P model (from figure 16(a)). The long-dashed line is a low-temperature isotherm (liquid isotherms from [138]). From (a) and (b), glasses at a given pressure, with higher density than that of the equilibrium liquid, contract upon annealing (right-pointing (green) arrows), while glasses with lower density than that of the equilibrium liquid expand upon annealing (left-pointing (red) arrows).

On compressing LDA slowly (with a compression rate of 20 MPa min^{-1}) at $T = 125$ K, two relatively sharp transitions are observable (see figure 18). At $P \sim 0.45$ GPa, a density increase from $\rho = 0.94$ g cm^{-3} to $\rho = 1.13$ g cm^{-3} (i.e. by about 20%) is observed. This first step in density corresponds to the LDA $\rightarrow$ HDA transformation discussed in section 2.3.1. At

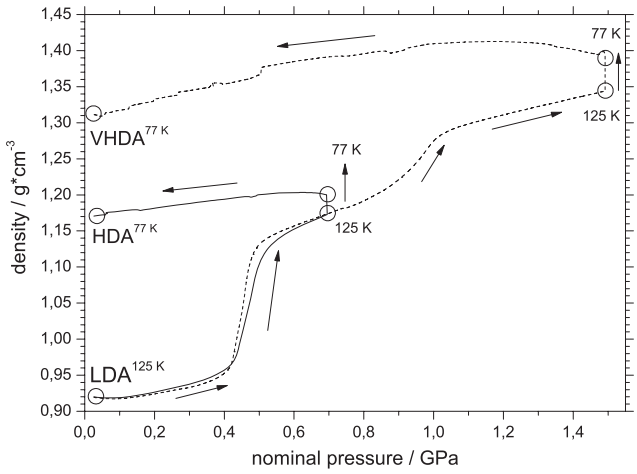

Figure 18. Pressure–density curves for isothermal compression of LDA at a rate of 20 MPa min^{-1} at 125 K, subsequent quenching to 77 K and decompression at 20 MPa min^{-1}. For calculation of density and further experimental details see [54] (from [221]).

$P \sim 0.95$ GPa, a second increase in density from 1.22 to 1.28 g cm^{-3} (by about 5%) can be observed. This second step in density represents a transformation from HDA to VHDA. The isothermal compressibility κ_T (see figure 3, bottom panel in [54]) shows two maxima and reaches at least five times the isothermal compressibilities κ_T of LDA and HDA in the course of the transformation. Assuming that the density serves as an order parameter for the transformation, such a maximum in the response function κ_T is usually seen as an indication of a phase transition [188].

When Mishima investigated systematically the amorphization/melting of ice as a function of temperature, he also prepared VHDA by isothermal compression at $T = 145$ K (see the caption of figure 4 in Mishima [78]; see section 3.1.1), but did not distinguish VHDA from HDA even though he observed a significant shift in the x-ray halo peak. He reasoned that the viscous liquids/relaxed amorphous states prepared isothermally between $T = 140$ K and $T = 160$ K, as well as the unrelaxed HDA states prepared isothermally at $T < 140$ K, all lie within the same HDA megabasin in configuration space. In view of the recent results presented in [54], it becomes increasingly clear that the relation between LDA and HDA is very similar to the relation between HDA and VHDA: the preparation routes of HDA from LDA are very similar to the preparation routes of VHDA from HDA. Moreover, the P–ρ curve of amorphous ice indicates that HDA and VHDA may indeed be two distinct amorphous phases [181], and that both LDA and HDA, *and* HDA and VHDA, are separated, on isothermal compression, by a relatively sharp density step and isothermal compressibility maximum [54].

However, as already mentioned in section 3.1.2.1, whether HDA and VHDA are two distinct amorphous states [54] or whether they correspond to the same state [78] is still an open question. The two density steps of figure 18 could be either a result of an unusual accelerating/decelerating kinetics or of thermodynamic origin. A major difference between these two density steps is that the step between LDA and HDA does not smear out up to compression rates of 6000 MPa min^{-1}, whereas the step between HDA and VHDA smears out at compression rates $\geqslant 600$ MPa min^{-1}. Loerting *et al* have attributed this difference to a lower activation barrier between LDA and HDA at $P \sim 0.45$ GPa than between HDA and VHDA at $P \sim 0.95$ GPa [54].

We note that the LDA → HDA transformation upon isothermal compressions has not been observed, so far, in computer simulations. It is not clear whether this is due to limitations of the water models or to the fast compression rates used in simulations with respect to experiments.

3.2. Phase diagram of glassy water

3.2.1. How many 'families' of amorphous ices exist at $P = 0$ GPa? In experiments, the densities of LDA (obtained upon isobaric heating of recovered HDA at $P = 1$ atm) [61], recovered HDA (obtained either upon compression of LDA or ice I) [61], and recovered VHDA (obtained upon decompression of VHDA either from $P = 1.1$ GPa or $P = 1.9$ GPa) [68] at $T = 77$ K and $P = 1$ bar are $\rho = 0.94 \pm 0.02$ g cm^{-3}, $\rho = 1.17 \pm 0.02$ g cm^{-3}, and 1.25 ± 0.01 g cm^{-3}, respectively. Thus, apparently each amorphous ice can be characterized by a single density value at $P = 1$ bar and $T = 77$ K. Both in the original experiments by Mishima *et al* [66] as well as in recent experiments [87, 88], recovered HDA has been heated isobarically at $P = 1$ bar, from $T = 77$ K to different intermediate temperatures $T < 120$ K, before LDA forms. In these experiments, many amorphous forms with *structure factors intermediate* between those of LDA and recovered HDA are obtained at $P = 1$ bar, which suggests that these samples are different from LDA, HDA, or any mixture of LDA and HDA [87, 88]. Furthermore, this also suggests that the densities of these intermediate states are in between the LDA and HDA densities given above. However, there is no direct information on the densities. Inspection of figure 3 in [87] shows that the first sharp x-ray diffraction peak of HDA shifts by about 25% towards LDA after three annealing cycles at 95, 100, and 105 K, and shifts by the remaining 75% to LDA after the fourth annealing cycle at 110 K. This behaviour seems compatible with the findings presented in figure 3, which shows a gradual decrease of the HDA density on heating from 77 K and a sudden density decrease at higher temperatures attributed to the HDA → LDA transition. It therefore seems likely that there is a range of HDA densities, i.e. there is a family of HDA states, and a sharp transition between HDA and LDA. Also, Nelmes *et al* have shown recently using *in situ* isochoric experiments in the Paris–Edinburgh cell that there is a range of HDA structure factors in between 'unrelaxed' (u-HDA) and 'expanded' (e-HDA) states [185]. However, whereas e-HDA has been prepared in the field of stability HDA and probably represents the metastable equilibrium configuration of HDA at $P = 0.18$ GPa, u-HDA and all states of HDA at ambient pressure represent kinetically arrested, unstable configurations, since it is the field of stability of LDA at 1 bar. Whereas e-HDA shows a first-order-like phase transition to LDA upon heating at 1 bar, u-HDA shows a transition to LDA which can be interpreted as continuous, since the annealing of u-HDA is superimposed on the first-order-like phase transition. Similar to VHDA, e-HDA also shows a sharp transition to LDA at clearly higher temperatures than the broad transition of u-HDA to LDA at 1 bar.

More experimental work is needed to answer the question of whether homogeneous amorphous states of *any* density in the range $\rho \sim 0.94$–1.32 g cm^{-3} can be prepared experimentally or if there are density gaps for which no homogeneous amorphous state can be obtained at 77 K and 1 bar, e.g., from $\rho \sim 0.98$–1.12 g cm^{-3} and from $\rho \sim 1.19$–1.22 g cm^{-3}. Currently there are no experimental density data available disproving that there is a density gap between LDA and HDA as well as between HDA and VHDA.

Both the TIP4P and SPC/E simulations suggest that LDA, HDA, and VHDA cannot be characterized by a unique density at $P = 1$ bar, and suggest the view that amorphous ices should each be considered as a family of slightly different states. Moreover, simulations indicate that, by following different thermodynamic paths, it is possible to obtain amorphous ices with densities in a continuous range of values that depends on pressure; at $P = 0$ GPa, such a density range is $\rho \sim 0.94$–1.32 g cm^{-3}. As discussed in [180], considering HDA and

LDA as two families of amorphous ices can explain the continuum of amorphous ices found in the experiments of reference [87] at $P = 0$ GPa.

The SPC/E simulations [118] show that recovering (i.e. isothermal decompression at $T = 77$ K) HDA and VHDA, from approximately $P > 1.35$ GPa down to $P = 0$ GPa, results in amorphous ices with densities in narrow intervals of $\rho \sim 1.15$–1.24 g cm^{-3} and $\rho \sim 1.22$–1.28 g cm^{-3}, respectively. This suggests that HDA is a *large* family of different amorphous forms (similarly, VHDA is a *small* family of different amorphous forms). Moreover, these two density intervals overlap, meaning that recovered HDA and VHDA are indistinguishable at $P = 0$ GPa. If HDA and VHDA are recovered at negative pressure, $P \sim -0.4$ GPa, then the HDA and VHDA samples collapse to a single state at $\rho = 1.05$ g cm^{-3}.

TIP4P simulations [91, 180] show that recovering VHDA and samples annealed at $P > 1$ GPa results in amorphous ices at $P = 0$ GPa with densities in a narrow interval of 1.28–1.32 g cm^{-3}. It is also found that recovering samples annealed at intermediate pressures (0.225 GPa $< P < 1$ GPa) results in a broad continuum of metastable HDA states at $P = 0$ GPa, with densities 1.10 g cm^{-3} $< \rho <$ 1.26 g cm^{-3}. Recovering at $P = 0$ GPa the amorphous ices annealed at $0 < P < 0.225$ GPa (corresponding to LDA) [91, 180] results in a family of slightly different glasses with densities in the range 0.97–1.025 g cm^{-3} (see also section 2.3.3).

3.2.2. What is VHDA?

3.2.2.1. Is VHDA an annealed HDA? The MD simulations, based on the TIP4P [91, 180] and the SPC/E [118, 187] models described so far indicate that the LDA $\rightarrow$ HDA transformation may be interpreted as a relaxation effect due to annealing. In this view, VHDA is identified as 'relaxed HDA'. Therefore, these computer simulations support Mishima's interpretation that HDA and VHDA both correspond to states in the same megabasin of the configuration space [78]. The results *from these computer simulations* supporting this view are the following. (i) The densification upon annealing HDA at high pressure (to obtain VHDA) is also observed at intermediate pressures, upon annealing LDA and other glasses obtained in the transition region of LDA and HDA (i.e. glasses corresponding to HDA samples 'contaminated' with LDA). (ii) The HDA $\rightarrow$ VHDA transformation is accompanied by a continuous evolution of the hydrogen bond network topology. As revealed by the network ring statistics, HDA represents a gradual evolution of LDA into VHDA [91] (see section 4). (iii) The higher the compression temperature in the isothermal LDA $\rightarrow$ HDA transformation, the larger the density of HDA at a given pressure. The density of HDA at a given pressure approaches, as the compression temperature increases, the value corresponding to VHDA at the given pressure [118].

Two other results agree with the view of VHDA as 'relaxed HDA' (however, they do not exclude the view of VHDA as a different glassy state than HDA). (i′) VHDA can be cycled at a constant (high) pressure (e.g. at $P > 1.38$ GPa; see figure 2 in [92, 187]) from $T \sim 165$ K down to $T = 77$ K, and back to $T \sim 165$ K. No HDA is formed in the cycle and the sample before and after the cycle has the same structural and thermodynamic properties [187] (this result is in agreement with experiments [68]). This irreversibility in the HDA $\rightarrow$ VHDA transformation is reminiscent of the relaxation of hyperquenched glasses to standard glasses upon annealing observed in experiments and simulations [189, 190]. However, this result does not exclude the possibility that HDA and VHDA are different glass states. For example, LDA and HDA are commonly accepted as two different glassy states. If LDA is obtained upon annealing HDA at $P \sim 0.1$ GPa, then LDA can be cycled from 140 to 77 K and 140 K and it remains LDA. (ii′) In simulations, VHDA does not convert back to HDA upon *isochoric* heating. We note that such a transformation of VHDA back to a HDA-like state is suggested both by the experiments of

reference [68] (figure 1(d) in that work) and by the experiments of reference [185] (figure 2 in that work) (see section 3.2.2.3).

The scenario of VHDA as a 'relaxed HDA' implies that the liquid–liquid first-order transition hypothesis is still consistent with experiments. The two amorphous states at low temperature separated by the first-order transition line should be identified as LDA and VHDA, rather than LDA and HDA. Experimental support for this scenario was provided by Mishima and Suzuki [191]. They were able to show that a sample of VHDA heated to 115.4 K at $P = 1$ bar shows a phase boundary to LDA that propagates on the sample on continued heating [191]. This corresponds to the expectation for a first-order transition without the interference of a continuous annealing process. This is also evident from a relatively sharp frequency shift of the Raman peak (of the uncoupled OH stretching mode), and its intensity monitored on heating VHDA (see figure 2 in [191]). By comparison, heating HDA at $P = 1$ bar (before annealing at high pressure; i.e. u-HDA in [185]) shows a much broader and much more continuous frequency shift of the same Raman peak (see figure 2 in [182]). Also, small-angle neutron scattering studies (at low-pressure conditions) indicate that HDA is a heterogeneous structure on the length scale of a few nanometres, whereas LDA and VHDA are homogeneous structures on this length scale, which might point in the direction of VHDA as relaxed HDA [90].

3.2.2.2. Is VHDA a new amorphous ice? Since there are at least 15 crystalline polymorphs of ice [1], it is natural to ask why there should be only two amorphous ices. There are few experimental results supporting the view of VHDA as a third amorphous ice. Most notable among these are (i) the density gap between HDA and VHDA at 77 K and 1 bar (see section 3.2.1), (ii) the differences in the diffractograms and the gap in Raman peak frequencies of HDA and VHDA decompressed down to $P = 1$ bar (*with no annealing at* $P = 1$ *bar*) [68], and (iii) the density jump observed at $P \sim 0.95$ GPa on compressing HDA at $T = 125$ K (section 3.1.3) [54].

As originally proposed from experiments [68], some computer simulations [192–195] also support the idea that VHDA is a new amorphous ice, different from LDA and HDA. The computer simulation results discussed so far are based on MD simulations. Moreover, with the exception of [92], the long-range Coulombic interactions (LRCIs) in those works are treated using the reaction field or Ewald sum techniques [196]. Recently, Brovchenko *et al* [192, 193] performed Monte Carlo (MC) simulations in both the Gibbs ensemble [197] and in the density-fluctuation-restricted NPT ensemble [198, 199]. They used the ST2, TIP5P, TIP4P, and SPC/E water models *as originally parameterized*. Therefore, the LRCIs were not included for molecules separated by distances larger than ∼0.9 nm. They also performed MC simulations, using the ST2 model treating the LRCI with the reaction field technique, and reproduced the results from MD simulations of reference [60]. We note that these 'ST2 models' (one treating the LRCI with reaction field and the other neglecting the LRCI) are, strictly speaking, different water models. Brovchenko *et al* [192, 193] find that the effect of adding the LRCI has drastic effects in the phase diagram of all the water models studied. In particular, they find that all these models show multiple amorphous–amorphous (i.e., liquid–liquid or glass–glass) transitions when no LRCI are included: two such transitions for the TIP5P, TIP4P, and SPC/E models, and three transitions for the ST2 model. Figure 19(a) shows the isotherms for the ST2 model with no LRCI obtained by MC simulations in the density-fluctuation-restricted NPT ensemble (data at $T \geqslant 260$ K are also confirmed by MC simulations in the Gibbs ensemble). As T decreases below $T = 290$ K, liquid–liquid transitions develop and, at $T = 235$ K, three such transitions are observed (see arrows). Figure 19(b) shows schematically the resulting T–ρ phase diagram. The three CPs, corresponding to the end of the liquid–liquid transition lines,

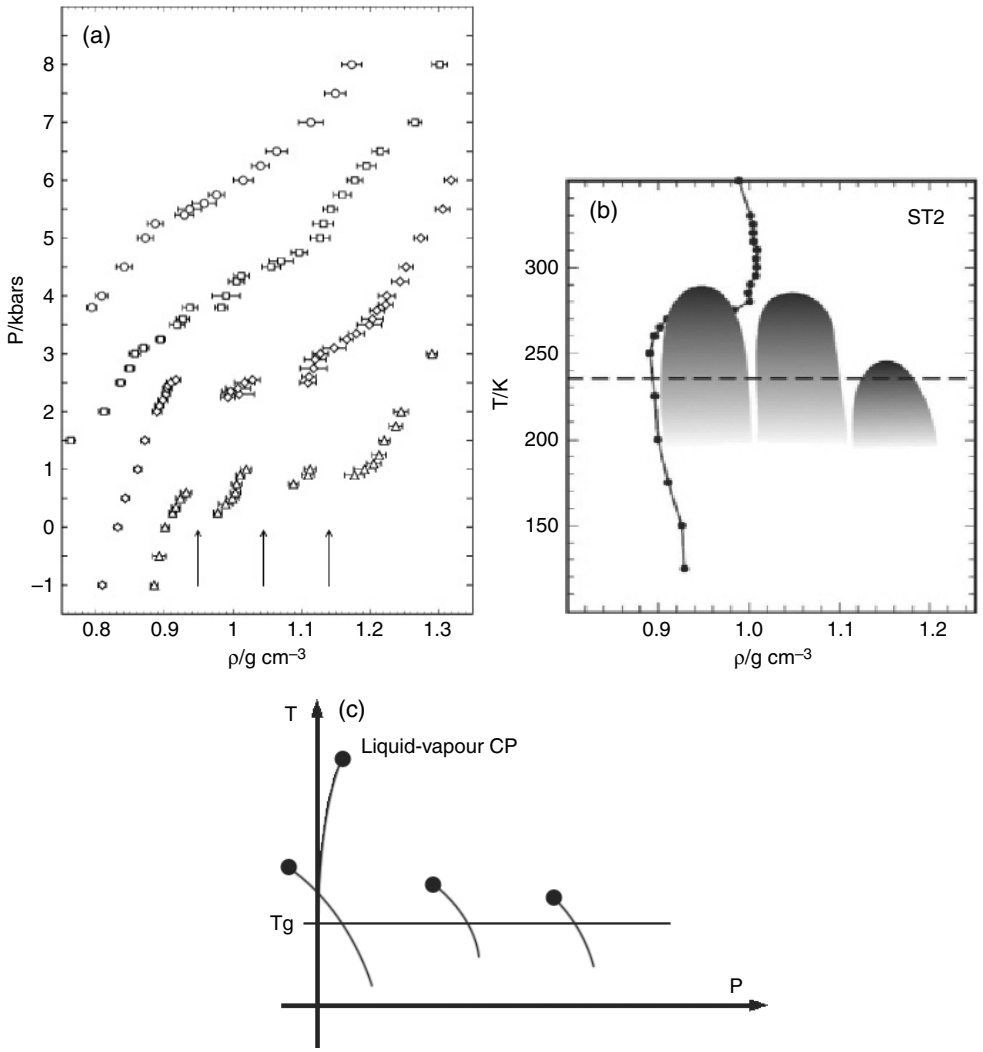

Figure 19. (a) Isotherms obtained from NPT density-fluctuation-restricted Monte Carlo simulations using the ST2 model with no long-range Coulombic interactions (i.e. as originally parameterized). Temperatures are $T = 290$ K (circles), $T = 275$ K (squares), $T = 260$ K (diamonds), and $T = 235$ K (triangles). Pressures are shifted by 2, 4, and 6 kbar for the 260 K, 275 K, and $T = 290$ K isotherms, respectively. Three isotherms are observed at $T = 235$ K (arrows). (b) Schematic representation of the liquid–liquid transitions (shaded areas) observed in (a). The solid line is the liquid–vapour coexistence line, which corresponds to the $P \sim 0$ GPa isobar. The dashed line is the estimated glass transition temperature. (c) Schematic T–P phase diagram corresponding to (b) (parts (a) and (b) are from [192]).

are located above the glass transition temperature T_g (see the dashed line)[5]. The liquid–vapour coexistence line in figure 19(b), which corresponds to the $P \sim 0$ GPa isobar, goes in between the low-density and intermediate-density CPs. Therefore, for the ST2 model, only the two high-

[5] As stated in [193], the isotherms of figure 19(a) do not exclude the possibility that the two liquid–liquid transitions lines at high density end up in a common CP. If so, the narrow region around $\rho = 1.1$ g cm^{-3} in figure 19(b) should end up in a triple point where three liquid phases coexist.

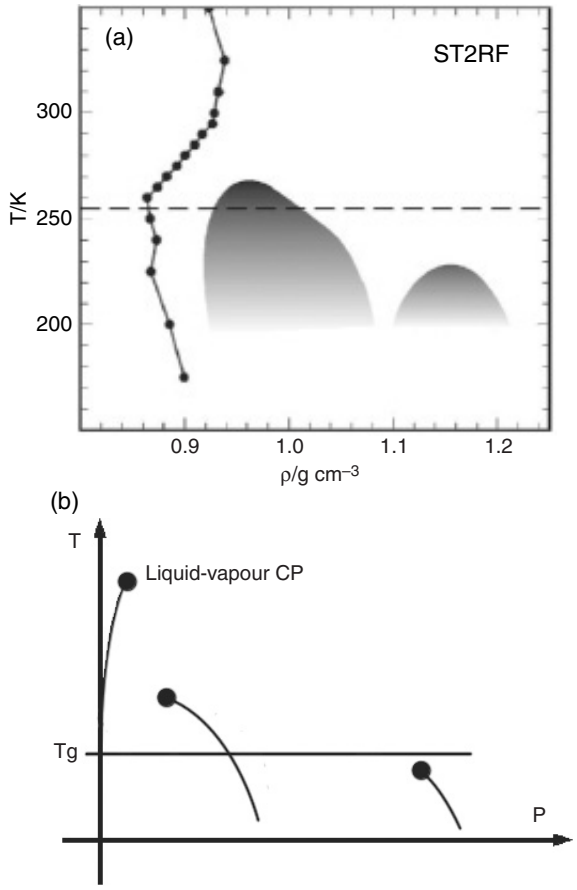

Figure 20. The same as figures 19(b) and (c) for the ST2 model treating the long-range Coulombic interactions using the reaction field technique (part (a) is from [193]).

density CPs are located at positive pressure (see figure 19(c)). The low-density CP is located at negative pressures and its corresponding first-order liquid–liquid transition line crosses the liquid–vapour coexistence line (see figure 19(c)). This also implies that there is a triple point where the two low-density liquids coexist with the vapour phase. A liquid–liquid transition line ending in a CP located at negative pressures was proposed in [136, 137] based on MD of the TIP4P model (with no LRCI).

Figure 20(a) shows the phase diagrams for the ST2 models from [193] when the reaction field technique is used to treat the LRCI. Only two CPs are observed in this case (in addition to the liquid–vapour CP). The low-density CP corresponds to the liquid–liquid CP of [60] (see figure 11). The extra CP at $\rho \sim 1.15$ g cm^{-3} is not detected in the MD simulations of [60]. Both CPs in figure 20 are located at $P > 0$ GPa but only one of them is in the liquid phase. The high-density CP is located at $T < T_g$ and thus it is in the glassy state. The phase diagrams from [193] for the TIP5P, TIP4P, and SPC/E models are shown in figure 21. The TIP4P model shows two CPs in the liquid phase, one at positive and another at negative pressures. The TIP5P model shows two CPs at positive pressures, one in the liquid and the other in the glass states. Finally, the SPC/E model shows two CPs in the glass state, one at positive and another at negative pressures.

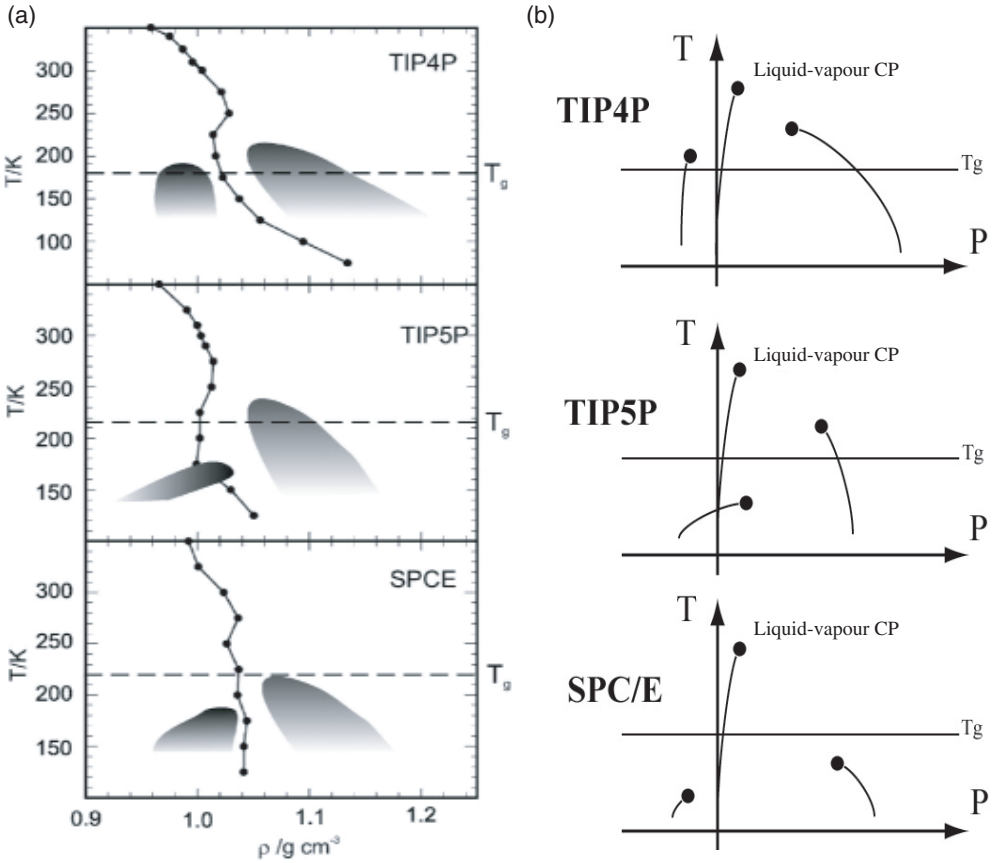

Figure 21. The same as figures 19(b) and (c) for the TIP4P, TIP5P, and SPC/E models. The long-range Coulombic interactions are not included (i.e., the models are defined as originally parameterized) (T–ρ plots are from [193]).

A comparison of the phase diagrams of figures 19–21 for the different water models indicates that only the ST2 potential (with or without LRCI) is consistent with the view of VHDA as a new glass state, different from LDA and HDA. In other words, only the ST2 potential (with or without LRCI) phase diagram has (i) a liquid–liquid first-order transition line located at *positive pressures (for at least some range of T)*, which also has *negative slope* in the P–T plane, and (ii) this liquid–liquid transition line is accompanied by *at least* another liquid–liquid or glass–glass first-order transition line at *higher* pressures.

A recent MC simulation [194] in the Gibbs ensemble using a *polarizable* water model also shows the presence of two liquid–liquid transitions. These transition lines end in two CPs located at $P > 0$: the temperature of the low-density CP being lower than that of the high-density CP. As found for the ST2 model, this model also has a triple point where the two low-density liquids coexist with the vapour phase. The only MD simulation showing multiple liquid–liquid phase transitions was performed using a spherical potential interaction [195]. In [195], it is shown that an isotropic potential with three length scales is able to show three CPs, one corresponding to the liquid–vapour transition, and two corresponding to liquid–liquid transitions.

3.2.2.3. Can HDA be obtained from VHDA? A key question that needs to be answered in order to distinguish between the scenarios outlined in sections 3.2.2.1 and 3.2.2.2 is whether HDA can be produced directly from VHDA. It was shown in a few studies that decompressed VHDA at $P = 1$ bar annealed up to $T \sim 136$ K results [200] in LDA, i.e. VHDA does not transform back to HDA but rather transforms to LDA (see figure 13(b) taken from [78]; figure 3(g) in [68]; figures 2 and 3 in [191]). Because of the apparently missing reversibility of the HDA $\rightarrow$ VHDA transformation, it was assumed that VHDA is in fact in the same megabasin in configurational space as HDA, thus supporting the view of VHDA as relaxed HDA. However, on heating VHDA at *constant volume*, from $T = 77$ K (with an initial pressure of $P = 0.02$ GPa) up to $T \sim 140$ K, a state similar in density and structure to HDA can be regained after recovery (figure 1(d) in [68]). Nelmes *et al* also show that VHDA heated isochorically from $T \sim 85$ K and $P \sim 0.2$ GPa to $T \sim 130$ K and $P \sim 0.5$ GPa transforms back to a state similar to e-HDA, and it can be cycled repeatedly between e-HDA and VHDA [185]. Furthermore, an amorphous structure indiscernible from HDA from neutron scattering experiments was found prior to formation of LDA on isobaric heating at 1 bar [90]. However, these are just scattered hints that the VHDA $\rightarrow$ HDA transition is also possible, and it is not fully clear at the present moment if the HDA $\rightarrow$ VHDA transition is reversible like the HDA $\leftrightarrow$ LDA transition accompanied by a sharp decrease of density upon decompressing.

In figure 22 we show the visual inspection of HDA and VHDA during their transformation to LDA upon annealing at $P \sim 1$ bar, with a heating rate of $\sim$10 K min^{-1}. The picture at $T \sim 90$ K shows HDA (sample on the left side) and VHDA (sample on the right side). At $T \sim 110$ K, HDA has fully transformed to LDA, whereas VHDA is still unchanged. This is in agreement with the thermal data presented in figure 13(b). At $T \sim 115$ K, a slow process starts in the VHDA sample, which has run to completion at $T \sim 130$ K, where both samples are LDA. The transformation from VHDA to LDA observed in figure 22 seems to be much slower than the transformation from HDA to LDA, which might imply that the VHDA $\rightarrow$ LDA transition proceeds in two stages: VHDA $\rightarrow$ HDA $\rightarrow$ LDA. The fact that the VHDA $\rightarrow$ HDA stage is difficult to observe at $P \sim 1$ bar (in many studies just the VHDA $\rightarrow$ LDA transition has been observed) might be related to kinetics. In figure 22, it is evident from the image recorded at $T \sim 110$ K that the activation energy to convert VHDA to LDA is higher than the activation energy to convert HDA to LDA. The overall VHDA to LDA transition shows an activation barrier $\Delta E > 53$ kJ mol^{-1}, which exceeds the barrier for the HDA to LDA transition by more than 20 kJ mol^{-1} according to neutron diffraction data [90]. The much lower barrier from HDA to LDA than that from VHDA to HDA may be the reason why it is experimentally very difficult to stop the VHDA $\rightarrow$ LDA transformation at an intermediate HDA stage: once the VHDA $\rightarrow$ HDA energy barrier is surmounted, VHDA transforms immediately to LDA. From this discussion it seems possible that HDA can be produced from VHDA at ambient pressure. Nevertheless, to unambiguously confirm that LDA, HDA, and VHDA each occupy a different megabasin in configurational space, it is necessary to fully clarify the issue of reversibility for the HDA $\rightarrow$ VHDA transition. Experiments are needed which carefully increase the temperature in small steps between $\sim$110 and $\sim$140 K at ambient pressure *and* at elevated pressures to investigate the possibility that HDA can be produced from VHDA.

We note that the difference in the activation energies of the VHDA $\rightarrow$ LDA and HDA $\rightarrow$ LDA transformations is consistent with the results of section 3.1.3 discussing the compression of LDA at $T \sim 125$ K. The second densification step in the compression curve of LDA, corresponding to the HDA $\rightarrow$ VHDA transformation, starts to smear out and lose its abruptness at compression rates of $\geqslant$600 MPa min^{-1} (the first densification step, corresponding to the LDA $\rightarrow$ HDA transformation, is still abrupt at the same rate). Thus, in accordance with the neutron diffraction result at ambient pressure, this implies that the activation barrier

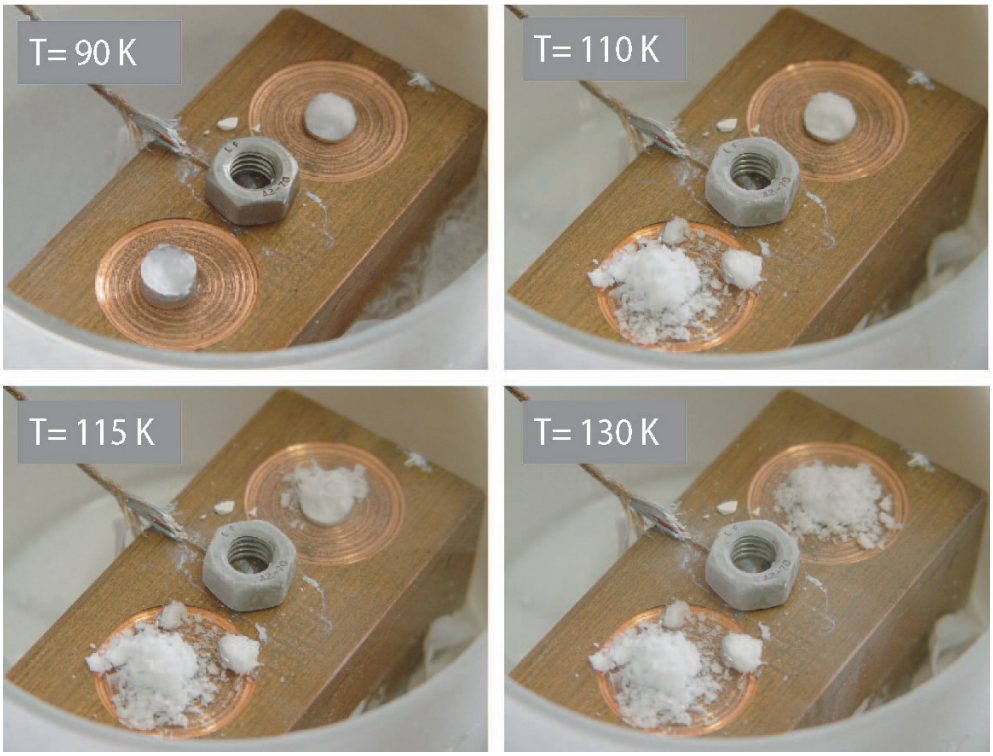

Figure 22. Visual inspection of HDA and VHDA during their transformation to LDA upon annealing at $P \sim 1$ bar, with a heating rate of $\sim$10 K min^{-1}. The picture at $T \sim 90$ K shows HDA (sample on the left side) and VHDA (sample on the right side). At $T \sim 110$ K, HDA has fully transformed to LDA, whereas VHDA is still unchanged. At $T \sim 115$ K, a slow process starts in the VHDA sample, which has run to completion at $T \sim 130$ K, where both samples are LDA. It is evident from the image recorded at $T \sim 110$ K that the activation energy to convert VHDA to LDA is higher than the activation energy to convert HDA to LDA. We estimate the accuracy of the temperature measurement to be ± 5 K in this set-up.

between LDA and HDA is much lower than the barrier between HDA and VHDA also at elevated pressures. It therefore seems that the VHDA $\rightarrow$ HDA step is rate limiting in view of the higher activation barrier.

In experiments, isobaric heating of recovered VHDA at $P = 0.11$ GPa, from $T = 77$ K to $T \sim 127$ K, results in LDA [68]. The same recipe is followed in the simulations of references [91, 180] when annealing recovered VHDA at $P = 0$ GPa. Figure 15(a) shows that the density of the system in the P–ρ plane upon annealing VHDA at $P = 0$ GPa reaches that of LDA. Thus, the VHDA $\rightarrow$ LDA transformation can be reproduced with the TIP4P model. The results obtained with the SPC/E model [118] are shown in figure 23. The blue arrow indicates the change in density upon isobarically heating recovered VHDA at $P = 0.11$ GPa. Upon heating, the system expands. However, the density of the system, before the glass transition temperature is reached, is higher than the corresponding density of LDA. Figure 23 shows that upon heating, the density of the amorphous ice evolves towards that of the low-T liquid state. If the isobaric heating of recovered VHDA is performed at $P = -0.3$ GPa, the system cannot be trapped in the liquid phase in the P–ρ plane because there are no liquid states at such pressure (see figure 23). Therefore, upon heating at $P = -0.3$ GPa, the density of the system in figure 23

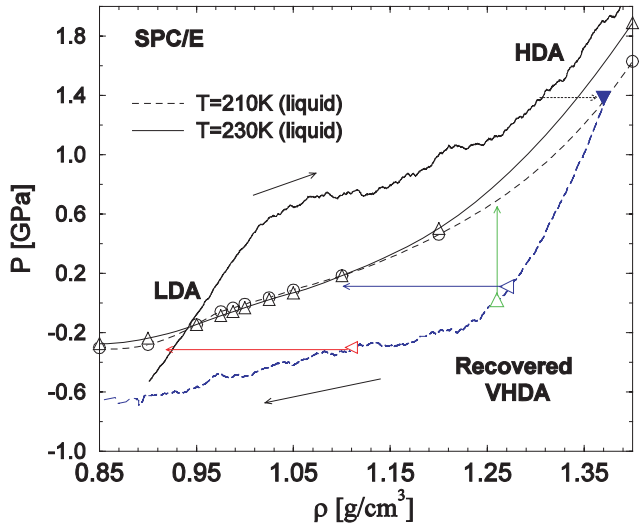

Figure 23. Effect of heating decompressed VHDA at constant pressure and constant volume from MD simulations using the SPC/E model. Liquid isotherms (circles and up triangles), the compression curve of LDA at $T = 77$ K (thick solid line), and the decompression curve of VHDA at $T = 77$ K (dashed (blue) line) are taken from figure 15(a). Horizontal (blue and red) arrows (at $P \sim 0$ GPa and $P \sim -0.3$ GPa, respectively) show the density change upon annealing decompressed VHDA up to $T \sim 170$ K. Only at $P \sim -0.3$ GPa does VHDA seem to transform to LDA. The vertical (green) arrow indicates the pressure change upon heating HDA isochorically at $\rho \sim 1.26$ g cm^{-3}. At the present heating rate, VHDA does not transform to HDA and the system gets trapped in the liquid isotherms before reaching the pressure corresponding to HDA.

(red arrow) evolves towards that of LDA, supporting the presence of a VHDA $\rightarrow$ LDA transformation.

The experiments suggest that VHDA can transform to HDA upon isochoric heating of recovered VHDA at $\rho \sim 1.25$ g cm^{-3} ($P = 0.02$ GPa) [68]. However, the x-ray patterns of HDA, produced from ice I_h at $T = 77$ K, and 'HDA', produced upon isochoric heating of VHDA, show a slight shift in the peak maximum and a reduced full width at half maximum. The evolution of the system in the P–ρ plane upon isochoric heating of recovered VHDA at $\rho \sim 1.26$ g cm^{-3} is shown in figure 23 (vertical (green) arrow). In agreement with our discussion in section 3.1.2.2, the system gets trapped in the liquid state and no VHDA $\rightarrow$ HDA transformation is observed. The heating rate used in the simulations corresponding to figure 23 is 10^{10} K s^{-1}. It is not clear whether a much smaller heating rate (nowadays not accessible in computer simulations) will show a VHDA $\rightarrow$ HDA transformation. In the short term, experiments may help to clarify this issue.

4. Structure of amorphous ices

4.1. Experimental results

It is straightforward to extract structural properties from MD simulations both at ambient and at elevated pressures. However, it is experimentally cumbersome to determine the structure of amorphous samples *in situ* by diffraction methods, i.e. directly in the pressurized sample holder. For this reason amorphous ice samples prepared at high pressures are usually first quenched under pressure to liquid nitrogen temperature ($T = 77$ K), and only when a temperature of 77 K has been reached is the pressure released. The *recovered* samples at

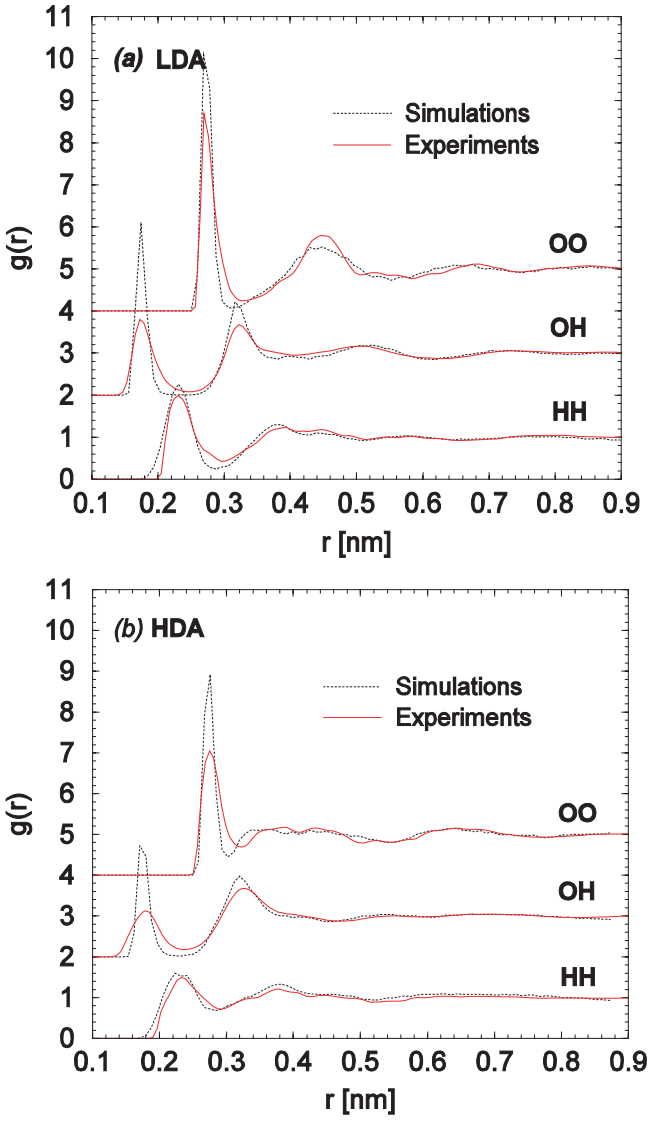

Figure 24. Comparison of the oxygen–oxygen (OO), oxygen–hydrogen (OH), and hydrogen–hydrogen (HH) radial distribution functions of (a) LDA and (b) recovered HDA at $T = 77$ K and $P = 0.02$ GPa, from experiments and computer simulations using the SPC/E model (experimental data from [80]; computer simulations data from [118]).

$T = 77$ K and $P = 1$ atm can be transferred to conventional cooled sample holders employed, e.g., for diffraction, spectroscopy, or calorimetry studies. It is assumed that upon release of pressure only elastic changes take place, i.e. molecular connectivity remains the same as at high pressure—just the density is lowered by decompression. With the few exceptions of structural studies performed directly in the high-pressure Paris–Edinburgh cell [201–203] and studies performed in a hydrothermal diamond anvil cell [204–206], all structural studies have been performed on recovered samples.

Examples of measured and calculated radial distribution functions (RDFs) obtained for LDA, HDA, and VHDA are shown in figures 24 and 25. The site–site radial distribution

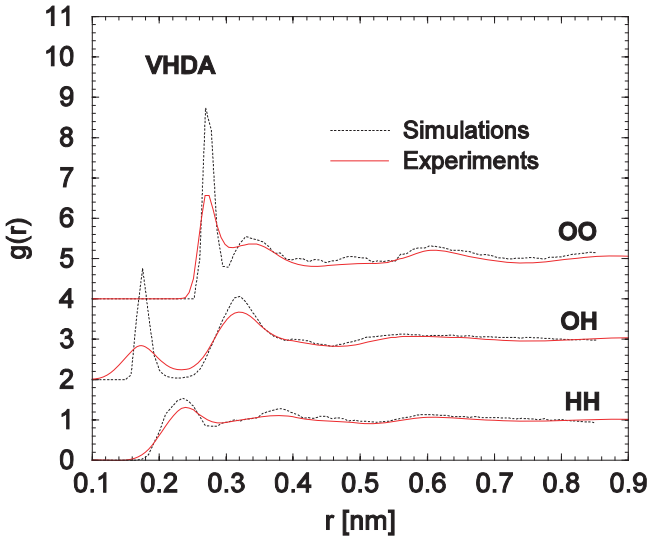

Figure 25. The same as figure 24 for VHDA (experimental data from [200]; computer simulation data from [118]).

functions $g_{OO}(r)$, $g_{OH}(r)$, and $g_{HH}(r)$ of recovered amorphous ices LDA, HDA, and VHDA have been determined by neutron diffraction with isotope substitution [200, 207, 208]. In earlier work $g_{OO}(r)$ was also determined for recovered HGW [209] and HDA [210, 211] by x-ray diffraction. Peak positions and heights of these RDFs are consistent with the RDFs derived from neutron diffraction data. According to both techniques all of the structures are fully amorphous, i.e. there are no signs of micro- or nano-crystallinity, even though the local order in LDA is similar to the local order in hexagonal ice I_h, and the local order in VHDA resembles the local order in high-pressure ices such as ice VI, ice VII, and ice XII. In fact, domains of ice I_h would need to be smaller than 15 Å, i.e., approximately two unit cells, to obtain diffraction patterns consistent with LDA, and domains of ice VI would need to be less than 20 Å for removal of crystalline features in the structure factor [208]. All samples are fully hydrogen-bonded with local tetrahedral arrangement of the oxygen atoms. The difference between LDA, HDA, and VHDA is found when looking beyond the first-neighbour peaks: the intermolecular coordination number as obtained by integrating $g_{OO}(r)$ between 2.3 and 3.3 Å is 3.9 ± 0.1 for LDA, 5.0 ± 0.1 for HDA, and 5.8 ± 0.1 for VHDA. That is, in the case of HDA, one interstitial water molecule approaches one plane of the tetrahedron formed by four oxygen atoms, and two interstitial water molecules approach two planes of this tetrahedron in the case of VHDA. These interstitial water molecules are essentially molecules pushed inwards from the second-neighbour shell and are reminiscent of the four non-bonded first-neighbour molecules found in ice VII [212]. In fact, amorphous ice compressed beyond 2.5–4 GPa at 77 K crystallizes to ice VII [204, 213]. The interstitial sites have been called 'lynch pin sites', since an activation barrier needs to be overcome to remove or add a water molecule to this site. The occupancy of the lynch pin sites is 0% for LDA, 50% for HDA, and 100% for VHDA. In the case of liquid water near ambient conditions the intermolecular coordination number is 4.3 ± 0.1; i.e., statistically 20% of the lynch pin sites are occupied. In other words, the structures of LDA, HDA, VHDA, and liquid water can be interconverted on the basis of water molecules moving from the second-neighbour shell to the lynch pin sites, without the necessity of a major network reorganization, e.g., by creating interpenetrating networks.

Additional neutron scattering and high-energy x-ray diffraction studies have shown that VHDA shows a better intermediate-range order than HDA and LDA [208]. Whereas for VHDA at least seven coordination shells are observed out to ∼20 Å, noticeable oscillations in the radial distribution functions are seen only up to ∼15 Å and ∼12 Å for HDA and LDA, respectively. The O–O distances as determined from the x-ray structure factors amount to 2.83, 2.80, and 2.75 Å for VHDA, HDA, and LDA, respectively. That is, the densest structure shows, somewhat counter-intuitively, the longest OH–O distances. These distances are in agreement with the estimates of 2.85, 2.82, and 2.76 Å, respectively, as obtained from a correlation between the OH–O distances with the decoupled ν(O–D) Raman band [68]. Therefore, it is plausible that in order to accommodate the fifth and/or sixth water molecule in the nearest-neighbour shell it is necessary that this first shell expands. A similar paradox has also been found for high-pressure crystalline phases [182].

In situ neutron diffraction studies at elevated pressures are possible using a specially designed pressure cell called the Paris–Edinburgh cell. In this cell, HDA has been studied at ∼100 K up to 2.2 GPa by neutron diffraction [203]. This study confirms that also under pressure major changes occur between the first- and second-neighbour shells. In fact at 2.2 ± 0.2 GPa the second shell contracts by ∼20 % and closely approaches the first shell, which itself remains intact. Similarly, in compressed liquid water also mainly the second shell contracts, whereas the first shell essentially remains unchanged [214]. The contraction in HDA is so strong that the intermolecular coordination number at 2.2 ± 0.2 GPa reaches eight; i.e., there are four hydrogen-bonded water molecules at a distance of ∼2.8 Å and four non-hydrogen-bonded water molecules at a distance of ∼3.5 Å from the central water molecule. At an intermediate pressure of 0.7 ± 0.1 GPa the coordination number is approximately six, implying that the structure of recovered VHDA resembles the structure of HDA at 0.7 GPa [213], which in turn resembles the structure of liquid water at 0.4 GPa [214]. Since the compression of HDA at 100 K up to ∼0.7 GPa is mainly elastic, the question arises of what the structural difference between HDA and VHDA is at elevated pressures. In this context it would be interesting to directly compare the HDA diffractogram recorded *in situ* at 100 K and ∼0.7 GPa with the *in situ* diffractogram of VHDA recorded at the same conditions (which is not yet available). There are two experimental hints, though, pointing in the direction that the structural difference between HDA and VHDA is becoming less pronounced as the pressure increases. First, the isothermal compressibility of VHDA at 77 K is ∼0.04 g cm^{-3} GPa^{-1} *lower* than the isothermal compressibility of HDA, but the density of VHDA at 1 bar and 77 K is *higher* by about 0.08 g cm^{-3} compared to the density of HDA at the same conditions [54]. This means that the densities of HDA and VHDA approach each other as the pressure increases. At about 2 GPa and 77 K the density of VHDA equals the density of HDA. Second, the d-spacings of unrelaxed HDA and of VHDA recorded at $T < 85$ K by *in situ* neutron diffraction also approach each other. On extrapolation of the data in figure 2 in [185], it seems that the d-spacings of HDA and VHDA intersect at about 2.2 GPa.

4.2. Results from computer simulations

4.2.1. LDA and HDA. The structure of LDA and HDA was also studied by simulations in [85]. In this work, it is shown that computer simulations are able to reproduce qualitatively the radial distribution functions (RDFs) of LDA and HDA at $P = 0$ GPa and $T = 80$ K. Below we compare the structures of LDA and recovered HDA with those from MD simulations using the SPC/E model. Similar conclusions can be drawn from the MD simulations using the TIP4P (see e.g., [91, 92, 117]) and ST2 models (see e.g., [60, 117]), and from the reverse Monte Carlo modelling technique of a flexible model of water [215].

Figure 24(a) shows $g_{OO}(r)$, $g_{OH}(r)$, and $g_{HH}(r)$ obtained from experiments [207] and simulations [118], at $P \sim 1$ atm and $T \sim 80$ K. Both LDA $g_{OO}(r)$ in figure 24(a) show maxima at $r \sim 0.27$, 0.44, and 0.67 nm. The first and second coordination shells are separated by a wide minimum at $r \sim 0.31$ nm. The first peak of $g_{OO}(r)$ obtained in simulations is higher and thinner than that from experiments. The $g_{OH}(r)$ and $g_{HH}(r)$ from experiments and simulations are also in qualitative agreement. The main differences occur in the height and width of the first peak of $g_{OH}(r)$ and the first two peaks of $g_{HH}(r)$: they are thinner and higher in the simulation RDFs than in the experimental ones.

Figure 24(b) shows the RDFs of HDA at $P \sim 1$ atm and $T \sim 80$ K. The structure of recovered HDA in simulations is in qualitative agreement with experiments, and it is independent of the procedure followed in the simulations to prepare HDA, i.e. whether HDA is formed upon compression of ice I_h [180] or LDA [118]. Both the $g_{OO}(r)$ shown in figure 24(b) have a first peak at $r \sim 0.27$ nm and a second wide peak at $r \sim 0.4$ nm. However, the first minimum of $g_{OO}(r)$ in simulations occurs at $r \sim 0.30$ nm, while in experiments it is found at $r \sim 0.32$ nm. Furthermore, in simulations the second wide peak of $g_{OO}(r)$ cannot be resolved into two peaks as clearly as in experiments. These differences in both the $g_{OO}(r)$ are also found in [85, 91, 180, 215].

Simulation and experiments indicate that LDA and HDA are characterized by a tetrahedrally coordinated fully hydrogen-bonded network. Integration of the first peak of the $g_{OO}(r)$ in figures 24(a) and (b) shows that each O atom in LDA and HDA has approximately four nearest-neighbour O atoms [92, 118, 207]. Furthermore, the integration of the first peak of $g_{OH}(r)$ indicates that in LDA and HDA O atoms have approximately two H neighbours [91, 92, 118, 207]. An analysis of the hydrogen-bond network indicates that more than 80% of the molecules have four hydrogen bonds in LDA and HDA [92]. Okabe *et al* [92] analyse the water structure in both instantaneous and inherent structures (local minima of the potential energy surface), and study different properties such as the RDFs, hydrogen bond (HB) distribution, Voronoi polyhedron statistics, and instantaneous normal modes. An interesting result from [92] is the analysis of the evolution of the ring statistics of the hydrogen-bond network in the ice $I_h \rightarrow$ HDA and recovered HDA $\rightarrow$ LDA transformations. This analysis shows a clear connection between the disruptions of the HBs and the density changes. For example, the starting sample of ice I_h is characterized by 720 rings formed by six water molecules. Instead, the HDA sample is composed only by 161 such rings, and mainly rings formed by four, five, and seven water molecules are found after compression (45, 109, and 49 rings, respectively). Moreover, it is found that in HDA there is no penetration of rings or crossing of HBs (as found e.g. in ice VII, where HB rings penetrate each other); instead, HDA is made by bending HBs.

The main differences in the $g_{OO}(r)$ of LDA and HDA occur for approximately $r > 0.31$ nm, i.e. beyond the first minimum of $g_{OO}(r)$. A comparison of figures 24(a) and (b) indicates that when going form LDA to HDA by compression the first peak of $g_{OO}(r)$ does not shift but becomes larger, the second peak becomes wider and smaller, and the third peak of $g_{OO}(r)$ shifts to lower values of r. In agreement with the discussion in the previous section, the main difference in the structure of LDA and HDA is the presence of an interstitial molecule between the first and second coordination shell, at $r \sim 0.32$ nm. Integration of the experimental $g_{OO}(r)$ (see figure 24(b)), from $r = 0.31$ nm (first minimum of the VHDA $g_{OO}(r)$) to $r = 0.33$ nm, indicates that, in this range of distances, an O atom has on average 0.9 oxygen neighbours. In simulations (see figure 24(b)), the integration of $g_{OO}(r)$ from $r = 0.303$ nm (first minimum of the VHDA $g_{OO}(r)$) to $r = 0.33$ nm indicates that O atoms have on average 1.1 oxygen neighbours. The presence of an interstitial molecule at $r \sim 0.32$ nm (as compared to LDA) has already been found in the

original work of Tse and Klein [85], and also confirmed recently in TIP4P simulations (see, e.g., [91]).

4.2.2. VHDA and annealed glasses.

4.2.2.1. Ring statistics of the hydrogen-bond network. In [91, 180], Martonak *et al* perform MD simulations and analyse the ring statistics of the hydrogen-bond network of VHDA at high pressure, after cooling VHDA back to $T = 80$ K. They also study the ring statistics of recovered HDA samples (at intermediate and low pressures, i.e. 0 GPa $< P <$ 1.3 GPa) after annealing and further cooling down to $T = 80$ K (as described in section 3.1.2.2). It is found [91, 180] that VHDA samples obtained at high pressures ($P > 1.0$ GPa) are characterized by eight- and nine-membered rings. Moreover, in agreement with reference [216], there is no evidence of interpenetrating networks. On the other hand, at low pressures ($P < 0.225$ GPa), the annealed samples (which correspond to LDA) are characterized by six- and seven-membered rings. At intermediate pressures corresponding to annealed samples of recovered HDA (0.225 GPa $< P <$ 1.0 GPa), the ring statistics evolves with increasing pressure, from that of LDA to that of VHDA: the number of six- and seven-membered rings decreases, while the numbered of eight- and nine-membered rings increases. Therefore, when comparing the structure of the *annealed samples* from $P = 0$ GPa up to $P \sim 2$ GPa, one observes first a *destruction* of the network topology of LDA (at $P \sim 0.15$–0.225 GPa), and then a *reconstruction* of the network topology upon approaching the pressures corresponding to VHDA ($P \sim 0.9$–1 GPa). For $P > 1$ GPa, it is found that the ring statistics almost stabilize, revealing that the reconstruction of the network is practically completed. No sign of discontinuity is observed in the ring statistics of the annealed amorphous ices at $P \sim 0.9$–1.0 GPa, i.e. in the hydrogen-bond network topology of HDA and VHDA. Such a discontinuity is expected if VHDA and HDA are separated by a first-order transition.

Upon isothermal decompression at $T = 80$ K, the annealed samples of HDA and VHDA show practically no change in the ring statistics of their HB network [180]. In other words, the hydrogen-bond network changes induced upon annealing at different pressures are frozen when the temperature is kept at $T = 80$ K, thereby confirming the validity of the experimental approach of analysing samples recovered at liquid nitrogen temperature. Upon decompression at this temperature, energy barriers cannot be crossed, and the system cannot relax via network reconstruction. The decompression thus proceeds predominantly via relaxation of the elastic compression. Because decompression does not alter the hydrogen-bond network of the annealed amorphous ices at different pressures, one finds that the high-density annealed states at $P > 1$ GPa, recovered at $P = 0$ GPa $T = 80$ K (with $\rho \sim 1.3$ g cm^{-3}), are characterized by eight- and nine-membered rings. As the density of the recovered states decreases toward 1 g cm^{-3} at $P = 0$ GPa, the number of eight- and nine-membered rings in the hydrogen-bond network decreases, while the number of five- and six-membered rings increases.

The presence of a *family* of HDA forms at $P = 0$ GPa, all with slightly different network topologies, may explain the experiments of [66, 87, 88] that suggest the presence of a continuum of amorphous states at $P = 0$ GPa. In these works, recovered HDA is isobarically heated at $P = 0$ GPa to intermediate temperatures between 80 and 120 K (before LDA is formed) and the system is allowed to relax at each temperature for few hours. At each intermediate temperature, the system shows a relaxation towards a different state that depends on the temperature chosen. As discussed in section 3.2.1, the idea of a family of HDA states is also supported by Koza *et al* [89]. These experiments suggest that upon heating HDA at $P = 0$ GPa from $T = 77$ K a family of HDA states occurs before the transition to LDA. The

observation of a continuum of states, though, does not rule out that there is a first-order-like transition between 'relaxed' HDA and LDA [89].

4.2.2.2. Radial distribution functions and coordination numbers. Experimental data of the structure of VHDA have been reported at $T = 80$ K and $P \sim 1$ atm [200]. To compare the structure of VHDA from experiments and simulations we discuss first the structure of recovered VHDA at $P \sim 0$ GPa and $T = 80$ K reported from MD simulations using the TIP4P [91, 180] and SPC/E models [118, 187]. The VHDA structures predicted by these two water models are remarkably similar to each other. Thus, we discuss mainly the results using the SPC/E model. Figure 25 shows the RDFs from experiments [200] and MD simulations [118]. A comparison of both the experimental and simulated RDFs in figures 24(b) and 25 shows that, when going from HDA to VHDA, the first peak of $g_{OO}(r)$ does not shift but decreases, and the third peak shifts to lower values of r. The second wide peak of the $g_{OO}(r)$ of HDA at $r \sim 0.44$ nm disappears. The main difference in the $g_{OO}(r)$ of HDA and VHDA obtained from experiments and simulations occurs at $r \sim 0.33$ nm. In experiments, the second peak of the HDA $g_{OO}(r)$ merges, upon annealing, into the first peak, filling the gap at $r \sim 0.33$ nm (first minimum of $g_{OO}(r)$). As a consequence, the first peak of $g_{OO}(r)$ develops a shoulder (with a second maximum at $r \sim 0.35$ nm). In simulations, such a shoulder does not exist and, instead, the second maximum of $g_{OO}(r)$ occurs at $r \sim 0.33$–0.34 nm. Therefore, in simulations, the first minimum of HDA does not disappear when going to VHDA, and there is still a clear minimum in the VHDA $g_{OO}(r)$ at $r \sim 0.30$ nm (see also figure 2 in [91]). When going from HDA to VHDA, the $g_{OH}(r)$ and $g_{HH}(r)$ barely change (see figures 24(b) and 25).

Experiments show that, similarly to LDA and HDA, VHDA is characterized by a tetrahedrally coordinated fully hydrogen-bonded network [200]. Integration of the first maximum of $g_{OH}(r)$ ($r < 0.25$ nm) indicates that each O atom has on average 2.0 ± 0.1 H neighbours. Similarly, integration of the first peak of $g_{OO}(r)$ ($r < 0.31$ nm, the first minimum of the experimental VHDA $g_{OO}(r)$), indicates that each O atom has on average ∼4.0 O neighbours. Simulations agree with these results. The integration of the first peak of $g_{OH}(r)$ of VHDA ($r < 0.25$ nm) gives a value of ∼1.9–2.0, while integrating the first peak of $g_{OO}(r)$ (approximately $r < 0.30$ nm, first minimum of the simulated VHDA $g_{OO}(r)$) gives a value of 4.0–4.1. Experiments also indicate that differences between HDA and VHDA, as compared to LDA, arise from the presence of interstitial neighbours between the first and second shells. Integration of the experimental $g_{OO}(r)$ from $r = 0.31$ nm (first minimum of $g_{OO}(r)$ of VHDA) to $r = 0.33$ nm (first minimum of $g_{OO}(r)$ of HDA) indicates that an O atom has 0.9 oxygen neighbours in HDA (i.e. approximately one interstitial molecule) and 1.7 in VHDA (i.e. approximately two interstitial molecules). In simulations, integrating from approximately $r > 0.30$ nm (first minimum of $g_{OO}(r)$ of VHDA) to $r = 0.33$ nm results in 1.1 and 1.8 neighbour O for HDA and VHDA, respectively. VHDA is characterized by medium-range order, showing at least seven well defined shells [208]. This medium-range order extends almost up to $r \sim 2$ nm. The simulations of reference [180] agree with this experimental result, and show that the medium-range order is likely to be related to the formation of large rings observed in the simulated VHDA.

The structures of the annealed amorphous states at $T = 80$ K and $0 < P < 1.95$ GPa are reported in the computer simulations of references [91, 180]. These amorphous solids are obtained from MD simulations using the TIP4P model as discussed in section 3.2.1 (see also figures 16(a) and 17(b)). The RDFs of these recovered glasses are shown in figure 26. The different $g_{OO}(r)$ in figure 26 indicate that a continuum of glasses with different structures can be obtained after annealing HDA at different pressures ranging from 0 to 1.95 GPa. These structures are intermediate between LDA and HDA for annealing pressures from 0.225 to

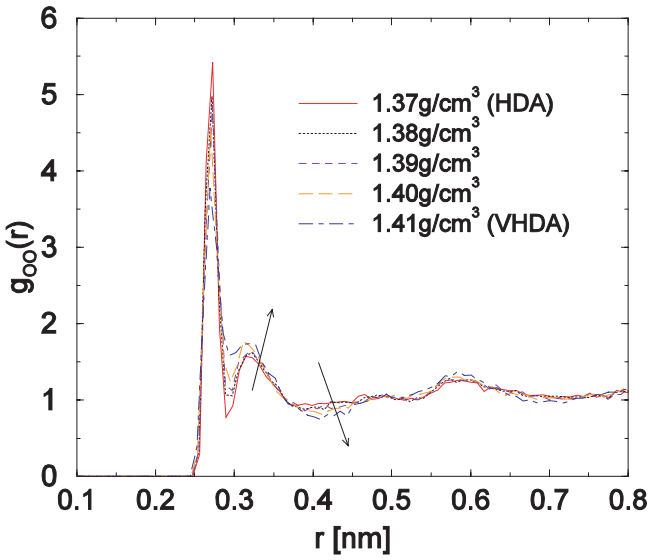

Figure 26. Oxygen–oxygen radial distribution functions of the annealed amorphous ices, at different pressures (see labels) after cooling back to $T = 80$ K (these amorphous ices correspond to the annealed glasses indicated in figure 16(a)). Results are from MD simulations using the TIP4P model (from [91]).

0.45 GPa and intermediate between HDA and VHDA at an annealing pressure of 1.05 GPa. Moreover, integration of the first peak of $g_{OO}(r)$ between $r = 0.23$ nm and $r = 0.33$ nm indicates that O atoms can have, on average, different numbers of nearest neighbours ranging in the interval 4.3 (after annealing at $P = 0.225$ GPa) to ∼6 (after annealing at $P > 1.5$ GPa). This suggests that the coordination number of five, observed for the experimental recovered HDA, can be regarded as accidental.

5. The relation between liquid and glassy water

5.1. HDA, VHDA, and the high-density liquid

In the liquid–liquid transition hypothesis, LDA and HDA are the glasses obtained upon isobaric cooling of the low- and high-density liquids, respectively. Independently of whether VHDA is considered a relaxed form of HDA or a new amorphous ice, the discovery of VHDA raises the question of how HDA and VHDA are connected to the high-density liquid. At the present time, this question has been addressed mainly in numerical works; experiments at high pressure connecting the liquid and amorphous phases are difficult to perform due to crystallization (experimental studies relating to the glass–liquid transition in LDA and (V)HDA are summarized in section 2.3.4.2). MD simulations show that VHDA can be obtained upon isobaric cooling of HDL at $P \sim 1.4$ GPa [56, 187]. Similarly, isochoric cooling of HDL at $\rho \sim 1.3$ g cm^{-3} shows that VHDA is the glass related to HDL [56, 187]. However, it has also been suggested that the variety of HDA ices, which exist as metastable forms at $P = 0$ GPa, corresponds to a variety of topologically different HDLs at different pressures [180].

In a recent work, Guillot and Guissani [56] address, for the first time, the formation of VHDA from the high-density liquid from numerical simulations. Using their own water model [217], they cool *isochorically* liquid water at $\rho = 1.3$ g cm^{-3} from $T = 300$ K

down to $T = 60$ K at a quenching rate of $q_c = -10^{11}$ K s^{-1}, and then recover the resulting amorphous ice at $P \sim 0$. The density of this amorphous ice is $\rho = 1.245$ g cm^{-3}, close to the experimental VHDA density. This led the authors to propose that the resulting amorphous ice is VHDA. We note that the procedure followed in [56] to obtain VHDA is not the one followed in experiments. However, their results suggest that isochoric cooling of high-density liquid (at least at $q_c = -10^{11}$ K s^{-1}) produces VHDA.

Guillot and Guissani also obtain HDA upon compression of cubic ice at different temperatures. The corresponding samples of recovered HDA at $P \sim 0$ have a lower density than that of VHDA; the higher the compression temperature, the higher the density of the recovered HDA (for a compression temperature of 50 K, the density of the recovered HDA at $P \sim 0$ is $\rho = 1.16$ cm^3, in agreement with experiments). When HDA and VHDA are heated isobarically at $P \sim 0$ [56], they transform to LDA forms with slightly different densities. The LDA form obtained upon heating HDA exhibits thermodynamic, structural, and dynamic properties very close to those of hyperquenched glassy water (i.e. the glass obtained upon isobaric ($P \sim 0$) cooling of normal liquid water). It seems from reference [56] that the resulting LDA obtained upon heating is sensitive to the thermodynamic path followed in the transformation from HDA or VHDA. Thus, although only two LDA forms were identified in [56], it is possible that in their simulations many other LDA forms can be obtained by slightly different thermodynamic paths (e.g., paths involving heating and isothermal annealing), all of them constituting a family of LDAs.

Computer simulations using the SPC/E model [187] show that *isobaric* cooling of the high-density liquid at $P = 1.38$ GPa, from $T = 300$ K down to $T = 77$ K, results in VHDA. VHDA in [187] is obtained upon annealing HDA at $P = 1.38$ GPa (HDA is obtained upon isothermal compression of LDA at $T = 77$ K from $\rho = 0.9$ g cm^{-3} up to $\rho = 1.31$ g cm^{-3} ($P = 1.38$ GPa)). The $P(\rho)$ curve obtained during the LDA $\rightarrow$ HDA $\rightarrow$ VHDA transformations can be traced in figure 15(b). The evolution of $\rho(T)$ during the HDA $\rightarrow$ VHDA transformation, from $T = 77$ K up to $T = 165$ K, is shown in figure 27(a) (dashed line). A '*slow*' heating rate of $q_h = 30$ K ns^{-1} is used along this path. The figure also shows $\rho(T)$ upon cooling VHDA from $T = 165$ K down to $T = 77$ K (dotted line) at a '*slow*' cooling rate of $q_c = -30$ K ns^{-1}.

The evolution of $\rho(T)$ upon cooling HDL from $T = 300$ K down to $T = 77$ K is included in figure 27(a) for different cooling rates. Only the (fast) cooling at $q_c = -10^4$ K ns^{-1} results, at $T = 77$ K, in an amorphous ice with the density corresponding to VHDA (solid line). A cooling rate of $q_c = -10^4$ K ns^{-1} is one of the fastest rates that can be simulated with the available computer times. The fact that the density of HDA at $T = 77$ K is lower than that of the amorphous ice obtained at $q_c = -10^4$ K ns^{-1} from HDL indicates that HDA *cannot* be obtained from HDL upon isobaric cooling *in the present simulations at the available timescales*. A slower $|q_c|$ produces an amorphous ice that is denser than VHDA (see, e.g., dot-dashed line in figure 27(a)). However, the slower the heating rate in the HDA $\rightarrow$ VHDA transformation, the denser the VHDA form. Thus, it is expected that, at least in simulations, VHDA obtained with different heating rates can be put into a one-to-one correspondence to an amorphous ice obtained upon isobaric cooling of HDL for some q_c.

It should be clear from the present discussion that the cooling/heating and compression rates are essential variables when discussing the connection of glassy and liquid water. The results obtained from figure 27(a) are relative to a 'timescale' that can be defined by the total simulation time during the HDA $\rightarrow$ VHDA transformation. For the present case, the simulated LDA $\rightarrow$ HDA transformation takes 8.2 ns (corresponding to a compression rate of 5×10^{-5} g cm^{-3} ps^{-1}). Accordingly, the slowest cooling rate to cool HDL from $T = 300$ K down to $T = 77$ K in [187] is $q_c = -30$ K ns^{-1}, the cooling simulation time being 7.43 ns.

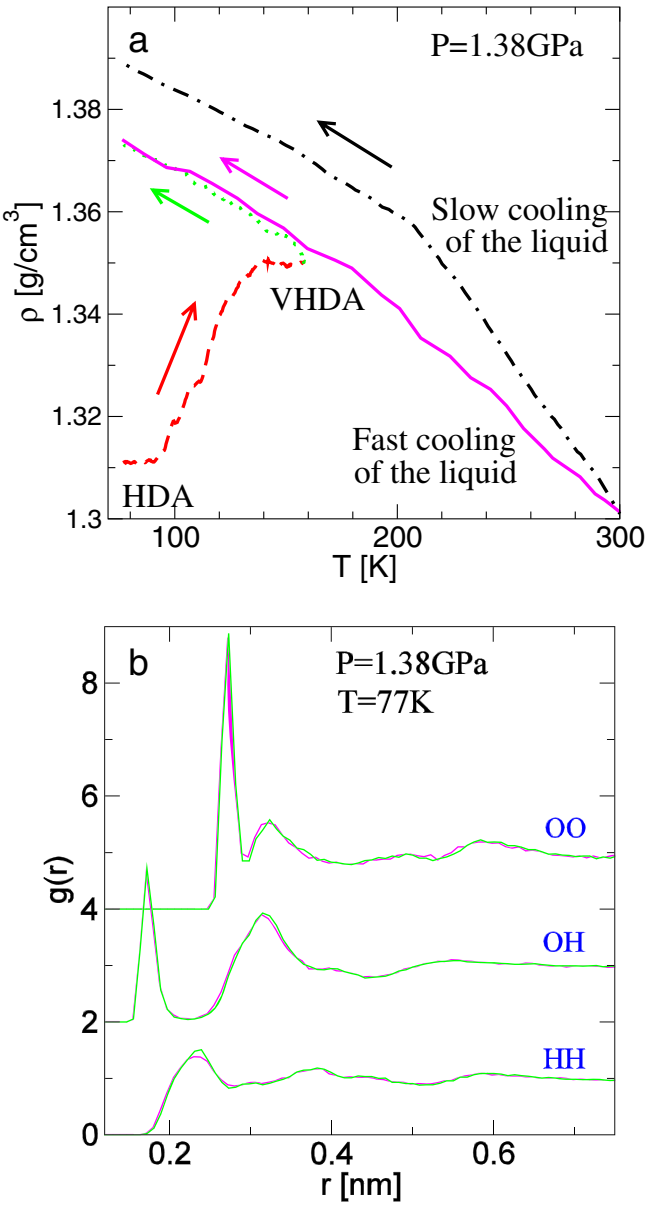

Figure 27. (a) Comparison of the thermodynamic path followed by the system in two independent computer simulations using the SPC/E model: (i) the formation of VHDA, and (ii) cooling of the liquid at high pressure. The dashed line corresponds to the annealing of HDA while the dotted line corresponds to the subsequent cooling of VHDA down to $T = 77$ K. Cooling of the liquid at -30 K ns^{-1} and -10^4 K ns^{-1} are indicated by the dot-dashed and solid lines. (b) Oxygen–oxygen (OO), oxygen–hydrogen (OH), and hydrogen–hydrogen (HH) radial distribution functions of the glasses obtained along the dotted/dashed lines and solid lines, at $T = 80$ K. The thermodynamic and structural properties of the fast cooled liquid coincide with those of VHDA (from [187]).

Figure 27(b) compares the RDFs from both VHDA and the amorphous ice obtained from HDL at $q_c = -10^4$ K ns^{-1}. The agreement in the corresponding RDFs indicates that both amorphous ices, which are obtained from two *independent* thermodynamic trajectories,

have not only the same thermodynamic properties (figure 27(a)) but also the same structure (figure 27(b)).

5.2. *Glasses obtained upon compression of LDA and upon cooling liquid water*

In [218], the amorphous ices obtained from MD simulations upon compression of LDA (using the SPC/E model) are compared to those obtained upon isochoric cooling of liquid water at different densities and cooling rates (30 K ns^{-1} $< |q_c| <$ 10^5 K ns^{-1}). It is found that, in general, both kinds of amorphous ices are different from both the thermodynamic and structural points of view.

Figure 28(a) shows $P(\rho)$ upon compression of LDA at $T = 0$ K. The advantage of using a compression temperature of $T = 0$ K is that there are no ageing effects involved. The location in the P–ρ plane of the amorphous ices obtained upon isochoric cooling of liquid water with different cooling rates is also shown in figure 28(a). LDA is obtained upon isobaric cooling of the liquid. Therefore, at $\rho = 0.9$ g cm^{-3}, the amorphous ices obtained upon cooling reach almost the same pressure as the starting LDA. At $\rho > 0.9$ g cm^{-3}, the amorphous ices obtained upon cooling the liquid have a much lower P than those obtained upon compression of LDA.

The differences in structure between these amorphous ices is studied in [218] by using order parameters or metrics. Two order parameters are used, a translational order parameter, τ, and an orientational order parameter, Q. Both order parameters were used in [219] to study the structure of liquid water. τ is a measurement of how different the oxygen–oxygen RDF is from unity. The more structured the glass is, the more $g_{OO}(r)$ deviates from unity, and thus the larger τ is. Q is a measurement of how similar the arrangement of a molecule and its four nearest neighbours is to a tetrahedral configuration (water is characterized by a local tetrahedral hydrogen-bond network). While $\tau > 0$, the range of Q is $[-3, 1]$; $Q = 1$ for a perfect tetrahedral configuration such as that of hexagonal ice (for a precise definition of Q and τ, please refer to [218, 219]). The advantage of using the (Q, τ) order parameter is that it is found that they are more sensitive to the glass structure than $g_{OO}(r)$ is [218].

Figure 28(b) shows the location of the amorphous ices in the Q–τ plane. The irregular solid line corresponds to the amorphous ices obtained upon compression (see also figure 28(a)). The location of the amorphous ices obtained by isochoric cooling of liquid water, at a given density and for all different cooling rates studied, falls on a single line in the Q–τ plane [218] (the cooling rate decreases as one moves to larger values of Q along this line). The solid straight lines in figure 28(b) indicate the location of the amorphous ices obtained by isochoric cooling at different densities (see also figure 28(a)).

Figure 28(b) shows that among the low-ρ isochorically cooled glasses ($\rho = 0.9, 1.0$ g cm^{-3}) only those cooled at slow cooling rates fall into the LDA region in the Q–τ plane. For intermediate and large cooling rates, the structure of these glasses corresponds to glasses lying between LDA and HDA in the Q–τ plane. Based on their density, high-ρ isochorically cooled glasses ($\rho > 1.2$ g cm^{-3}) are expected to fall in the HDA region. However, even the slow-cooled glasses are located in the region between those of LDA and HDA. Therefore, isochorically cooled glasses in the appropriate density range cannot always be classified as LDA or HDA.

The results of figure 28 indicate that glasses obtained by compression in the LDA $\rightarrow$ HDA transformation are structurally and thermodynamically different from those obtained by isochoric cooling (at least with the available timescales in simulations). A comparison of the potential energy landscape properties of the amorphous ices obtained upon compression of LDA and those of *equilibrium* liquids, also show dramatic differences [119]. From the theoretical point of view, it would be interesting to compare the results described in this section,

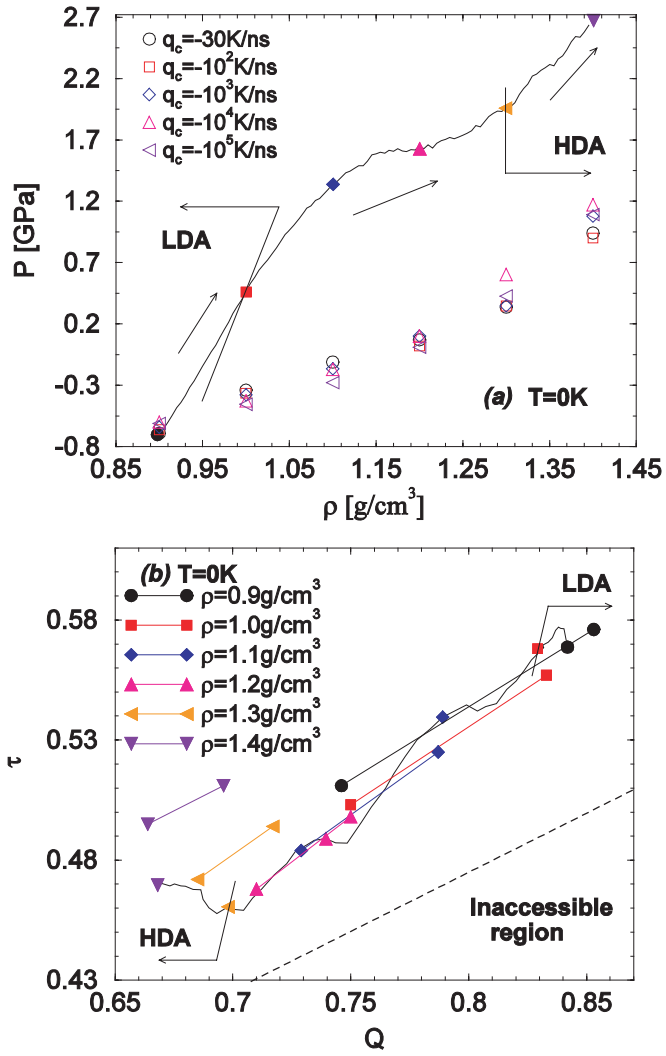

Figure 28. (a) Comparison of the location in the P–ρ plane of the glasses at $T = 0$ K obtained by isothermal compression of LDA (black line, filled symbols) and by isochorically cooling the liquid at different densities and cooling rates (open symbols). (b) Location in the Q–τ plane. Results from computer simulations using the SPC/E model (from [218]).

obtained with the SPC/E model, to those from other potentials such as the ST2 or TIP5P models. Finally, we note that the extremely different timescales in simulations and experiments imply that the numerical results should always be taken with caution.

6. Conclusions

While liquid water and its anomalous behaviour have been studied for more than 300 years [220] the study of glassy water is relatively new: LDA was discovered ∼70 years ago [62], and HDA was obtained ∼20 years ago [66]. There have been some excellent reviews about the topic of supercooled water and amorphous ices [5–11]. The discovery

of HDA demonstrated that a substance could have more than one amorphous solid state (polyamorphism). Since then, much research has focused on understanding the behaviour of glassy water. According to the database 'Chemical Abstracts Plus' (implemented in 'SciFinder Scholar'), the number of entries for 'amorphous ice' has increased constantly by ∼30% in any 5 year period since 1984, and it increased by ∼70% in the period between 2001 and 2005 (as of May15 2006). The sharp increase of publications on amorphous ice in 2001 is most probably due to the discovery of VHDA that year (about one-third of these studies in the last 5 years refer to VHDA).

The latest review addressing the topic of amorphous ice was published in 2004 [5–11]. In the last three years the field has evolved rapidly and many theoretical as well as experimental studies have appeared. A close comparison between experimental and computer simulation results is needed. Such a comparison has been the main focus of this work, starting from the discovery of HDA and LDA, until the recent works related to VHDA.

Most of the open questions on glassy water that we had a few years ago are still unanswered (see [5–11]).

(i) Does water possess a second critical point (CP)? If so, is this CP accessible in experiments? Finding the postulated second CP would prove that the liquid–liquid transition hypothesis (instead of the singularity-free scenario [5–11]) is the right scenario to explain the anomalous behaviour of supercooled and glassy water. The possibility that the glass transition temperature, T_g, is lower than the crystallization temperature opens the door to explore deeply supercooled liquid water at $T \sim T_g$, and thus to observe the liquid–liquid transition line. This would also confirm that LDA and HDA are separated by a first-order transition line.

(ii) Are LDA and HDA 'families' of amorphous ices, as computer simulations and some experiments suggest? If so, how can we characterize these families of states? Answering this question implies understanding the effects of ageing and annealing in glassy water.

The discovery of VHDA prompted new relevant questions.

(i′) Is VHDA a relaxed HDA? Or is it a new amorphous state, different from HDA and LDA? While some computer simulations confirm the idea of a phase separation between LDA and HDA as well as HDA and VHDA [192–195] (and between the corresponding liquid states), other simulations rather draw a picture of a phase separation between LDA and HDA, but not between HDA and VHDA, VHDA being just an annealed form of HDA [56, 91, 187]. Also from the experimental side the available data can be interpreted in favour of either view. It is still open to check if the conversion from one amorphous state to the other occurs at a single pressure or over a range of pressures. Another experimental challenge is to distinguish whether VHDA can be converted back to HDA. In particular, is the VHDA to LDA transition at $P \sim 0$ GPa a one-step process? Or is it a two-step process, involving HDA as an intermediate phase?

(ii′) The discovery of a new glass would require a re-examination of the phase diagram of metastable water. In particular, it implies that the liquid–liquid transition hypothesis involving phase separation between two liquids should be amended or may be even discarded. Moreover, if VHDA is a new amorphous ice, does the HDA–VHDA first-order transition line end up in a third CP, as suggested by some computer simulations [192–195]? Or does it join the LDA–HDA first-order transition line, both lines ending in a common second CP?

(iii′) Whether VHDA is a relaxed HDA or a new amorphous ice: what is the connection between liquid and glassy water? In particular, can any amorphous ice (obtained by

compression/decompression and/or cooling/heating of ice or glassy water) be put in a one-to-one correspondence with an amorphous ice obtained upon cooling the liquid? Is there a glass transition at a temperature below crystallization ($T_g < T_X$) for LDA, HDA, and VHDA? Answering these questions requires a thorough understanding of transformations between disordered states at low temperatures, which will probably require a few more decades of effort, e.g., to learn more about the effects of cooling/heating and compression/decompression rates in the glass and liquid states.

Acknowledgments

TL is grateful to the Austrian Science Fund (FWF, grant no R37-N11) for supporting this work and to Erwin Mayer, Paul F McMillan, Richard J Nelmes and Ivan Brovchenko for helpful discussions. NG thanks P G Debenedetti, F Sciortino and H E Stanley for fruitful discussions.

Note added in proof. While this manuscript was under review, we noticed a recent pre-print (cond-mat/0512199) where simulations using the TiP4P-Ew model (Horn H W *et al* 2004 *J. Chem. Phys.* **120** 9665) using the volume–temperature replica exchange MD were reported. In these simulations, two liquid–liquid transitions are observed at positive pressures.

References

[1] Salzmann C G, Radaelli P G, Hallbrucker A, Mayer E and Finney J L 2006 *Science* **311** 1758
[2] Engelhardt H and Whalley E 1972 *J. Chem. Phys.* **56** 2678
[3] Lobban C, Finney J L and Kuhs W F 1998 *Nature* **391** 268
[4] Speedy R J and Angell C A 1976 *J. Chem. Phys.* **65** 851
[5] Angell C A 1983 *Annu. Rev. Phys. Chem.* **34** 593
[6] Angell C A 1982 *Water Compr. Treatise* vol 7 (New York: Plenum) p 1
[7] Debenedetti P G 1996 *Metastable Liquids* (Princeton, NJ: Princeton University Press)
[8] Mishima O and Stanley H E 1998 *Nature* **396** 329
[9] Debenedetti P G and Stanley H E 2003 *Phys. Today* 40
[10] Debenedetti P G 2003 *J. Phys.: Condens. Matter* **15** R1669
[11] Angell C A 2004 *Annu. Rev. Phys. Chem.* **55** 559
[12] Yarger J L, Angell C A, Borick S S and Wolf G H 1997 *ACS Symp. Series* **676** 214
[13] McMillan P F 2004 *J. Mater. Chem.* **14** 1506
[14] Smith K H, Shero E, Chizmeshya A and Wolf G H 1995 *J. Chem. Phys.* **102** 6851
[15] Durandurdu M and Drabold D A 2002 *Phys. Rev.* B **66** 041201
[16] Funamori N and Tsuji K 2002 *Phys. Rev. Lett.* **88** 255508
[17] Koga J, Okumura H, Nishio K, Yamaguchi T and Yonezawa F 2002 *Phys. Rev.* B **66** 064211
[18] Principi E, Di Cicco A, Decremps F, Polian A, De Panfilis S and Filipponi A 2004 *Phys. Rev.* B **69** 201201
[19] Morishita T 2004 *Phys. Rev. Lett.* **93** 055503
[20] Ha A, Cohen I, Zhao X, Lee M and Kivelson D 1996 *J. Phys. Chem.* **100** 1
[21] Cohen I, Ha A, Zhao X, Lee M, Fischer T and Kivelson D 1996 *J. Phys. Chem.* **100** 8518
[22] Wiedersich J, Kudlik A, Gottwald J, Benini G, Roggatz I and Roessler E 1997 *J. Phys. Chem.* B **101** 5800
[23] Senker J and Roessler E 2002 *J. Phys. Chem.* B **106** 7592
[24] Senker J and Rossler E 2001 *Chem. Geol.* **174** 143
[25] Kivelson D and Tarjus G 2002 *J. Non-Cryst. Solids* **307–310** 630
[26] Guinet Y, Denicourt T, Hedoux A and Descamps M 2003 *J. Mol. Struct.* **651–653** 507
[27] Tarjus G, Alba-Simionesco C, Grousson M, Viot P and Kivelson D 2003 *J. Phys.: Condens. Matter* **15** S1077
[28] Hedoux A, Guinet Y, Descamps M and Lefebvre J 2003 *Phase Transit.* **76** 831
[29] Derollez P, Hernandez O, Hedoux A, Guinet Y, Masson O, Lefebvre J and Descamps M 2004 *J. Mol. Struct.* **694** 131
[30] Saika-Voivod I, Poole P H and Sciortino F 2002 *NATO Sci. Series, II: Mathematics, Physics and Chemistry* vol 81, p 169
[31] Saika-Voivod I, Sciortino F and Poole P H 2004 *Phys. Rev.* E **69** 041503

[32] Saika-Voivod I, Sciortino F and Poole P H 2004 *Phil. Mag.* **84** 1437
[33] Saika-Voivod I, Poole P H and Sciortino F 2001 *Nature* **412** 514
[34] Durandurdu M and Drabold D A 2002 *Phys. Rev.* B **65** 104208
[35] Grande T, Stolen S, Grzechnik A, Crichton W A and Mezouar M 2002 *Physica* A **314** 560
[36] Huang L and Kieffer J 2004 *Phys. Rev.* B **69** 224203
[37] Huang L and Kieffer J 2004 *Phys. Rev.* B **69** 224204
[38] Sen S, Andrus R L, Baker D E and Murtagh M T 2004 *Phys. Rev. Lett.* **93** 125902
[39] Weber J K R, Abadie J G, Hixson A D, Nordine P C and Jerman G A 2000 *J. Am. Ceram. Soc.* **83** 1868
[40] Weber R, Benmore C J, Siewenie J, Urquidi J and Key T S 2004 *Phys. Chem. Chem. Phys.* **6** 2480
[41] Weber R and Nordine P 2001 *NASA Conf. Publication* **210827** 630
[42] Weber R and Nordine P 2001 *NASA Conf. Publication* **210827** 624
[43] McMillan P F, Wilson M and Wilding M C 2003 *J. Phys.: Condens. Matter* **15** 6105
[44] Wilding M C and McMillan P F 2001 *J. Non-Cryst. Solids* **293–295** 357
[45] Wilding M C, McMillan P F and Navrotsky A 2002 *Phys. Chem. Glasses* **43** 306
[46] Wilding M C, McMillan P F and Navrotsky A 2002 *Physica* A **314** 379
[47] Wilson M and McMillan P F 2004 *Phys. Rev.* B **69** 054206
[48] Tangeman J A, Phillips B L, Nordine P C and Weber J K R 2004 *J. Phys. Chem.* B **108** 10663
[49] Poole P H, Grande T, Angell C A and McMillan P F 1997 *Science* **275** 322
[50] Bachmann L and Mayer E 1987 *Cryotechniques in Biological Electron Microscopy* ed R A Steinbrecht and K Zierold (Berlin: Springer) p 3
[51] Bogdan A 2006 *J. Phys. Chem.* B **110** 12205
[52] Duman J G, Wu D W, Xu L, Tursman D and Olsen T M 1991 *Q. Rev. Biol.* **66** 387
[53] Chen L, DeVries A L and Cheng C H C 1997 *Proc. Natl Acad. Sci. USA* **94** 3817–22
[54] Loerting T, Schustereder W, Winkel K, Kohl I, Salzmann C G and Mayer E 2006 *Phys. Rev. Lett.* **96** 025702
[55] Mayer E 1985 *J. Appl. Phys.* **58** 663
[56] Guillot B and Guissani Y 2003 *J. Chem. Phys.* **119** 11740
[57] Matsumoto M, Saito S and Ohmine I 2002 *Nature* **416** 409
[58] Yamada M, Mossa S, Stanley H E and Sciortino F 2002 *Phys. Rev. Lett.* **88** 195701
[59] Mishima O 2001 *J. Chem. Phys.* **115** 4199
[60] Poole P H, Sciortino F, Essmann U and Stanley H E 1992 *Nature* **360** 324
[61] Mishima O, Calvert L D and Whalley E 1985 *Nature* **314** 76
[62] Burton E F and Oliver W F 1935 *Proc. R. Soc.* A **153** 166
[63] Jenniskens P and Blake D F 1994 *Science* **265** 753
[64] Jenniskens P, Blake D F, Wilson M A and Pohorille A 1995 *Astrophys. J.* **455** 389
[65] Brüggeller P and Mayer E 1980 *Nature* **288** 569
[66] Mishima O, Calvert L D and Whalley E 1984 *Nature* **310** 393
[67] Al-Amoudi A, Dubochet J and Studer D 2002 *J. Microsc.* **207** 146
[68] Loerting T, Salzmann C, Kohl I, Mayer E and Hallbrucker A 2001 *Phys. Chem. Chem. Phys.* **3** 5355
[69] Lepault J, Freeman R and Dubochet J 1983 *J. Microsc.* **132** RP3
[70] Baratta G A, Leto G, Spinella F, Strazzulla G and Foti G 1991 *Astron. Astrophys.* **252** 421
[71] Moore M H and Hudson R L 1992 *Astrophys. J.* **401** 353
[72] Strazzulla G, Baratta G A, Leto G and Foti G 1992 *Europhys. Lett.* **18** 517
[73] Sartori N, Bednar J and Dubochet J 1996 *J. Microsc.* **182** 163
[74] Strazzulla G, Baratta G A and Palumbo M E 2001 *Spectrochim. Acta* A **57** 825
[75] Leto G and Baratta G A 2003 *Astron. Astrophys.* **397** 7
[76] Kohl I, Mayer E and Hallbrucker A 2001 *Phys. Chem. Chem. Phys.* **3** 602
[77] Tse J S 1992 *J. Chem. Phys.* **96** 5482
[78] Mishima O 1996 *Nature* **384** 546
[79] Tse J S, Klug D D, Tulk C A, Swainson I, Svensson E C, Loong C-K, Shpakov V, Belosludov V R, Belosludov R V and Kawazoe Y 1999 *Nature* **400** 647
[80] Finney J L, Hallbrucker A, Kohl I, Soper A K and Bowron D T 2002 *Phys. Rev. Lett.* **88** 225503
[81] Floriano M A, Handa Y P, Klug D D and Whalley E 1989 *J. Chem. Phys.* **91** 7187
[82] Loerting T, Kohl I, Schustereder W, Hallbrucker A and Mayer E 2006 *Chem. Phys. Chem.* **7** 1203
[83] Röttger K, Endriss A, Ihringer J, Doyle S and Kuhs W F 1994 *Acta Crystallogr.* B **50** 644
[84] Whalley E 1986 *Water and Aqueous Solutions, Vol. Colston papers Nr. 37* ed G W Neilson and J E Enderby (Bristol: Hilger) p 105
[85] Tse J S and Klein M L 1987 *Phys. Rev. Lett.* **58** 1672
[86] Jorgensen W L, Chandrasekhar J, Madura J D, Impey R W and Klein M L 1983 *J. Chem. Phys.* **79** 926

[87] Tulk C A, Benmore C J, Urquidi J, Klug D D, Neuefeind J, Tomberli B and Egelstaff P A 2002 *Science* **297** 1320
[88] Guthrie M, Urquidi J, Tulk C A, Benmore C J, Klug D D and Neuefeind J 2003 *Phys. Rev.* B **68** 184110
[89] Koza M M, Schober H, Fischer H E, Hansen T and Fujara F 2003 *J. Phys.: Condens. Matter* **15** 321
[90] Koza M M, Geil B, Winkel K, Koehler C, Czeschka F, Scheuermann M, Schober H and Hansen T 2005 *Phys. Rev. Lett.* **94** 125506
[91] Martonak R, Donadio D and Parrinello M 2004 *Phys. Rev. Lett.* **92** 225702
[92] Okabe I, Tanaka H and Nakanishi K 1996 *Phys. Rev.* E **53** 2638
[93] Hemley R J, Chen L C and Mao H K 1989 *Nature* **338** 638
[94] Handa Y P, Mishima O and Whalley E 1986 *J. Chem. Phys.* **84** 2766
[95] Johari G P and Andersson O 2004 *J. Chem. Phys.* **120** 6207
[96] Gromnitskaya E L, Stal'gorova O V, Brazhkin V V and Lyapin A G 2001 *Phys. Rev.* B **64** 094205
[97] Sharma S M and Sikka S K 1996 *Prog. Mater. Sci.* **40** 1
[98] Stanley H E 1999 *Pramana* **53** 53
[99] Katayama Y, Mizutani T, Utsumi W, Shimomura O, Yamakata M and Funakoshi K-I 2000 *Nature* **403** 170
[100] Hemley R J, Jephcoat A P, Mao H K, Ming L C and Manghnani M H 1988 *Nature* **334** 52
[101] McNeil L E and Grimsditch M 1992 *Phys. Rev. Lett.* **68** 83
[102] Kingma K J, Meade C, Hemley R J, Mao H and Veblen D R 1993 *Science* **259** 666
[103] Grimsditch M, Popova S, Brazhkin V V and Voloshin R N 1994 *Phys. Rev.* B **50** 12984
[104] Grimsditch M 1984 *Phys. Rev. Lett.* **52** 2379
[105] Grimsditch M 1986 *Phys. Rev.* B **34** 4372
[106] Polian A and Grimsditch M 1990 *Phys. Rev.* B **41** 6086
[107] Susman S, Volin K J, Price D L, Grimsditch M, Rino J P, Kalia R K, Vashishta P, Gwanmesia G, Wang Y and Liebermann R C 1991 *Phys. Rev.* B **43** 1194
[108] El'kin F S, Brazhkin V V, Khvostantsev L G, Tsiok O B and Lyapin A G 2002 *JETP Lett.* **75** 342
[109] Hemley R J, Mao H K, Bell P M and Mysen B O 1986 *Phys. Rev. Lett.* **57** 747
[110] Meade C, Hemley R J and Mao H K 1992 *Phys. Rev. Lett.* **69** 1387
[111] Lyapin A G, Brazhkin V V, Gromnitskaya E L, Mukhamadiarov V V, Stal'gorova O V and Tsiok O B 2002 *NATO Sci. Series, II: Mathematics, Physics and Chemistry* vol 81, p 449
[112] Zaitsev A I, Shelkova N E, Lyakishev N P and Mogutnov B M 1999 *Phys. Chem. Chem. Phys.* **1** 1899
[113] Johari G P and Andersson O 2004 *Phys. Rev.* B **70** 184108
[114] Mishima O 1994 *J. Chem. Phys.* **100** 5910
[115] Pruppacher H R and Klett J D 1980 *Microphysics of Clouds and Precipitation* (Dordrecht: Reidel)
[116] Stillinger F H and Rahman A 1974 *J. Chem. Phys.* **60** 1545
[117] Poole P H, Sciortino F, Essmann U and Stanley H E 1993 *Phys. Rev.* E **48** 3799
[118] Giovambattista N, Stanley H E and Sciortino F 2005 *Phys. Rev.* E **72** 031510
[119] Giovambattista N, Stanley H E and Sciortino F 2003 *Phys. Rev. Lett.* **91** 115504
[120] Stillinger F H and Weber T A 1984 *Science* **225** 983
[121] Stillinger F H 1995 *Science* **267** 1935
[122] Sciortino F 2005 *J. Stat. Mech.* P05015
[123] Zhelezni B V 1969 *Russ. J. Phys. Chem.* **43** 1311
[124] Fine R A and Millero F J 1973 *J. Chem. Phys.* **59** 5529
[125] Angell C A, Shuppert J and Tucker J C 1973 *J. Phys. Chem.* **77** 3092
[126] Franks F 1982 *Water—a Comprehensive Treatise* vol 7, ed F Franks (New York: Plenum) chapter 1
[127] Speedy R J and Angell C A 1972 *J. Chem. Phys.* **65** 851
[128] Speedy R J 1982 *J. Phys. Chem.* **86** 982
[129] Speedy R J 1982 *J. Phys. Chem.* **86** 3002
[130] Mishima O 2000 *Phys. Rev. Lett.* **85** 334
[131] Poole P H, Essmann U, Sciortino F and Stanley H E 1993 *Phys. Rev.* E **48** 4605
[132] Poole P H, Saika-Voivod I and Sciortino F 2005 *J. Phys.: Condens. Matter* **17** L431
[133] Harrington S, Zhang R, Poole P H, Sciortino F and Stanley H E 1997 *Phys. Rev. Lett.* **78** 2409
[134] Mahoney M W and Jorgensen W L 2000 *J. Chem. Phys.* **112** 8910
[135] Paschek D 2005 *Phys. Rev. Lett.* **94** 217802
[136] Tanaka H 1996 *Nature* **380** 328
[137] Tanaka H 1996 *J. Chem. Phys.* **105** 5099
[138] Sciortino F, Poole P H, Essmann U and Stanley H E 1997 *Phys. Rev.* E **55** 727
[139] Starr F W, Bellissent-Funel M-C and Stanley H E 1999 *Phys. Rev.* E **60** 1084
[140] Sciortino F, La Nave E and Tartaglia P 2003 *Phys. Rev. Lett.* **91** 155701
[141] Scala A, Starr F W, La Nave E, Stanley H E and Sciortino F 2000 *Phys. Rev.* E **62** 8016

[142] Sastry S, Debenedetti P G, Sciortino F and Stanley H E 1996 *Phys. Rev.* E **53** 6144
[143] Stanley H E and Teixeira J 1980 *J. Chem. Phys.* **73** 3404
[144] Poole P H, Sciortino F, Grande T, Stanley H E and Angell C A 1994 *Phys. Rev. Lett.* **73** 1632
[145] Truskett T M, Debenedetti P G, Sastry S and Torquato S 1999 *J. Chem. Phys.* **111** 2647
[146] Jeffrey C A and Austin P H 1999 *J. Chem. Phys.* **110** 484
[147] Borick S, Debenedetti P G and Sastry S 1995 *J. Phys. Chem.* **99** 3781
[148] Roberts C J and Debenedetti P G 1996 *J. Chem. Phys.* **105** 658
[149] Franzese G and Stanley H E 2002 *J. Phys.: Condens. Matter* **14** 2201
[150] Ponyatovsky E G, Sinitsyn V V and Pozdnyakova T A 1994 *JETP Lett.* **60** 360
[151] Moynihan C T 1997 *Mater. Res. Soc. Symp. Proc.* **455** 411
[152] Ponyatovsky E G, Sinitsyn V V and Pozdnyakova T A 1998 *J. Chem. Phys.* **109** 2413
[153] Ponyatovsky E G and Sinitsyn V V 1999 *Physica* B **265** 121
[154] Sasai M 1990 *J. Chem. Phys.* **93** 7329
[155] Tanaka H 1998 *Phys. Rev. Lett.* **80** 5750
[156] Tanaka H 1999 *J. Phys.: Condens. Matter* **11** L159
[157] Tanaka H 2000 *Europhys. Lett.* **50** 340
[158] Tanaka H 2000 *J. Chem. Phys.* **112** 799
[159] Tanaka H 2000 *Phys. Rev.* E **62** 6968
[160] Mishima O and Stanley H E 1998 *Nature* **392** 164
[161] Angell C A, Bressel R D, Hemmati M, Sare E J and Tucker J C 2000 *Phys. Chem. Chem. Phys.* **2** 1559
[162] Kanno H, Speedy R J and Angell C A 1975 *Science* **189** 880
[163] Mishima O 2000 *Phys. Rev. Lett.* **85** 334
[164] Debenedetti P G 1998 *Nature* **392** 127
[165] Johari G P, Hallbrucker A and Mayer E 1987 *Nature* **330** 552
[166] Hallbrucker A, Mayer E and Johari G P 1989 *Phil. Mag.* B **60** 179
[167] Kohl I, Bachmann L, Hallbrucker A, Mayer E and Loerting T 2005 *Phys. Chem. Chem. Phys.* **7** 3210
[168] Kohl I, Bachmann L, Mayer E, Hallbrucker A and Loerting T 2005 *Nature* **435** E1
[169] Salzmann C G, Kohl I, Loerting T, Mayer E and Hallbrucker A 2003 *Phys. Chem. Chem. Phys.* **5** 3507
[170] Handa Y P and Klug D D 1988 *J. Phys. Chem.* **92** 3323
[171] Smith R S and Kay B D 1999 *Nature* **398** 788
[172] Yue Y and Angell C A 2004 *Nature* **427** 717
[173] Angell C A *Science* at press
[174] Mishima O 2004 *J. Chem. Phys.* **121** 3161
[175] Andersson O 2005 *Phys. Rev. Lett.* **95** 205503
[176] Faraone A, Liu L, Mou C-Y, Yen C-W and Chen S-H 2004 *J. Chem. Phys.* **121** 10843
[177] Liu L, Chen S H, Faraone A, Yen C-W and Mou C-Y 2005 *Phys. Rev. Lett.* **95** 117802
[178] Zanotti J M, Bellissent-Funel M C and Chen S H 2005 *Europhys. Lett.* **71** 91
[179] Lyapin A G, Stal'gorova O V, Gromnitskaya E L and Brazhkin V V 2002 *J. Exp. Theor. Phys.* **94** 283
[180] Martonak R, Donadio D and Parrinello M 2005 *J. Chem. Phys.* **122** 134501
[181] Salzmann C G, Loerting T, Klotz S, Mirwald P W, Hallbrucker A and Mayer E 2006 *Phys. Chem. Chem. Phys.* **8** 386
[182] Klug D D, Mishima O and Whalley E 1987 *J. Chem. Phys.* **86** 5323
[183] Salzmann C G, Loerting T, Kohl I, Mayer E and Hallbrucker A 2002 *J. Phys. Chem.* B **106** 5587
[184] Salzmann C G, Kohl I, Loerting T, Mayer E and Hallbrucker A 2003 *Can. J. Phys.* **81** 25
[185] Nelmes R J, Loveday J S, Straessle T, Bull C L, Guthrie M, Hamel G and Klotz S 2006 *Nat. Phys.* **2** 414
[186] Salzmann C G, Mayer E and Hallbrucker A 2004 *Phys. Chem. Chem. Phys.* **6** 5156
[187] Giovambattista N, Stanley H E and Sciortino F 2005 *Phys. Rev. Lett.* **94** 107803
[188] Stanley H E 1971 *Introduction to Phase Transitions and Critical Phenomena* (New York: Oxford University Press)
[189] Moynihan C T, Macedo P B, Montrose C J, Gupta P K, DeBolt M A, Dill F J, Dom B E, Drake P W, Easteal A J, Elterman P B, Moeller R P, Sasabe H and Wilder J A 1976 *Ann. New York Acad. Sci.* **279** 15
[190] Giovambattista N, Angell C A, Sciortino F and Stanley H E 2005 *Phys. Rev.* E **72** 011203
[191] Mishima O and Suzuki Y 2002 *Nature* **419** 599
[192] Brovchenko I, Geiger A and Oleinikova A 2003 *J. Chem. Phys.* **118** 9473
[193] Brovchenko I, Geiger A and Oleinikova A 2005 *J. Chem. Phys.* **123** 044515
[194] Jedlovszky P and Vallauri R 2005 *J. Chem. Phys.* **122** 081101
[195] Buldyrev S V and Stanley H E 2003 *Physica* A **330** 124
[196] Allen M P and Tildesley D J 2004 *Computer Simulations of Liquids* (New York: Oxford University Press)

[197] Panagiotopoulos A Z 1987 *Mol. Phys.* **62** 701
[198] Hansen J-P and Verlet L 1969 *Phys. Rev.* **184** 151
[199] Corti D S and Debenedetti P G 1994 *Chem. Eng. Sci.* **49** 2712
[200] Finney J L, Bowron D T, Soper A K, Loerting T, Mayer E and Hallbrucker A 2002 *Phys. Rev. Lett.* **89** 205503
[201] Klotz S, Straessle T, Saitta A M, Rousse G, Hamel G, Nelmes R J, Loveday J S and Guthrie M 2005 *J. Phys.: Condens. Matter* **17** S967
[202] Klotz S, Straessle T, Nelmes R J, Loveday J S, Hamel G, Rousse G, Canny B, Chervin J C and Saitta A M 2005 *Phys. Rev. Lett.* **94** 025506
[203] Klotz S, Hamel G, Loveday J S, Nelmes R J, Guthrie M and Soper A K 2002 *Phys. Rev. Lett.* **89** 285502
[204] Hemley R J, Chen L C and Mao H K 1989 *Nature* **338** 638
[205] Yoshimura Y, Mao H-k and Hemley R J 2006 *Chem. Phys. Lett.* **420** 503
[206] Yoshimura Y, Stewart S T, Somayazulu M, Mao H-k and Hemley R J 2006 *J. Chem. Phys.* **124** 024502
[207] Finney J L, Hallbrucker A, Kohl I, Soper A K and Bowron D T 2002 *Phys. Rev. Lett.* **88** 225503
[208] Guthrie M, Tulk C A, Benmore C J and Klug D D 2004 *Chem. Phys. Lett.* **397** 335
[209] Bellissent-Funel M C, Bosio L, Hallbrucker A, Mayer E and Sridi-Dorbez R 1992 *J. Chem. Phys.* **97** 1282
[210] Bizid A, Bosio L, Defrain A and Oumezzine M 1987 *J. Chem. Phys.* **87** 2225
[211] Bellissent-Funel M-C, Teixeira J and Bosio L 1987 *J. Chem. Phys.* **87** 2231
[212] Kuhs W F, Finney J L, Vettier C and Bliss D V 1984 *J. Chem. Phys.* **81** 3612
[213] Klotz S, Hamel G, Loveday J S, Nelmes R J and Guthrie M 2003 *Z. Kristallogr.* **218** 117
[214] Soper A K and Ricci M A 2000 *Phys. Rev. Lett.* **84** 2881
[215] Pusztai L 2000 *Phys. Rev.* B **61** 28
[216] Saitta A M, Strässle T, Rousse G, Hamel G, Klotz S, Nelmes R J and Loveday J S 2004 *J. Chem. Phys.* **121** 8430
[217] Guillot B and Guissani Y 2001 *J. Chem. Phys.* **114** 6720
[218] Giovambattista N, Debenedetti P G, Sciortino F and Stanley H E 2005 *Phys. Rev.* E **71** 061505
[219] Errington J R and Debenedetti P G 2001 *Nature* **409** 318
[220] Waller R 1964 *Essays of Natural Experiments* (New York: Johnson Reprint)
[221] Loerting *et al* 2006 *Phys. Chem. Chem. Phys.* **8** 2810
[222] Harrington S *et al* 1997 *J. Chem. Phys.* **107** 7443